Ph.D. Dissertation

Vehicle Ride and Handling Control Using Active Hydraulically Interconnected Suspension

University of Technology Sydney

Electrical, Mechanical and Mechatronics School

Center for Green Energy and Vehicle Innovations

Anton Tkachev	Prof. Nong Zhang	A.Prof Steven Su
PhD Candidate	Principle Supervisor	Co-Supervisor

5 March 2018

Certification of Original Authorship

I certify that the work in this thesis has not previously been submitted for a degree nor has it been submitted as part of requirements for a degree except as fully acknowledged within the text. I also certify that the thesis has been written by me. Any help that I have received in my research work and the preparation of the thesis itself has been acknowledged. In addition, I certify that all information sources and literature used are indicated in the thesis.

Signature of Student: Production Note: Signature removed prior to publication.

Date: 5 March 2018

Acknowledgements

I would like to acknowledge my principle supervisor Prof. Nong Zhang for giving me such an excellent opportunity to work on this project and to learn. I am thankful to Prof. Zhang for his guidance and practical advice. I would like to thank Prof. Zhang for his friendly and fatherly attitude which he usually has towards his students. I want to thank my co-supervisor A.Prof. Steven Su for spending a lot of time with me in the office and the lab educating me on the control theory topics and guiding me in my work from the control point of view. I acknowledge Dr Steven Su for his excellent teaching skill and high professional competence that were of great help to me. I acknowledge the Lab Engineer Christopher Chapman for his valuable pieces of advice given at the right time on many practical matters, for assessing my CAD drawings and helping me out in building the setup. Christopher Chapman is a good-natured person who is always willing to help and share his experience which he attained through decades of experimental work. I am thankful to him for being ready to discuss any question and helping me in taking critical decisions in my project. Also, I would like to note that his lab is kept in perfect order and tidiness at all times making work there a pleasure. I am very thankful to Laurence Stonard and Siegfried Holler from UTS Workshop who were friendly, helpful and highly professional in making custom parts and assemblies. I should say here that Laurence Stonard was always open for discussions too and gave me some useful pieces of advice regarding the designs and the hardware. I would like to thank Siegfried Holler for making all custom parts and assemblies and addressing the needs of the project promptly and professionally. It was a pleasure to work with Siegfried Holler and Laurence Stonard. I would like to thank Paul Walker for his

support and Paul's capstone student Sung Wook Suh who helped me a lot in the lab. Sung Wook was doing his capstone project on the half-car testing rig under Paul's supervision, and we all collaborated productively. Sung Wook was always coming to the lab when I needed help, and together with him, we have done most of the commissioning and experimental work.

Dedication

I dedicate this thesis to all my dearest family: my darling wife Anastasia who loves me and tirelessly takes care of me all the time and who came to Australia with me, my parents Anatoly and Tatyana who brought me up in a difficult time and also love me so much and always support me in any situation, my younger sister Elena who is my best friend forever and who knows me like herself! I would like to specially mention here my dear grandmother Valentina who passed away in the year 2016. She worked as a teacher of English at a school for 40 years and she taught me not only English but so many other good things that I feel very grateful for. And, of course, I want to say thanks to all my good friends who share their love and support and always make me laugh and always make me happy!

If you are reading and recognising yourself in these lines then, Hi there! :)

Contents

List of Figures

List of Tables

Abstract

In this thesis, is proposed a different actuator layout for active anti-roll hydraulically interconnected vehicle suspension. Unlike other designs, the layout suggested, is a closed circuit which is powered by a hydro-mechanical actuator and neither needs a storage tank for the fluid, nor it needs a pump for charging the storage tank. The project includes four main components: modelling, simulations, the practical part and the experimental part. In the modelling part, the author derived an augmented half-car model which additionally takes lateral acceleration as a disturbance. The model of active hydraulically interconnected suspension system was also obtained. The practical component of the author's work focuses on the upgrade of the existing half-car testing rig the Dynamics Laboratory at UTS. A precise CAD modelling of the half-car testing rig was done. Then, were proposed the upgrades. The setup was upgraded in compliance with the models designed. After the upgrades, followed the experimental part. The experiments were conducted in three stages: the identification experiments, the implementation of a real LQG compensator and the validation experiments. The author adopted a methodology known as a classical approach in control theory in which the models of a physical system are identified in the frequency domain prior to the design of a control system. In the thesis, it is discussed in detail how the experiments were conducted and the data analysed. All theoretical derivations, mechanical drawings, and codes are thoroughly explained. The experimental results indicate two significant outcomes: the identified models demonstrate high prediction power, the LQG compensator improves frequency response characteristics of the system and achieves significant roll angle reduction across the range

of frequencies of the interest including the resonance. Overall, the results obtained experimentally come in excellent agreement with the simulations which confirms the integrity of current research.

Chapter 1

Introduction

1.1 Historical Reference

The history of hydraulic suspensions begins from the mid-20th century. In this section, we briefly review some historical facts significant to the development of kinetic suspension systems. In 1955 Citroen DS introduced the first four-wheel hydropneumatic (nitrogen-over-oil) suspension system. In 1962 The Morris 1100's Hydrolastic suspension used rubber springs and water-based fluid. In 1963 The Mercedes-Benz 600 employed rubber air springs with hydraulically adjusted two-position dampers. In 1965 Rolls-Royce licensed Citroen technology for its Silver Shadow. In 1970 Citroen GS offered a hydro-pneumatic system on a small, affordable sedan. In 1989 Chris Heyring of Dunsborough, Western Australia founded Kinetic Suspension Technology. In 1999 Tenneco purchased Kinetic for $52 million. In 2002 the Audi RS6 used a cross-linked suspension with extra damper pressure supplied on demand to manage pitch and roll. In 2004 Lexus introduced a Kinetic dynamic suspension on the GX470. In 2006 Kinetic suspension systems were banned from use in World Rally Championship and Dakar Rally competition. In 2011 the Infiniti QX56 offered hydraulic body motion control.

1.2 Hydraulically Interconnected Suspension

Rollover prevention is commonly considered to be one of the prominent priorities in vehicle safety and handling control. A promising alternative to anti-roll bars is the hydraulically interconnected suspension. Historically, passive hydraulically interconnected suspensions have been widely discussed and studied up until the present, whereas a study of the active systems has been done partially and yet has some topics to cover. Current research work focuses explicitly on active hydraulically interconnected suspension systems (active HIS). Although, active HIS systems were studied in [1], [2] and [3], in this thesis, we propose a new concept of a closed hydraulic circuit as opposed to open circuits presented in the papers above.

The system involved consists of two separate subsystems that can be modelled independently and then combined in a robust model. One of the subsystems describes a 4 degrees of freedom half-car model which, besides other things, is responsible for lateral vehicle dynamics. The other subsystem is active hydraulically interconnected suspension which is responsible for the active reduction of the roll angle. The subsystems are coupled via the hydraulics-to-mechanical boundary condition.

To understand the action of active HIS, consider the dynamics of a vehicle undergoing a turning maneuver which is shown in figure 1.1. As seen in the figure, the vehicle body inclines under the action of a lateral force which results from lateral dynamics of the vehicle. In a non-inertial reference frame associated with the vehicle's centre of gravity, the centrifugal force is exerted on vehicle body causing it to lean in the roll plane.

1.3 Active HIS System

To begin, we need first to address passive HIS which was modelled and thoroughly studied in [4], [5] and [6] by Nong Zhang, Wade A. Smith et. al. Their studies proved HIS systems to have a promising potential for the improvement of driving safety and rollover prevention. Figure 1.2 can illustrate the general idea of passive HIS system. In the figure, it is seen that when the vehicle body inclines due to a turning maneuver,

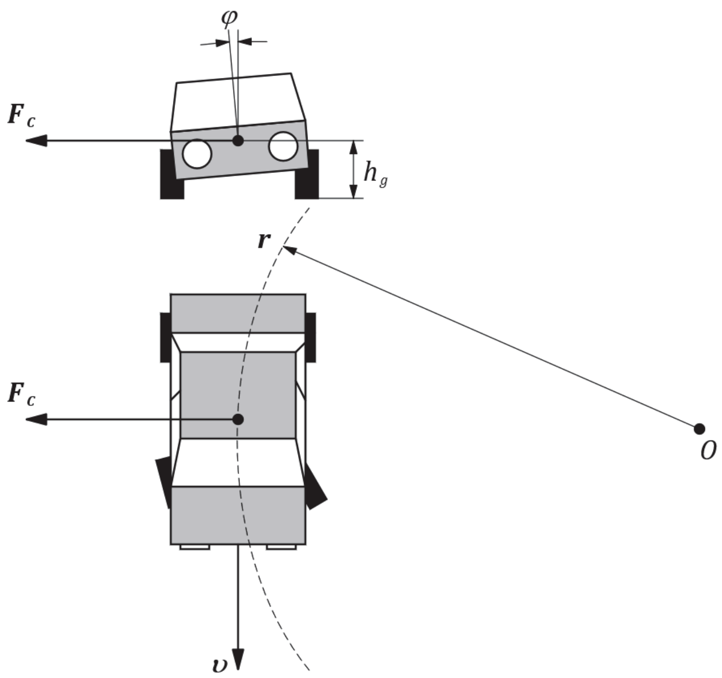

Figure 1.1: The dynamics of a vehicle performing a turning manoeuvre. The projections shown are: the front veiw and the top view.

the differential pressure is built up in the HIS system creating a counter roll moment to oppose that of the centrifugal force.

Although the original passive system is already more efficient than an anti-roll bar, it opens an opportunity for further improvement by making the system active. To upgrade HIS system, initially passive, one can enhance its performance with an actuator augmented to the original passive HIS. As mentioned above, the model derived in this thesis implements a conceptually new closed hydraulic circuit which

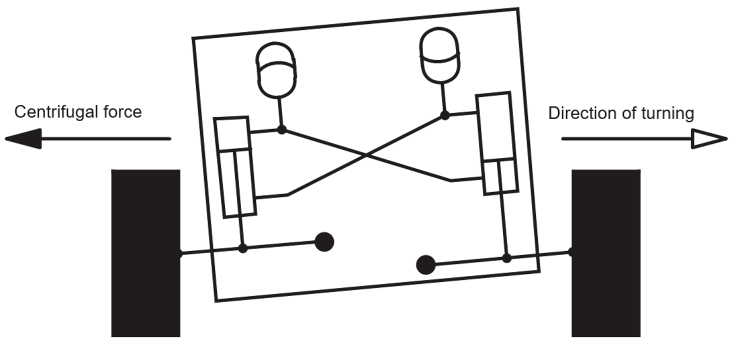

Figure 1.2: The general idea of the hydraulically interconnected suspension

does not require an additional storage tank for the hydraulic fluid, unlike other studies on active HIS system, e.g., [1]. Neither this system needs a pre-charged accumulator as a source of energy and a pump for pre-charging. The concept of the system studied in this thesis is shown in 1.3. It can be seen that there is an additional hydraulic actuator introduced into the hydraulic circuit. One can see that the hydraulic circuit is closed and has neither the storage tank nor the charging pump unit.

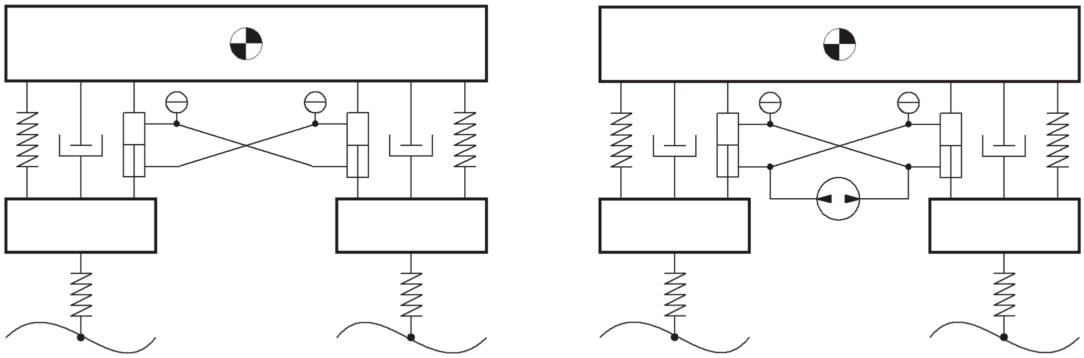

(a) Passive HIS (b) Active HIS

Figure 1.3: The concept of passive and active hydraulically interconnected suspension

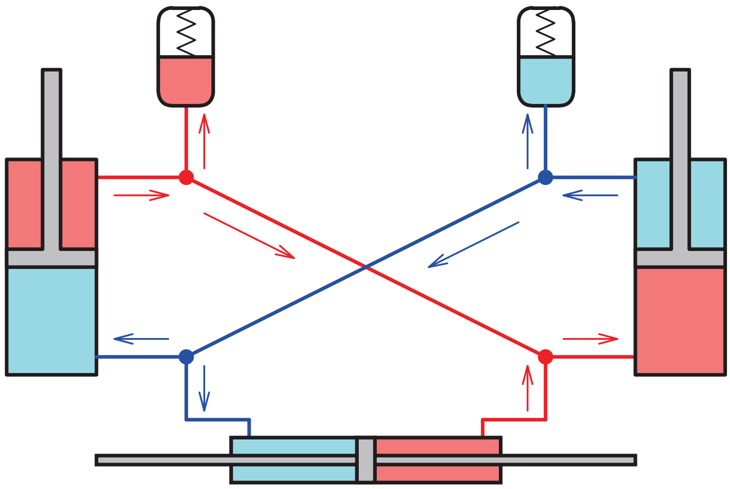

Figure 1.4: Active hydraulically interconnected suspension schematic diagram

1.4 Literature Review

It is important to mention that present work is mainly based on the fundamentals of Mechanical Engineering, although it relies on many adjacent engineering fields too, e.g., Hydraulics, Control Theory, Linear Dynamics, and so forth. An intensive study of hydraulic interconnected suspensions had been conducted by the group of Prof. Nong Zhang at UTS during recent ten years. In this section, we review main publications related to the subject of current research: Hydraulically Interconnected Suspensions, produced by Prof. Zhang's group and other authors. In this Literature review, we first enumerate the publications in a timely manner for the reader to get familiar with the background of current research topic. Then, we discuss the research gaps and a the weaknesses of these publications which is followed by a summary of all preceding research.

1.4.1 Timeline of Preceding Research

As mentioned above, first implementations of interconnected suspension took place in the early 2000's. Since then, the research on this topic has advanced dramatically. The following list of publications represents an overview of ideas and also reflects the advancement of the research through time beginning from the year 2005 and ending at present.

First attempts of experimental studies of hydraulically interconnected suspensions were taken by the authors of [7] and [8]. In paper [7] the authors used hydraulically interconnected suspension designed in Tenneco Automotive and equipped two Honda CRV sport utility vehicles with it. They subjected the vehicles to extreme maneuvers such as fishhook to examine the lateral behaviour of the vehicles. The key parameters including the roll angle, vehicle speed, steering angle and the lateral acceleration were monitored. In their experiments, the authors found a significant improvement of the roll-over stability of the vehicles. For instance, one of the vehicles was able to increase its NHTSA fishhook speed from 43 mph to 60 mph without ever yielding a two-wheel-lift condition.

Although the paper presents an experimental study, it does not talk about the designs of hydraulically interconnected suspensions. The parameters of the hydraulically interconnected suspension system are missing as well as the properties of the vehicles. However, it is out of the question that the authors conducted thorough simulations before actually building the suspensions, which is presented in the next paper.

Paper [8] presents the computational approach to studying hydraulically interconnected suspensions. A vehicle is accurately modelled with a software named ADAMS. A simulation of vehicle lateral dynamic responses is performed under NHTSA standard tests. The simulations demonstrate the benefits of hydraulically interconnected suspension developed by Tenneco Automotive. ADAMS software allows one to precisely simulate almost any mechanical system, however, the system under consideration can be also analysed analytically which may provide additional understanding of the designs.

In [9], two distinct principles of hydro-pneumatic suspension struts are discussed. The two alternatives are either hydraulic or pneumatic interconnections between the struts in wheel suspensions. The method employs a compact strut layout that integrates a gas chamber and damping valves into a unit and gives considerably more advantage by reducing the operating pressure significantly. A cross-connection between the hydro-pneumatic struts can efficiently suppress the roll plane degree of freedom of a vehicle. In the paper, have been studied static and dynamic heave and roll properties of cross-connected hydraulic suspension. Such benefits as enhancing the roll stability and at the same time keeping smooth heave experience have been discovered. Hydraulically and pneumatically interconnected strut configurations were analysed for heavy vehicles. Fluid compressibility was accounted for. The feedback effect related to hydraulic interconnections was found to be significant. Roll stiffness and damping characteristics were compared among various configurations of hydraulic interconnections including the direct connection, cross connection and no connection. The effects of such connections are discussed in the article and figures presented.

It has been found that the cross-connection provides a noticeable roll stiffness improvement enhancing anti-roll stability of a vehicle. The authors conclude the most important benefit of the interconnected suspension is the flexibility of tuning the suspension parameters.

This paper is the only one to compare the performance between a hydraulic and pneumatic interconnected suspension. Although the authors found both alternatives, hydraulic and pneumatic, to enhance roll stiffness of the vehicle, we can conclude that their preference is given to a hydraulic suspension as the one capable of handling heavy loads sacrificing the advantage of faster action speed which can be achieved with pneumatics.

Paper [10] studies the dynamic response of a model having uncertainties of parameters. In this study is used the half-car model which is subjected to a random road excitation input. Such key parameters as the mass of the vehicle body, moment of inertia of the vehicle, masses of the front and rear wheels, damping coefficients and spring stiffness of front and rear suspensions, distances of the front and rear suspension locations to the centre of gravity, and the stiffness of front and rear tires are assumed to have random uncertainty. The roughness of the road is modelled with a Gaussian random process with pure exponential power spectral density. Monte-Carlo simulation is used to obtain the mean and the variance of vehicle's natural frequencies as well as the mean square of the vehicle's response. The influence of the uncertainties of vehicle parameters is then discussed in the paper and concluded to affect vehicle performance although within appropriate tolerance frames.

This paper attempts to assess the variance of vehicle responses under the condition of the uncertainty of its parameters. Theoretical foundations are given and Monte-Carlo simulations performed. The methodology presented is important due to the necessity to validate real models' robustness over a range of possible parameter deviations.

An alternative approach to finding the vehicle vibration model parameters is proposed in [11]. The natural frequencies, damping ratios and the mode shapes of the half-car with general hydraulically interconnected suspension system are obtained in this paper. The proposed dynamic model of the system consists of a sprung mass, unsprung masses, and the hydraulically interconnected suspension connected to the wheel struts. The model is formalised in state-space representation. The state variable describes lumped masses motions in the model that are also coupled to the hydraulically interconnected suspension fluid circuit. The transient dynamics of the model is studied in numerical simulations. In particular, free vibration responses are obtained under specific initial conditions of the road input disturbances. The results are compared with those obtained via the simulations of the transfer function model. The advantages and disadvantages of state-space model as compared with the transfer function model are then discussed. The authors conclude state-space representation to be more practical for use. However, transfer function representation preserves the physical meaning of the variables, unlike the state-space which may often lead to the loss of decent physical meaning of the state variable.

In the paper, matrix equations of motion of a vehicle equipped with hydraulically interconnected suspension were obtained. Free vibration responses were simulated. Strangely, the authors arrived at a complex value of the state variable, which might be incorrect. However, the paper demonstrated an alternative approach to the analysis of hydraulically interconnected suspension which is based on analytical derivation of the equations of motion. The advantage of this method is the possibility of compute free vibration modes and relatively easily find the damping ratio and the natural frequency.

In thesis [12] is examined the dynamics of hydraulically interconnected suspension which belongs to a particular class of vehicle anti-roll suspension systems. The author of thesis claims this type of suspension to break the compromise between ride and handling performance of a vehicle. As of 2005 hydraulically interconnected suspensions had not been studied in the academic literature much. The author of the thesis [12] believes that the involved class of suspensions features unique capabilities among all other known passive suspensions. Specifically, unlike other passive suspension systems, such as, for example, anti-roll bar, in a hydraulically interconnected suspension system the stiffness and damping exposed depend on the excitation mode: either bounce or articulation. The modelling approach adopted in this thesis is multidisciplinary. It involves the theory of mechanical vibrations as well as the linear fluid dynamics theory. This thesis illustrates the basic principles and demonstrates the application of the methodology based on a simple half-car model. The half-car is modelled as a lumped mass multi-body system, and the hydraulic circuit is also assumed to have some distributed parameters. Fluid circuit components are modelled individually using the impedance method. The resulting system model forms a set of linear frequency-dependent state-space equations that govern the dynamics of the half-car coupled with a hydraulically interconnected suspension. The equations were studied in different ways including free vibration analysis, ride comfort assessment and multi-objective optimisation. The author of thesis identified some of the critical elements influencing the performance of hydraulically interconnected suspension and also studied how sensitive the model is towards the change of parameters identified. The author validates his findings in two ways. First one is the simulation of an identical half-car model with an alternative non-linear fluid model. The second way of validation is experimental tests on the half-car testing rig which was purposely built for the project. The author of thesis obtained experimental results in both free and forced tests. The author concluded the results obtained to agree with the simulated linear model at a satisfactory level of endorsement. The author claims his methodology to be practical for modelling vehicles equipped with hydraulically interconnected suspensions primarily in the frequency domain. The author concludes that his findings demonstrate hydraulically interconnected suspensions to provide a somewhat better compromise between vehicle ride and handling performance. Finally, the author advises further investigation into the topic primarily involving modelling of a full-scale vehicle.

In paper [13] is proposed a novel layout for so-called demand dependent active suspension which focuses mainly on vehicle roll-over control. The authors claim that as of the year 2009 using active suspensions for vehicle roll-over control had not been widely studied although active suspensions were used for the improvement of vehicle ride and handling. The authors proposed an active suspension design comprised of four hydraulic actuators that are interconnected hydraulically to actively compensate for the vehicle's roll motion by supplying restoring roll moment at the suspension struts. The authors conclude active suspension to outperform passive or semi-active one regarding ride and handling improvement. The authors then validated their theoretical findings experimentally on a real vehicle fitted with demand dependent active suspension. The experimental results obtained in this paper confirm the effectiveness of demand dependent active suspension for roll-over control.

The paper explains in every detail how an experimental stand for the testing full vehicle equipped with hydraulically interconnected suspension was created. Along with the stand was designed and created a hydraulically interconnected suspension with switching configuration. The authors subjected the vehicle to a random road roughness input for two different configurations of hydraulic connections. However, the paper can be rather considered as a report on building the experimental setup than making a significant research contribution. Nevertheless, the paper shares the valuable experience of design and construction of the experimental stand.

A novel approach to frequency domain analysis of a vehicle equipped with a general hydraulically interconnected suspension system is proposed by authors of [4]. The authors believe hydraulically interconnected suspension to attribute the unique ability compared with other passive systems to provide mode-dependent stiffness and damping characteristics. The methodology proposed is demonstrated on a basic lumped-mass four degree of freedom mechanical half-car model. The hydraulically interconnected suspension force is modelled with the mechanical-to-fluid boundary condition regarding the hydraulic suspension cylinder. The hydraulically interconnected suspension force is then accounted for as external in the mechanical model. The fluid system is modelled with hydraulic impedance method which defines, generally, differential relationships between the hydraulic flow and the pressure drop across the hydraulic lumped elements. Thus, the authors obtain a set of frequency dependent differential equations that are further subject to free and forced vibration analysis. In their studies, the authors considered two types of wheel-pair interconnections that are the anti-synchronous and anti-oppositional. The paper then gives an example of using anti-roll hydraulically interconnected suspension system. A detailed discussion of free vibration solutions and frequency responses of the transfer functions obtained is presented. The authors conclude that the approach proposed provides a fundamental basis for further research on the dynamic properties of vehicles equipped with hydraulically interconnected suspension. The results obtained confirm hydraulically interconnected suspension to be able to provide different mode-selective stiffness and damping characteristics of the vehicle suspension.

This paper represents a thorough fulfilment of the analytical approach to the analysis of passive hydraulically interconnected suspension system. The authors derive the equations of motion for the half-car model as well as the hydraulic circuit equations. The paper is the first one to reproduce the processes in such a complicated system thoroughly. However, the model neglects viscous fluid damping as well as fluid inertia. Another simplification is using a linear model for hydraulic accumulators. The pole-zero map representation is unconventionally chosen to be a 3D surface. Only zeros are shown in the figure, and strangely no poles. In their next paper the authors use the model obtained to perform simulations and use them for the design of the experimental setup.

In paper [5] the authors start their research based on the previously derived model of a vehicle equipped with the hydraulically interconnected suspension system which was used for frequency domain analysis. In this paper, the authors subjected the four degrees of freedom half-car model to the ride analysis under a rough road input. The road roughness was modelled with a two-dimensional Gaussian random process. Its power spectral density function represented the road input profile and the frequency responses of the half-car model were obtained for such variables as bounce, roll angle, roll acceleration, suspension deflection and dynamic tyre loads. The simulation results were compared in detail between a half-car fitted with hydraulically interconnected suspension system and the conventional half-car model. The sensitivity of the model to uncertainties of its parameters was also studied through simulations. The validation of simulation results was conducted by the authors experimentally in both free and forced vibrations tests in the half-car roll plane. The paper describes the experimental setup in detail including mechanical and hydraulic layouts, data acquisition system and the external force actuation mechanism. The authors discussed the methodology of free and forced vibration tests regarding the validation of simulations results. The tests were conducted at different hydraulic pressure settings across the reasonable range of pressures. It is also discussed how the effective damper valve pressure drop is accounted for in the mathematical models and observed experimentally. The authors examined the deficiencies, and practical implications of the model proposed and gave suggestions for future research. The authors conclude about the performance of the roll-plane hydraulically interconnected suspension as a promising method of enhancing vehicle roll stability and safety.

The authors of [5] report the design and construction of the half-car testing rig. Extensive simulations performed and the outcomes used in designs of the new half-car testing rig. The authors state that the new half-car testing rig can repeat the behaviour of a real vehicle in bounce and roll modes. The testing rig parameters are characterised and provided. Experimental results show good agreement between the simulated and measured experimental response data.

The authors of paper [14] derived four degrees of freedom half-car model for studying vehicles equipped with anti-roll systems. Several systems as such were involved in this paper: the anti-roll bar, the roll plane hydraulically interconnected suspensions as well as active suspensions. The authors first obtain a model of a vehicle followed by parameters estimation and experimental tests conducted to compare between two passive anti-roll systems. For purposes of modelling a torsional spring model was adopted to represent the equivalent roll stiffness of an anti-roll bar. The authors conclude that the advantage of such a model is that the vehicle model and the anti-roll system model can be analysed separately. The vehicle parameters and the anti-roll system parameters can be estimated independently as well. Moreover, the authors claim that different anti-roll systems of the kind can be compared by merely varying the roll stiffness of the vehicle model. The authors propose an approach to vehicle parameters identification via free vibration tests and thus derive the transition matrix by utilising the state variable method. The authors then solve the eigenvalue problem to obtain system modes parameters such as the natural frequencies and the decay constants, i.e. the damping ratios. The authors reconstruct the system matrix by solving so-called inverse eigenvalue problem. Given the form of system transition equations, the inertia and stiffness parameters are estimated through solving the inverse eigenvalue problem numerically. Damping parameters were estimated separately under an assumption of no tire damping. The agreement of the simulated models with the experiments was confirmed by conducting vehicle roll and bounce experimental tests. In their experiments, the authors compared the anti-roll bar with the passive hydraulically interconnected suspension system. Both systems were consequently installed on the same vehicle and then tested. Both systems showed to enhance suspension roll stiffness. However, the anti-roll bar was also found to lock the so-called articulation mode which appears to be a disadvantage as opposed to the passive hydraulically interconnected suspension system.

In paper [14] the authors attempt to analyse free vibration responses of a half-car equipped with the hydraulically interconnected suspension to a step input in the frequency domain. However, after taking fast Fourier transform of time-domain signals one can see that it is extremely challenging to draw conclusions out of the frequency domain data. For this particular reason, any sensible interpretations of frequency domain data are missing. Nevertheless, this paper makes a step towards frequency analysis of dynamic models which is widely used in the current thesis in a more systematic manner.

The authors of [6] contributed to the research on hydraulically interconnected suspension systems. The authors report hydraulically interconnected suspension systems to be addressed more in the research community as of 2011 due to their unique ability to provide stiffness and damping depending on the mode of operation, i.e. bounce, roll, pitch or articulation. Unlike single wheel independent suspension stations, the hydraulically interconnected suspension allows more flexibility in tuning the suspension performance. The authors of the paper formalised a full-car nine degrees of freedom model and examined it under commonly used manoeuvres such as, for example, fishhook to assess vehicle's handling performance. The simulations were conducted for conventional suspension model and hydraulically interconnected suspension model to compare between the two. The fluid subsystem was modelled with the non-linear approach. The hydraulic and mechanical systems are coupled via a hydraulic-to-mechanical boundary condition forming a set of simultaneous differential equations that govern the dynamics of the entire system. The simulation results demonstrate hydraulically interconnected suspension to have handling ability superior to a conventional vehicle suspension as evidently follows from the measurements of roll angle, roll rate, roll acceleration, lateral acceleration and the vehicle's rollover critical factor. The effects of hydraulically interconnected suspension on ride performance were studied as well through the transient response simulations when one side of the vehicle traverses a half-sine bump. The authors discussed the results obtained and concluded the results to be consistent with the previous findings of other researchers. The authors claimed to have posted an alternative approach to studying the vehicles fitted with the hydraulically interconnected suspension which is especially suited to time-domain simulations.

In the paper, is derived a model of half-car fitted with hydraulically interconnected suspension. The equations of motion are then converted to a state-space. Vehicle roll-over stability is assessed with the quantity named Rollover Critical Factor under different excitation inputs including both steering input and road input. The authors report having used a non-linear model for hydraulic accumulators. The paper contains a thorough analysis of the results followed by a discussion of further work. As of the year 2011, the authors reported a significant computational cost of the models obtained. However, with modern computers, the computation can be done much faster.

The authors of [15] report the studies of hydraulically interconnected suspension to be motivated by attempts at creating a cost-effective vehicle anti-roll system more efficient than an anti-roll bar. The authors claim that hydraulically interconnected suspension has been proved both theoretically and practically to have its anti-roll ability superior to the anti-roll bars. And therefore hydraulically interconnected suspension attained commercial success in racing vehicles as well as luxury sports utility vehicles. The authors of [15] emphasise the importance of research on the vehicles equipped with the hydraulically interconnected suspension due to the complicated nature of vehicle as a mechanical system. As per [15], apart from anti-roll ability, ride comfort and lateral stability, other aspects of vehicle dynamics need to be studied. In the paper is presented an experimental investigation into the dynamics of a sports utility vehicle fitted with the hydraulically interconnected suspension system. The vehicle is studied under a severe steady steering manoeuvre. The same vehicle is used to independently test the performance of commonly used anti-roll bars for comparison under the same testing conditions. The authors discuss their ideas of how to optimise hydraulically interconnected suspension to enhance its performance when subjected to extreme manoeuvres like the one used in the experimental tests. The authors use real-time simulations to assist the experiments and provide a better picture of the hydraulic system response. It is concluded that both experimentally and theoretically hydraulically interconnected suspension performs better than an anti-roll bar.

The paper reports building hydraulically interconnected suspension for a real vehicle. The authors also conduct field tests and share the experience. Although the paper contains both the modelling part and the experimental part, the link between the two is somewhat missing. However the experience and experimental results contribute to the research.

In [16] is proposed a novel hydraulically interconnected suspension system which allows for a compromise between the pitch and bounce modes of the vehicle. The impedance matrix of the hydraulic subsystem is derived using the transfer function method. The hydraulic sub-model is then coupled with the mechanical system, and the multi-body dynamic equations are obtained. The identification is made through eigenvalue iterations performed for a frequency dependent characteristic equation of the system which is derived from numerical optimisation. The authors compare free vibration analysis between a three-axle truck having conventional suspension and that fitted with the hydraulically interconnected suspension system. The results obtained demonstrate that anti-oppositional hydraulically interconnected suspension system can significantly reduce pitch motion of the vehicle as well as maintain ride comfort simultaneously. For the suspension involved, the pitch stiffness increases while the bounce mode properties become softer. The peak values of body bounce and wheel hop reduce drastically. The damping ratio of the vehicle body bounce is also enhanced providing passengers with better ride comfort.

The authors of [17] proposed a new implementation of the hydraulically interconnected suspension system for pitch and bounce mode resistance control when it is installed on heavy three-axle trucks. A lumped mass model of a half-truck was formalised using free body diagram method. The forces generated by the fluid system are incorporated into the mechanical model and accounted for as external to the mechanical system. The fluid impedance matrix of the hydraulic subsystem is obtained through the transfer matrix method. The hydraulic subsystem consists of the pipes, damper valves, accumulators and tee-junctions. The boundary condition and the transfer matrix method is used to find quantitative relationships between the mechanical and the fluid sub-models. The conventional truck model is compared with the truck model incorporating hydraulically interconnected suspension via modal simulations and analysis. The comparison is made for free vibration responses, the eigenvalues, the isolation vibration capacity and the forced vibrations. The power spectrum densities are measured. The authors of the paper conclude that the results obtained show the effectiveness of hydraulically interconnected suspension in reducing pitch mode oscillations and at the same time maintaining the ride comfort. The pitch stiffness is reported to have increased while the bounce stiffness was slightly softened. The peak responses of wheel hop and body bounce are said to have reduced noticeably. The vibrations damping parameters increased.

Papers [16] and [17] are the first ones to model hydraulically interconnected suspension on a multi-axle truck vehicle. The modelling equations are worked out cleanly and represent a very complicated system. Strangely, the pole-zero map is uncommonly presented as a 3D figure having only the zeros and no poles. As reported by the authors, the state variable contains complex values, which is unlikely to be correct according to theory. However, the modelling part provides valuable information regarding the three-axle vehicle fitted with hydraulically interconnected suspension. The Bode diagrams are obtained, analysed and interpreted. The conclusion drawn is that the hydraulically interconnected suspension system effectively suppresses road roughness in all the modes of a multi-axle truck vehicle. Low frequency modes are also noticeably attenuated.

In paper [18] modelling and parameters estimation for a novel low-cost active hydraulically interconnected suspension was performed. The findings were also confirmed experimentally. An estimated state-space model of the combined mechanical system and hydraulic system was derived from designing and testing an H-infinity controller for active vehicle body roll reduction. The controller was verified numerically. The authors of the paper propose a safety-oriented low-cost active hydraulically interconnected suspension in an attempt make active suspensions more affordable. Unlike other active suspensions with four individual actuators located at each wheel, the active hydraulically interconnected suspension is controlled by a single hydraulic pressure valve only, which makes it much more competitive regarding cost-effectiveness than many other active suspension systems. The authors designed and assembled a pressure control unit as the critical part of the hydraulic system which connects to the existing passive hydraulic components such as hydraulic pipes and hydraulic cylinders. The authors discuss the appropriate choice of the pressure controller parameters as these are of critical importance for the design of the model-based optimal controller. The authors advise that the pressure controller needs to be simple enough for effective control strategy implementation and the enhancement of system's dynamic characteristics. The authors adopted an empirical approach to the controller design using the estimated models obtained previously. A Bode diagram of the real and the estimated numerical models are used as a benchmark.

Paper [18] is the first to talk about active hydraulically interconnected suspension. The paper reports building an active pressure control unit embedded into the hydraulic circuit of a vehicle. Secondly, it is worth mentioning that the authors attempted to perform real system identification using frequency analysis same as we did in current theses. The authors managed to obtain experimental Bode plot, although with a limited frequency range. The underlying model was also obtained. The methodology of forced vibration experiment and some data interpretation was introduced in this paper for the first time.

The authors of [19] present a detailed experimental investigation into the quantitative comparison of a roll-plane hydraulically interconnected suspension and an anti-roll bar. Particularly the study focuses on the so-called articulation excitation mode. The authors emphasise on the point that anti-roll bars usually are part of conventional vehicle suspension systems that are widely used in road vehicles to enhance the roll-stiffness, handling performance and safety of a vehicle in a rapid turning manoeuvre. However, as opposed to hydraulically interconnected suspensions anti-roll bars have a disadvantage of imposing undesired constraints on vertical wheel travel when driving on an uneven surface which also affects wheel-ground holding ability specifically in the articulation mode. Roll-plane hydraulically interconnected suspensions can potentially replace anti-roll bars as an alternative that allows more flexibility in changing roll damping and roll stiffness without affecting the articulation mode. In this paper, the authors share their findings on the experimental analysis of the roll-plane hydraulically interconnected suspension system in comparison with anti-roll bars. The tests were conducted on a sports utility vehicle equipped with an anti-roll bar and then fitted with a hydraulically interconnected suspension system. The articulation mode excitation tests were prioritised. The authors claim their experimental results to demonstrate that an anti-roll bar has negative effect on the articulation mode flexibility whereas the roll-plane hydraulically interconnected suspension enhances roll stiffness and vehicle roll-over safety in general without affecting the articulation mode.

In this paper are compared to the two alternative solutions for roll angle reduction. Namely the anti-roll bar and the hydraulically interconnected suspension. It is common knowledge that along with positive effect on roll motion anti-roll bar interlocks the articulation wheel mode which is considered a disadvantage. The authors of the paper conduct an experimental investigation into the articulation performance of two concurrent systems and report the results. Although the experimental results are provided, any theoretical background is missing. However, the empirical study is profound and thorough.

Another study of the novel cost-effective active hydraulically interconnected suspension is done in paper [1]. The authors chose H-infinity control strategy for active vehicle roll motion control. The experimental test was conducted on a sports utility vehicle equipped with an active hydraulically interconnected suspension system. Estimation of model parameters was done from the experimental data, and the results were used in H-infinity controller design. The active suspension model was formalised and combined with a half-car model via mechanical-to-hydraulic boundary conditions. The authors also discussed the choice of appropriate weighing function for H-infinity controller design. The experimental tests were conducted on a four-post testing rig where a real vehicle equipped with active hydraulically interconnected suspension was subjected to various road excitation patterns: such as single wheel bump, articulation bump and other. The results obtained demonstrated significant roll angle reduction delivered by the H-infinity controller. The experimental test proved H-infinity to be an effective control strategy for active vehicle roll angle control.

In paper [1] the authors derive, implement and test an H-infinity controller on the testing setup comprised by a full-car fitted with hydraulically interconnected suspension. This paper is the first attempt, although challenging, to apply advanced control to the system under consideration. However, the controller design is based on an assumed theoretical model, not the measured experimental one. The authors rely on the robustness of the chosen control method and try to tune their analytical equations to fit into the real system. This approach, in general, can succeed but requires a lot of trials and errors due to many unknown, hidden and implicit parameters in a real vehicle and real hydraulic circuit.

The authors of [2] claim active hydraulically interconnected suspension to be able to compensate the limitation of conventional active suspension systems such as high power consumption and low cost-effectiveness. In the paper, the authors propose a layout of active hydraulically interconnected suspension with a fuzzy logic controller implemented. Namely, the article focuses on fuzzy proportional-integral-derivative control as well as the optimal linear quadratic regulator. A half-car model was derived and combined with the model of the active hydraulically interconnected suspension system. The resultant system was simulated numerically with different control strategies and different excitation patterns. The robustness of controllers designed was also validated through simulations. The authors claim their results to have proved the effectiveness of the controllers involved by assessing the amount of roll angle reduction. The authors conclude that fuzzy proportional-integral-derivative controller demonstrated superior performance regarding its robustness and stability.

The authors derive two advanced controllers: fuzzy PID and LQR and perform comparative tests. Fuzzy PID shows better performance than LQR. However, this must be a result of improper signal filtering for LQR. According to textbooks [20] and [21] cannot be used in its pure form. It must be used in combination with a state observer which will perform state estimation and noise filtering. It requires a lot of novelty and effort to design something like fuzzy PID than to design an LQR with Kalman state observer. However, LQG controller is one of the best advanced control methods whereas fuzzy PID is not a common one and its performance and reliability are not studied well.

In paper [3] is derived a more complicated mathematical linear model of a roll-plane active hydraulically interconnected suspension system. The authors performed model parameters tuning to obtain a model that was able to predict the dynamics of a real system accurately. As of the year 2014, the authors claim to have made significant improvements to their new model as compared with all models derived previously. The authors verify their new model by simulations and similar experiments that were conducted. The simulations data were compared with the experiments and demonstrated right consistency between the numerical model and the real system. Thus, the authors concluded their new mathematical model to be valid and accurate. The critical hydraulic parameters were measured at the same time.

Paper [3] presents a thorough analytical derivation of half-car fitted with active hydraulically interconnected suspension which is followed by some experimental measurements. However the connection between the theory and the experiment is obscure. The paper introduces the model equations that are thorough and reproducible. Experimental tests demonstrate the performance of a real hydraulically interconnected suspension system.

In paper [22], the authors derive a frequency domain model of 4-degrees-of-freedom hydraulically interconnected suspension. The authors set up frequency models of the road surface and obtain power spectral density for such parameters as vertical acceleration and the roll acceleration. The effect of hydraulic parameters on suspension response is studied with fuzzy grey correlation. The influence degree of hydraulic parameters on the vertical motion mode and the roll mode is determined. The authors conclude that the vertical mode is more affected by the hydraulic valve which is connected to the hydraulic chamber. At the same time, the accumulators have more impact on the roll mode.

Paper [22] presents a systematic approach to hydraulic circuit parameters optimisation. The authors develop a methodology allowing one to study the impact of almost any parameter of the hydraulic circuit on the vibrational mode of the interest. However, it should be remembered that fuzzy methods are often subjective as they always imply a human choice of at least one variable essential to the outcome produced by the entire method.

In PhD thesis [23] the author presents a broad review of integrated control techniques of active vehicle chassis. The thesis discusses such integrated stability control systems as

- active normal load control,
- active aerodynamics control,
- active rear steering,
- hydraulically interconnected suspension,
- active anti-roll bar,
- electronic stability control,
- torque vectoring.

General information is given on all the above topics. Some calculations and simulations provided. However, the integrity of the thesis is questionable. The experimental part is missing.

In [24] the authors conduct a theoretical study of the lateral stability of a vehicle fitted with hydraulically interconnected suspension. The authors study the vehicle's yaw rate, slip angle and trajectory tracking ability. The authors conclude that roll stability cannot enhance the lateral stability of the vehicle but the lack of lateral stability can affect roll stability. The study investigates vehicle lateral stability using cornering responses and compares between anti-roll bars and hydraulically interconnected suspensions. The authors compare between the calculated actual path of the vehicle and the desired path which is definitely a novelty and a good benchmarking method. However, the study needs experimental support.

Paper [25] represents a novelty which is the invention of author researchers. In their research, the authors came up with a fundamentally new modification of the conventional hydraulically interconnected suspension system. Namely, the authors proposed to add an extra hydraulic accumulator to the existing hydraulic circuit which is why the new suspension system was named "Dual HIS", or simply "DHIS". The additional accumulator connects in parallel to the existing one on either side of the hydraulic circuit and not only it duplicates the action of the regular one but also shunts the action of the latter in accordance with parallel capacitor connection rule. This introduction of another functional element brings essentially new properties to the hydraulic circuit in particular and to the vehicle equipped with the DHIS system in general. According to [25], the new invention needs to be thoroughly examined before it can be reproduced commercially. Therefore, the authors derive a model of the new system which has a high degree of accuracy as well as high complexity. Given the model, the authors conduct an exhaustive study in order to verify and test their ideas in simulations using various approaches and graphs. Not only the authors use mathematical models in Matlab but they also involve another software named CarSim to build the computational model and compare between the two. The authors report their new DHIS system to show significant improvement of ride performance comparing with the conventional hydraulically interconnected suspension system which only has one hydraulic accumulator on each side and lacking many benefits that can be attained only with DHIS.

1.4.2 Summary of the Publications

The above papers represent the recent studies conducted on the subject of hydraulically interconnected suspensions both passive and active. They successively introduce such methodologies as analytical modelling, frequency domain model identification, using advanced control methods. Analytical modelling starts with simplified linear models and finishes with accurate models involving non-linear effects. Experimental methodology develops from measuring responses to road roughness to the proposition of frequency domain system identification prior to the controller design. Advanced control methods only are used for the system which can be explained by the complexity of the system and practical challenges when using simple control methods such as PID, for example.

Overall the papers discussed above provide although not always self-consistent but a sufficient foundation for current research. Parts and bits of those were adopted throughout the current project and the corresponding papers are cited where necessary in the body of the thesis.

1.5 Research Objectives

The ultimate objective of the project was to build an active HIS prototype and demonstrate the feasibility of active HIS system and its effectiveness as compared to passive anti-roll HIS system. In this PhD dissertation, we pursued multiple directions of research. Not only they included theory, modelling and simulations but also a significant experimental component with 3D CAD drafting, manufacturing custom parts and building the assemblies. The author spent a lot of time in the lab commissioning, tuning system parameters and making everything to work together. As a result of these efforts, the author of the thesis is delighted to say that all research components eventually met in perfect agreement and formed a solid picture of current research with the unification of theory, modelling, simulation and the experiment. Below, are discussed the main research objectives the author pursued in this project.

1.5.1 Theoretical Component

Our theoretical studies were concentrated around the major aspects of active hydraulically interconnected suspension. Mainly, our studies refer to Mechanical Engineering and the adjacent fields. Thus, we used Lagrange Mechanics while deriving the equations of motion of the mechanical system. Hydraulic Circuits Theory was used to obtain the equations for active HIS. After that, the entire half-car with active HIS system was modelled and further studied. Linear Dynamics Theory was used in the analysis of free vibration and forced vibration responses of the system. We used Classical Control Theory to find the gain and phase stability margins that are necessarily accounted for in the controller design. We also analysed the equations of motion of the system for the subject of potential order reduction. Modern Control Theory was used for control system design, in which we altered the poles of the original system with Linear Quadratic Regulator and alternatively with Ackerman pole placement technique.

1.5.2 Practical Component

Here we discuss the practical component of our research work which was primarily focused on building the Active HIS Prototype. In order to be able to verify our theoretical findings, we needed to design and build an experimental setup. Our design was based on the existing Half-Car Testing Rig located in the Dynamics Lab in UTS City Campus Building 11 Level B4. The existing rig was built by the lab engineer Chris Chapman and the former PhD student Wade Smith, who worked under the supervision of Prof. Nong Zhang and graduated in 2005. Originally the rig was built for passive tests only, such as the drop test and the road disturbance test. Therefore, we designed and built two new actuators for active HIS tests, namely the HIS Actuator and the Force Moment Disturbance Actuator. The existing Half-Car Rig was successfully augmented with the actuators and gained a possibility of performing angular dynamics tests about the roll axis of the setup.

1.5.3 Control System Implementation

Not only the author was building the experimental setup, but also he worked intensively on the implementation of the control system. And thus, control system design and implementation constitute an individual research component. One should remember that it is always a challenge to get a control system working in practice rather than in simulations since the number of third factors affecting your simulated designs is countless. If we name some of them, it will be the noise in the sensors, electromagnetic interference, unexpected phase lags in the hardware, backlashes and gaps in the mechanical system, model uncertainties and hidden parameters, unknown variables, sampling errors, numerical errors, etc. Therefore, a real control system has to have a high level of tolerance to the above factors. And this is not only a procedure to follow step-by-step but rather an art of designing a control system, where one needs to apply all their skill and expertise to get things work correctly and as expected by compromising between a lot of controversial parameters and being constrained by the limitations of the hardware.

1.5.4 Experimental Component

The experimental component was one of the main parts of this research. The author intended to get things done properly and to have a sound foundation under each step and each milestone of the project. Rather than trial and error which is often practised in research, the author believes in the heritage of European Engineering School which provides one with a comprehensive and self-consistent theoretical background in any engineering field. Before the first experiment could be conducted there was a great number of preparations that were done. Once all preparations were finished, and the setup became fully operational, the author dedicated a few months to purely experimenting. The methodology chosen implied the direct measurement of the frequency response of the system over the range of frequencies starting from 0.1 Hz to 10 Hz with an increment of 0.1 Hz which resulted in up to 50 - 70 experimental runs followed by data processing and analysis every time. This type of experiment was conducted for all the subsystems of the setup multiplied by the number of different controllers and control system settings that were tested. Also, we also conducted the drop test as an analogy to step input response imitating the real situation of a sudden harsh steer movement such as that defined by the NHTSA J-turn or Fishhook maneuver.

1.6 Methodology

Throughout the current project, the author utilised his expertise in various engineering fields. The methodology was borrowed from such subjects and disciplines as Lagrange Mechanics, Mechanical Vibration, Hydraulics, Fourier Analysis, Fourier Transform, Laplace Transform, z-Transform, Linear Dynamics, Control Systems and others. In this section, we review the most significant methods and techniques. We list the methods in sequential order as they were used in our work.

1.6.1 Lagrange Method for a Non-Conservative System

Although the half-car model can be assumed to be linear, it is yet an example of a non-conservative system due to the damping elements represented by the suspension dampers. Moreover, the model takes multiple force inputs such as HIS forces exerted at the suspension struts that can be either semi-active or fully active, and the external lateral force as the disturbance. Therefore, one needs to utilise Lagrange mechanics for systems with non-conservative forces that also includes Rayleigh dissipation function in charge of the dissipation of energy.

1.6.2 Hydraulic Circuit Analysis

We obtain the equations for the hydraulic system using Hydraulic Impedance Method. The method is helpful for the analysis of linear hydraulic circuits with lumped elements such as the HIS system is assumed to be. Although the HIS system is not exactly linear and neither it has all its parameters lumped, the accuracy of the method is sufficient for our purposes.

1.6.3 Forced Vibration Experiment

As known from theory, a Linear Time Invariant system responds to a sine-wave excitation with a sine-wave of the same frequency but perhaps of different amplitude and phase. This property of the LTI systems was exploited in the experimental part of our research. By subjecting the system to a sine-wave excitation over the range of frequencies of the interest we measured the system's responses that were further analysed.

1.6.4 Fourier Analysis

We analysed the data collected in Forced Vibration Experiment with Fourier Analysis. By taking Fast Fourier Transform of both the signals: the input disturbance and the output of the system we could accurately measure the magnitude of the response with the input and the phase angle between the two. These data were further graphed on a Bode Plot and used for model identification in the frequency domain.

1.6.5 State-Feedback Control

Since the performance of model-independent controllers such as PID is very limited, and the feedback gains are severely constrained to the stability of the system, one can design a better controller with state-feedback techniques such as the Linear Quadratic Regulator or the Ackerman Direct Pole Placement. In the first one, the LQR problem is formulated, and the variation equation is solved with the penalties given to the states that are specified by a control engineer. The solution results in a vector of gains to be multiplied by the states of the system to alter closed-loop poles. In the Ackerman Pole Placement, one can directly alter the position of system's poles with the Ackerman Formula. Both the methods require a fast state-observer.

1.6.6 State Observer Design

One needs to use a state observer to get the estimated system states. There can exist a variety of observers, and however, in this project, we aimed at using the most reliable and efficient ones. The simplest state observer is the Leuenberger State Observer. It has lowest computation cost of all, but the downside of it is that it has phase lag. Leuenberger State Observer is designed with Ackerman Formula and in the same manner as Direct Pole Placement. One needs to position the poles of the observer farther away from the origin on the 's' plane than the poles of the system. This fact signifies that the observer will converge faster than the settling time of the system.

Another example of another reasonable state observer is Kalman State Observer. Kalman State Observer is the best regarding its filtering capability which is mathematically proved in Control Theory as a theorem. For Kalman State Observer design one needs to specify the two variables: the *a' priori* uncertainty of the model and the *a' posteriori* uncertainty of the measurement. Kalman State Observer converges fast having only insignificant phase lag as compared to other observers.

1.7 Thesis Outline

To summarise, here we give an overview of current research with detailed explanations of key milestones and steps undertaken for successful completion of the project:

- formulated an objective: to build a working prototype of active HIS system,
- performed an estimated calculation of the key parameters of the system,
- modelled the system with the equations and performed simulations,
- designed and built a custom hydraulic actuator for the HIS system,
- designed and built an actuator to imitate lateral force on the system,
- conducted forced vibration experiments to identify the transfer functions,
- designed an LQG compensator for the system,
- deployed the LQG compensator on a micro-controller,
- did commissioning work to make the setup functional,
- performed experimental tests to validate the effectiveness of active HIS.

Here we also briefly review the thesis outline. In Chapter 2 are discussed the theoretical fundamentals current research is based upon. In Chapter 3 we present our work on upgrading the existing half-car testing rig. Two essential upgrades are the roll actuator to simulate the external roll moment and the actuator for active hydraulically interconnected suspension. In Chapter 4 we derive mathematical models of the setup and design a controller for our models. In Chapter 5 we perform simulations pursuing two primary objectives: to verify the feasibility of proposed actuator for roll angle reduction and to obtain the estimates of the variables that are important. In Chapter 6 we discuss the commissioning work that has been done including signal conditioning, sensor calibrations and coding. In Chapter 7 we perform identification experiments to identify the critical system sub-models. In Chapter 8 we use the models obtained for the design of a real LQG compensator which is to work with the physical system. In Chapter 9 we validate the compensator experimentally and conduct a series of identifications in the frequency domain as well as the time domain drop tests. In Chapter 10 we conclude the overall status of the project and the research outcomes.

Chapter 2

Fundamentals

In this chapter, we refer to the theoretical foundations that our research is based upon. We find it unnecessary to make these articles complete and comprehensive. On the contrary, we only convey the essential practical information on each of the topics. For further reading, bibliographic references are given in the text.

2.1 Non-Conservative Lagrange Equation

Since half car is a complex model with many parameters, multiple inputs and outputs (MIMO) one should use Lagrange formalism to assure that no mistakes occur. As the system has dampers and external force inputs the Lagrange equation will have a non-conservative term. Consider a system with n lumped inertia elements and m springs/dampers. Here follow the expressions for the kinetic 2.1, potential 2.2 energy and the Rayleigh dissipation function 2.3.

$$\mathcal{T} = \sum_{i=1}^{n} \frac{1}{2} m_i \dot{q}_i^2 \tag{2.1}$$

In formula 2.1 for kinetic energy, m_i should be understood as inertia, either a lumped mass or moment of inertia, and q_i is the generalised coordinate which can be either linear or angular displacement of the i-th inertia element. The contributions are summed over N inertia elements indexed by i.

$$\mathcal{U} = \sum_{j=1}^{m} \frac{1}{2} k_j \Delta q_j{}^2 \tag{2.2}$$

In the half-car model potential energy is accumulated in springs. Therefore, in 2.2 the summation is across m springs indexed by j. Spring deflections Δq_j are expressed through the generalised coordinates q_i.

$$\mathcal{D} = \sum_{j=1}^{m} \frac{1}{2} b_j \Delta \dot{q}_j{}^2 \tag{2.3}$$

In 2.3, b_j are the damping coefficients. The summation is across all dampers that are assumed to be as many as the springs. To exclude some of the dampers (for instance, tire damping), one can set $b = 0$ for those that are excluded from the model.

$$\mathcal{L} = \mathcal{T} - \mathcal{U} \tag{2.4}$$

$$\frac{d}{dt}\frac{\partial \mathcal{L}}{\partial \dot{q}_i} - \frac{\partial \mathcal{L}}{\partial q_i} + \frac{\partial \mathcal{D}}{\partial \dot{q}_i} = \mathcal{F}_i \tag{2.5}$$

$$\frac{d}{dt}\frac{\partial \mathcal{T}}{\partial \dot{q}_i} + \frac{\partial \mathcal{D}}{\partial \dot{q}_i} + \frac{\partial \mathcal{U}}{\partial q_i} = \mathcal{F}_i \tag{2.6}$$

As per [26], Lagrange equation of a non-conservative system is given by 2.6, where F_i is the generalised force which can be either linear force or angular force moment applied to i-th inertia element. Thus, one obtains n equations of motion correspondent to n inertia elements of the system. Each individual equation of motion is of the kind of 2.7. Given n simultaneous equations we can organise them into a single equation in a matrix form 2.8, where $q = [q_1 \dots q_n]^T$, $F = [f_1 \dots f_n]^T$ and M, B, K being square matrices of size $[n \times n]$.

$$m_i \ddot{q}_i + b_i \dot{q}_i + k_i q_i = f_i \tag{2.7}$$

$$M\ddot{q} + B\dot{q} + Kq = F \tag{2.8}$$

2.2 Huygens–Steiner Theorem

Huygens–Steiner theorem is also known as Parallel Axis theorem [27]. The theorem states the relation between the intrinsic body moment of inertia and the moment of inertia about an arbitrary axis which is parallel to one of the intrinsic rotation axis of the body (see figure 2.1). If a body of mass m has an intrinsic rotation axis x with an intrinsic moment of rotation I_{xx}. Then the moment of rotation I'_{xx} about the parallel axis x' is given by formula 2.9, where d is the separation distance between the axis.

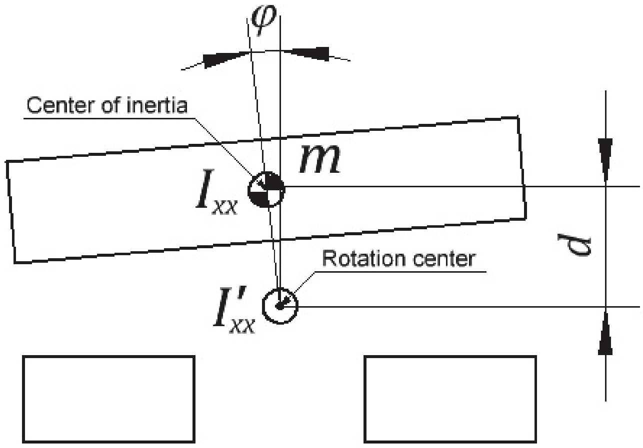

Figure 2.1: Illustration to Huygens-Steiner theorem

$$I'_{xx} = I_{xx} + md^2 \tag{2.9}$$

2.3 Ball-Screw Torque Calculations

According to [28], ball-screw torque is classified into four categories: driving torque, back-driving torque, holding torque and drag torque. For simplicity, in this section, we do not consider drag torque but will focus on the other three kinds of ball-screw torque. As per [28], the normal driving torque is given by formula 2.10. Formula 2.11 gives the back-driving torque. And the holding torque equals the back-driving torque under an assumption of no drag.

$$T_d = \frac{F\,p}{2\pi\,\eta_d} \tag{2.10}$$

$$T_b = \frac{F\,p\,\eta_b}{2\pi} \tag{2.11}$$

Here F is the ball-screw axial load in N, p is the lead pitch in mm/rev, η_d is the normal ball-screw efficiency and η_b is the reverse ball-screw efficiency. Torques T_d and T_b are measured in N.m.

2.4 Hydraulic Impedance Method

Hydraulic impedance method was used for analysis of the HIS circuit as discussed in [29]. As typical of an impedance method of analysis, the method is based on the algebraization of the differential equations obtained from the Kirchhoff's laws through Fourier transform followed by solving the equations simultaneously in the frequency domain.

2.4.1 Hydraulic Circuit Elements

As per [30] the elements of a hydraulic circuit for analysis can be replaced with their idealised analogues, i.e. hydraulic resistance, hydraulic inertance and hydraulic capacitance. The parameters of idealised elements are assumed lumped, and their action is defined by the formulas similar to those of Electrodynamics. See equations 2.12, 2.13 and 2.14. Note that here q is the volumetric hydraulic flow in (m^3/s) and p is the pressure in (Pa).

$$p_2 - p_1 = Rq \tag{2.12}$$

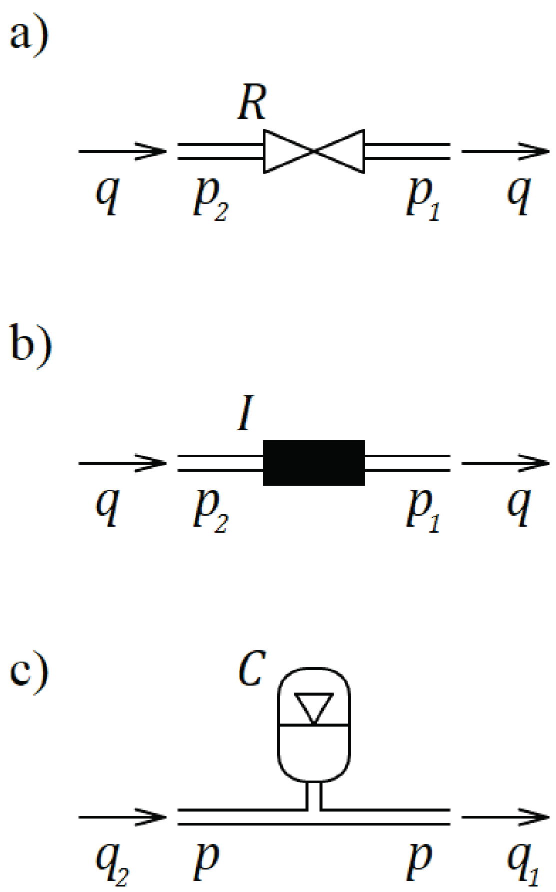

Figure 2.2: Hydraulic elements as analogous to electric circuits: a) - hydraulic resistance, b) - hydraulic inertance, c) - hydraulic capacitance

$$p_2 - p_1 = I\frac{dq}{dt} \tag{2.13}$$

$$q_2 - q_1 = C\frac{dp}{dt} \tag{2.14}$$

2.4.2 Hydraulic Resistance and Hydraulic Inertance

On the other hand, according to [31] R, I and C can be expressed through fundamental physical properties of the fluid and the parameters of the hydraulic components that constitute the circuit. Here we give the formulas for some simple cases that are described in the literature.

If there is a fluid of density ρ (kg/m^3) and of dynamic viscosity μ (Pa.s), then for a long pipe of inner radius r and length l hydraulic resistance is expressed by 2.15. Hydraulic inertance, in turn, is given by 2.16.

$$R = \frac{8\mu l}{\pi r^4} \tag{2.15}$$

$$I = \frac{\rho l}{\pi r^2} \tag{2.16}$$

2.4.3 Hydraulic Capacitance

As per the hydraulic capacitance of an accumulator such as shown in figure 2.2 c), there can be two possibilities: a mechanical spring loaded accumulator and a gas spring accumulator. Equation 2.17 gives the definition of capacitance. In case of a gas spring, according to [32], it follows fundamental adiabatic equation 2.18 which is more commonly known as 2.19. However, equation 2.19 is only a consequence of 2.18 and therefore it is preferable to use 2.18 instead. Thus, out of 2.18 we can derive an expression for gas accumulator capacitance 2.20. Here γ signifies the specific heat ratio of the gas the accumulator is charged with.

$$C = \frac{dV}{dP} \tag{2.17}$$

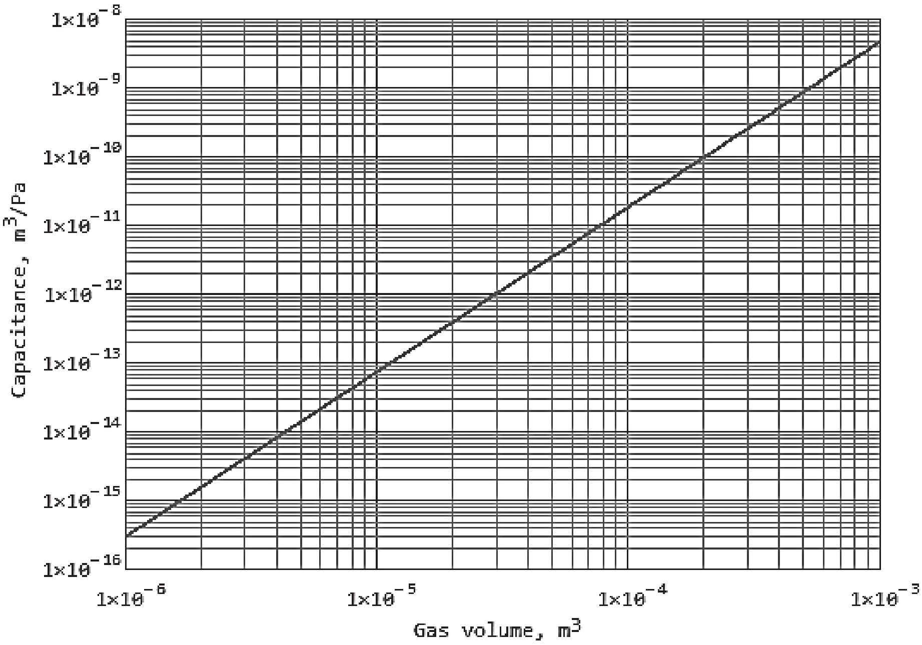

Figure 2.3: Gas accumulator capacitance as a function of gas volume at $P_0 = 2 \times 10^6$ (Pa) initial gas pressure, $V_0 = 0.16 \times 10^{-3}$ (m^3) initial gas volume and the specific heat ratio $\gamma = 1.4$ for N_2

$$\gamma\, P\, dV + V\, dP = 0 \tag{2.18}$$

$$P\, V^{\gamma} = \text{const} \tag{2.19}$$

$$C = \frac{1}{\gamma}\frac{V}{P} \tag{2.20}$$

One can see that in 2.20 capacitance is a non-linear function of the gas volume and pressure. In figure 2.3 is given a log-scale graph of capacitance as a function of gas volume.

In the case of mechanical spring we need to introduce the spring stiffness k (N/m) and the accumulator membrane area A (m^2). The capacitance of the accumulator is derived from the mechanical spring equation 2.21, x (m) being the spring displacement. The capacitance then is given by 2.22 and it is independent of the pressure and the volume of accumulated fluid.

$$F = kx, \quad PA = k\frac{V}{A}, \quad V = \frac{A^2}{k}P \tag{2.21}$$

$$C = \frac{A^2}{k} \tag{2.22}$$

2.4.4 Adiabatic Spring

With adiabatic spring it is important to distinguish between the two laws of molecular kinetic theory: the adiabatic process law and the isothermal process law (see [33] for details). While the adiabatic law governs the instantaneous action of springs, the charging process is defined by the isothermal law. An accumulator is prepared to work by initially charging it with precharge pressure P_0. At this moment the accumulator is assumed to be filled with gas only, having no liquid in it. If the accumulator volume is V_0, then the isothermal process is characterised by a constant 2.23.

$$P_0V_0 = \text{const} \tag{2.23}$$

After precharging the accumulator, the hydraulic system can be charged to working pressure P which is usually higher than P_0. In this case, the accumulator will follow an isotherm and settle down in a new state PV. According to the isothermal process, the law follows equation 2.24.

$$PV = P_0V_0 \tag{2.24}$$

However, when working as a suspension spring, the accumulator is governed by adiabatic law. Provided Q is the volumetric flow and the capacitance C is not a constant, an accumulator can be precisely modelled with the equation 2.25.

$$Q = \frac{d}{dt}(C\,P) \tag{2.25}$$

2.4.5 Kirchhoff's Laws

Kirchoff's laws are the two laws that apply in many engineering areas such as, for example, electric circuits as discussed in [34]. However, Kirchoff's laws are also of particular use when formalising hydraulic circuit equations. There are two major laws to be addressed commonly known as the current law and the voltage law. In analogy to electric circuits in hydraulics one would have the laws for the volumetric flow of the fluid and the pressure of the fluid respectively.

The volumetric flow law, see equation 2.26, postulates that the algebraic sum of currents in a junction equals zero. This is mainly an admission of the fact that no fluid can accumulate in a junction. The pressure law, see equation 2.27, in turn, postulates that the algebraic sum of pressure drops across a loop in a circuit equals zero. This is because as we monitor the pressure along a closed path in a circuit the point where we start and end up is the same and thus, it must have the same pressure in it. An illustration of the volumetric flow law can be seen in figure 2.4(a), and for the fluid pressure - in figure 2.4(b).

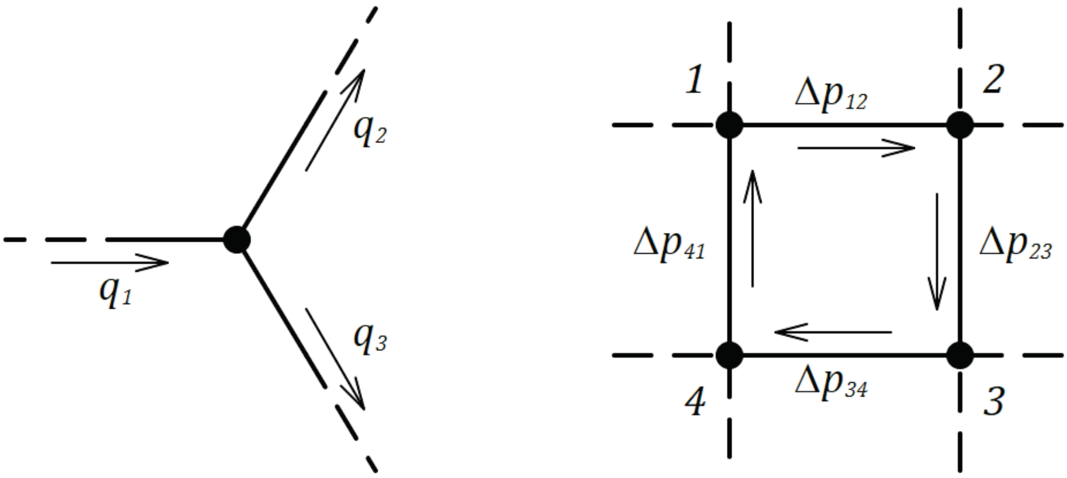

(a) First Kirchhoff's law (b) Second Kirchhoff's law

Figure 2.4: An illustration to Kirchhoff's laws

$$\sum_{i=1}^{n} q_i = 0 \tag{2.26}$$

$$\sum_{i=1}^{n} \Delta p_i = 0 \tag{2.27}$$

2.5 Second Order Systems

Second order systems are most common. Therefore, the properties of second order systems are of superior importance in such disciplines as Mechanical Vibrations, Linear Dynamics and Control Theory. Moreover, as per the Gauss's Fundamental Theorem of Algebra [35], any polynomial can be rearranged as a multiplication of first-order terms and irreducible quadratic trinomials. Note that, the latter are irreducible only in real numbers $\mathbb{R}$, although they have their roots in complex numbers $\mathbb{C}$. In this section, we review main ideas about second order systems in general as they are essential for understanding any higher order dynamical systems.

$$\ddot{x} + 2\gamma\dot{x} + \omega_n^2 x = 0 \tag{2.28}$$

Consider a homogeneous second order differential equation 2.28. Here, $x(t)$ being the variable of the process, γ - the decay constant, and ω_n - the natural frequency of the process. There are various ways of solving equation 2.28 which is commonly known as the equation for harmonic oscillator with dissipation. We are going to find the solution by applying Laplace transform to the equation, making use of the remarkable property of Laplace transform 2.72. Thus we obtain 2.29, where $\hat{x}(s) = \mathcal{L}\{x\}(s)$ is the Laplace image of $x(t)$. If $\hat{x}(s)$ is a non-zero function we can divide both parts of 2.29 by $\hat{x}(s)$ and thus obtain the characteristic equation 2.30.

$$s^2\,\hat{x}(s) + 2\gamma\,s\,\hat{x}(s) + \omega_n^2\,\hat{x}(s) = 0 \tag{2.29}$$

$$\begin{gathered} \lambda^2 + 2\gamma\,\lambda + \omega_n^2 = 0 \\ (\lambda - p_1)(\lambda - p_2) = 0 \end{gathered} \tag{2.30}$$

$$
\begin{aligned}
p_{1,2} &= -\gamma \pm i\sqrt{\omega_n^2 - \gamma^2} \\
p_{1,2} &= -\gamma \pm i\,\omega
\end{aligned}
\tag{2.31}
$$

Equation 2.30 is a quadratic equation with respect to variable s and has two roots $p_{1,2}$. In the case when natural frequency is greater than the damping factor $\omega_n > \gamma$ the roots can be express as shown in equation 2.31. This corresponds to general solution of the homogeneous equation 2.29 in the form shown in 2.32.

$$
x(t) = A\, e^{-\gamma t} \sin(\omega t) \tag{2.32}
$$

If we introduce a new variable ζ (see equation 2.33) which, according to [21], is commonly referred to as the damping ratio, then we can rewrite the other variables: $p_{1,2}$, γ and ω, - in terms of ζ (see 2.34). Yet another variable that often can be more convenient to work with is the specific time of the process τ - the reciprocal of γ.

$$
\zeta = \frac{\gamma}{\omega_n} \tag{2.33}
$$

$$
\begin{aligned}
p_{1,2} &= -\omega_n \left(\zeta \pm j\sqrt{1-\zeta^2} \right), \\
\gamma &= \omega_n \zeta, \\
\omega &= \omega_n \sqrt{1-\zeta^2}, \\
\tau &= \frac{1}{\omega_n \zeta}
\end{aligned}
\tag{2.34}
$$

As seen in figure 2.5, the location of poles $p_{1,2}$ can vary depending on the relation between γ and ω_n. The poles usually come in twins mirrored about the real axis unless the damping ratio equals one $\zeta = 1$. Also, in the figure, one can see that natural frequency ω_n is the magnitude of poles $p_{1,2}$, whereas the actual frequency of oscillation ω being the imaginary part of $p_{1,2}$ and the decay constant γ - the real

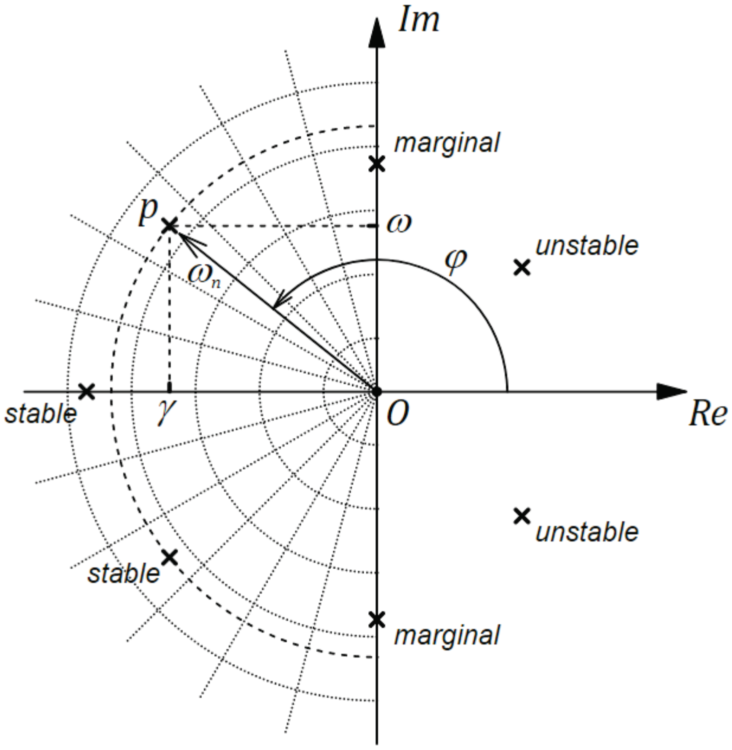

Figure 2.5: Pole-zero plot

part. If a pole lies in the right half-plane, then such system is called unstable, and it diverges to infinity with time. If a pole lies in the left half-plane, then the system is stable, and the oscillation of the system decays with time converging to a constant. If a pole lies on imaginary axis, then such system is marginal and in theory, once excited will never stop oscillating. One can also see that the damping ratio ζ is just a cosine of the polar angle φ. The system can be classified by its damping ratio as: a) under-damped $0 < \zeta < 1/\sqrt{2}$, b) critically damped $\zeta = 1/\sqrt{2}$, or c) over-damped $\zeta > 1/\sqrt{2}$. An under-damped oscillator tends to oscillate more before it settles down. An over-damped oscillator does not oscillate at all and settles down slowly due to excessive damping. A critically damped oscillator provides an optimal compromise between the damping and the oscillation (see figure 2.6). The general rule is that a pair of poles (or a single pole if only real) that is farther away from the imaginary axis to the left provides faster settling.

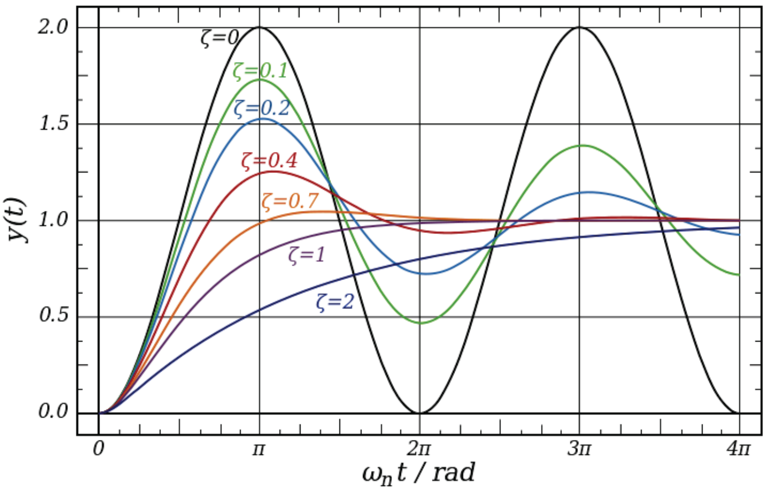

Figure 2.6: Damping ratio

2.6 Transfer Function Representation

A linear dynamics second order equation can be represented in general as shown in 2.35. After applying Laplace transform to both sides one can obtain 2.36. If $A_0, A_1, A_2, B_0, B_1, B_2$ are matrices and u, y - vectors, then the transfer function matrix can be obtained as 2.37.

$$A_2\ddot{y} + A_1\dot{y} + A_0 y = B_0 u + B_1\dot{u} + B_2\ddot{u} \tag{2.35}$$

$$s^2 A_2\hat{y} + sA_1\hat{y} + A_0\hat{y} = B_0\hat{u} + sB_1\hat{u} + s^2 B_2\hat{u} \tag{2.36}$$

where $\hat{u}(s) = \mathcal{L}\{u(t)\}$ and $\hat{y}(s) = \mathcal{L}\{y(t)\}$.

$$\begin{aligned} H(s)_{[n\times m]} &= D(s)^{-1} \cdot N(s) \\ &= \left(s^2 A_2 + sA_1 + A_0\right)^{-1} \cdot \left(B_0 + sB_1 + s^2 B_2\right) \end{aligned} \tag{2.37}$$

Here the numerator-matrix is denoted by $N(s)$ and the denominator-matrix - by $D(s)$.

2.6.1 Discrete Transfer Function

Consider a discrete transfer function $H(z)$, see equation 2.38. A discrete transfer function defines the relation between two variables: the input $u(t)$ and the output $y(t)$, both the input and the output being discrete variables: u_k and y_k, where k is the time lag index. For example, y_0 would signify the output value at the current moment of time. Similarly, for instance, u_1 would mean the input value at the previous iteration, i.e. one sampling period ago in the past, and so on. The operator z^{-k} is the lag operator. When z^{-k} acts on a variable it yields the value of the variable lagging by k sampling periods, e.g. the expression $z^{-2}u$ denotes the delayed value of u, namely $z^{-2}u = u_2$. Thus, we can write down an equation 2.39 which states the relation between two discrete variables. The discrete equation such as 2.39 can be then implemented on a micro-controller in the form 2.40

$$H(z) = \frac{b_0 + b_1 z^{-1} + b_2 z^{-2} + \cdots}{1 + a_1 z^{-1} + a_2 z^{-2} + \cdots} \tag{2.38}$$

$$\left(1 + a_1 z^{-1} + a_2 z^{-2} + \cdots\right) y = \left(b_0 + b_1 z^{-1} + b_2 z^{-2} + \cdots\right) u \tag{2.39}$$

$$y_0 = -\left(a_1 y_1 + a_2 y_2 + \cdots\right) + b_0 u_0 + b_1 u_1 + b_2 u_2 + \cdots \tag{2.40}$$

2.7 State-Space Representation

Given a mechanical second order equation such as 2.41 one can transform it into a state-space equation of the form of 2.42 as shown in 2.43, 2.44, 2.45 and 2.46. In some situation the formulas may slightly differ. The poles of the system can be found, then, as eigenvalues of $\mathcal{A}$.

$$M\ddot{y} + C\dot{y} + Ky = f \tag{2.41}$$

$$\begin{aligned} \dot{x} &= \mathcal{A}x + \mathcal{B}u \\ y &= \mathcal{C}x + \mathcal{D} \end{aligned} \tag{2.42}$$

$$\mathcal{A} = \begin{bmatrix} [\,0\,]_{n\times n} & [\,I\,]_{n\times n} \\ -M^{-1}K & -M^{-1}C \end{bmatrix} \tag{2.43}$$

$$\mathcal{B} = \begin{bmatrix} 0 \\ M^{-1} \end{bmatrix} \tag{2.44}$$

$$\mathcal{C} = \begin{bmatrix} I \end{bmatrix} \tag{2.45}$$

$$\mathcal{D} = \begin{bmatrix} 0 \end{bmatrix} \tag{2.46}$$

2.7.1 Hankel Singular Values of Dynamic System

As per [36], Hankel singular values of a dynamic system provide a measure of energy attributed to each of the states of the dynamic model. Hankel singular values can be used for balanced model truncation in which high energy states are retained and low energy states can be discarded and ignored. In this thesis we are using Hankel singular values to make conclusions about the effective order of the dynamic model derived for a half-car equipped with active hydraulically interconnected suspension system.

According to [37], Singular Value Decomposition (SVD) has been widely applied in engineering problems, such as System Identification, Model Reduction, Vibration Control, and Sensor Placement, and so forth. Although in our research was used a ready function from Matlab package, it is important to understand how Hankel singular values originate so that we could further use them educated way.

If $y(t)$ is represents impulse displacement response, N - the number of modes, r being the index of mode, k - the matrix size, ω - the natural frequency, ζ - viscous damping, A - amplitude and Δt - sampling interval, then one can obtain Hankel matrix of a dynamic system as follows.

Firstly, the impulse response of displacement can be represented as

$$y(t) = \frac{1}{2}\sum_{r=1}^{N}\left(\bar{A}_r e^{\lambda_r t} + \bar{A}_r^* e^{\lambda_r^* t}\right) \tag{2.47}$$

where

$$\begin{aligned} \lambda_r, \lambda_r^* &= \zeta_r\omega_r \pm j\omega_r\sqrt{1-\zeta_r^2} = \omega_r e^{\pm j\alpha_r} \\ \bar{A}_r &= -jA_r \qquad \bar{A}_r^* = jA_r \\ \alpha_r &= \cos^{-1}(-\zeta_r) \end{aligned} \tag{2.48}$$

Then, k-th sampled data can be abbreviated as

$$y(k\Delta t) = y(t_k) = y_k = \frac{1}{2}\sum_{r=1}^{N} A_r\left(-je^{\lambda_r t_k} + je^{\lambda_r^* t_k}\right) = \sum_{r=1}^{N} A_r e^{-\zeta_r\omega_r t_k}\sin\left(\sqrt{1-\zeta_r^2}\omega_r t_k\right) \tag{2.49}$$

After that the sampled data can be sequentially filled to form a Hankel matrix H, as follows

$$H_{m\times n} = \begin{bmatrix} y_0 & y_1 & \cdots & y_{n-1} \\ y_1 & y_2 & \cdots & y_n \\ \vdots & \vdots & \cdots & \vdots \\ y_{m-1} & y_m & \cdots & y_{m+n-2} \end{bmatrix} \tag{2.50}$$

Now, without loss of generality we can let $m = n = k$ and derive Hankel singular values λ as the eigenvalues of Hankel matrix H

$$\det\left|H^T H - \lambda I\right| = 0 \tag{2.51}$$

2.8 Hierarchy of Control Methods

The author of thesis applied significant effort to learning about modern control methods. From that experience the author would like to share a diagram which summarises and classifies linear control methods and explains relations between them, see 2.7.

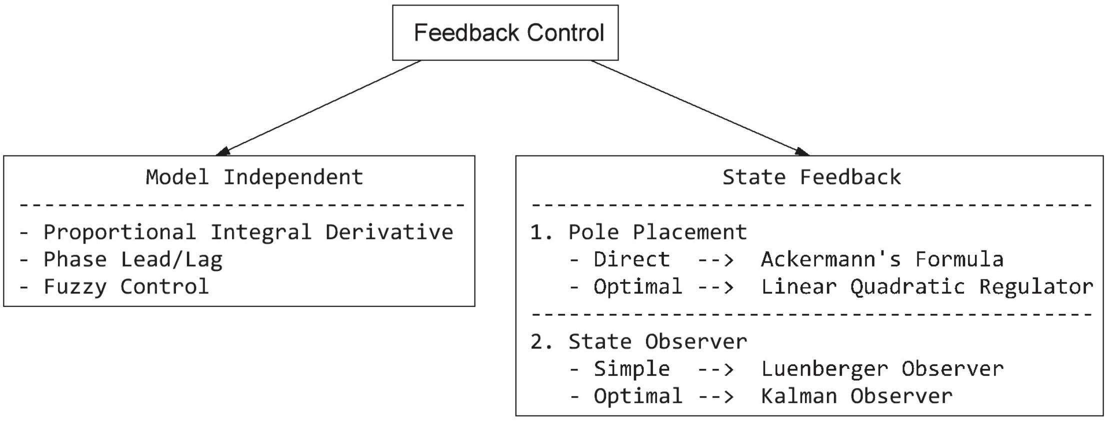

Figure 2.7: Classification of control methods

As seen in the figure, linear control methods can be divided into two categories: model independent and model dependent, i.e. state feedback. Model-independent methods are mainly represented by PID, phase lead and phase lag compensator. State feedback methods include pole placement techniques such as direct pole placement and optimal pole placement. While Ackermann's formula represents direct pole placement, Linear Quadratic Regulator being a functional solution leading to optimal pole placement concerning minimising a cost-function.

Another aspect of state feedback is choosing the observer. There can be different state observers. However, we will discuss the two most common ones being Luenberger State Observer and Kalman State Observer. Luenberger State Observer implements the simplest state observer possible. It is easy to implement, and it is cost-effective computation-wise. The disadvantage of Luenberger observer is its rigidity. The observer is fixed and does not adapt to changing process conditions. This disadvantage is overcome by the Kalman state observer which is indeed adaptive. Kalman state observer is somewhat harder to implement and tune, but it is much more robust and reliable as compared to Luenberger observer. From a practical point of view, the Kalman state observer is the most common one in the areas where human life is entrusted to a machine. Kalman observer is used widely in the airspace, rocketry, navigation, naval, production lines and many other industries.

In our project we proved, theoretically and experimentally, model-independent methods to fail for our models. Therefore, the scope of our consideration will focus on state feedback methods such as LQR, LQG and Kalman state observer.

2.9 State Feedback Control

As per [38], state feedback controllers represent a prominent category of advanced control methods. In state feedback, the system's state variable is multiplied by the feedback gains vector to calculate the control effort which is required to stabilise the plant. The diagram 2.8 shows the general idea of state feedback control. Note that the feedback gain vector K can be found through different ways either by solving a linear quadratic regulator problem or by direct pole placement.

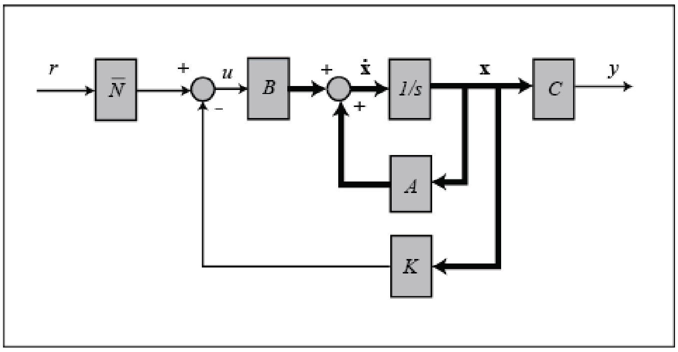

Figure 2.8: State feedback control

2.9.1 Ackermann's Formula

Ackermann's formula [39], [40] is a control system design method developed for solving the pole allocation problem. In control systems design, one of the primary problems is the design of controllers that will change the properties of the plant in a particular way by altering the location of plant's poles to a more suitable and often more stable region. Ackermann's formula is an efficient pole allocation method which allows one to move poles of the plant to an arbitrary desired location, in theory. In practice, of course, relocation of the poles is limited by actuator capabilities.

Consider a state-space [41] of a linear time invariant model 2.52

$$\begin{aligned} \dot{x}(t) &= Ax(t) + Bu(t) \\ y(t) &= Cx(t) \end{aligned} \tag{2.52}$$

Then the transfer function of the system can be found as 2.53

$$G(s) = C(sI - A)^{-1}B = C\frac{\mathrm{Adj}(sI - A)}{\det(sI - A)}B \tag{2.53}$$

From 2.53 one can see that the denominator of the transfer function is given by the characteristic polinomial of A i.e. the poles of the system are also the eigenvalues of A.

If the system is unstable, or has a slow response or any other characteristic that does not meet the design criteria, it could be advantageous to relocate the poles. The realization given by the state-space, however, represents the intrinsic dynamics of the system, and sometimes cannot be altered. One approach to this problem might be to create a feedback loop with a gain K that will feed the state variable into the input.

If the system is controllable, then it will feature an input $u(t)$ such that any initial state x_0 can be transferred to any other state $x(t)$. Given that, a feedback loop can be introduced to the system with the control input $u(t) = r(t) - Kx(t)$, where $r(t)$ being the reference signal, see 2.9.

Then, the new dynamics of the system will be described by 2.54

$$\begin{aligned} \dot{x}(t) &= Ax(t) + B[r(t) - Kx(t)] = (A - BK)x(t) + Br(t) \\ y(t) &= Cx(t) \end{aligned} \tag{2.54}$$

In this new realisation the poles will be defined by the eigenvalues of the new ma-

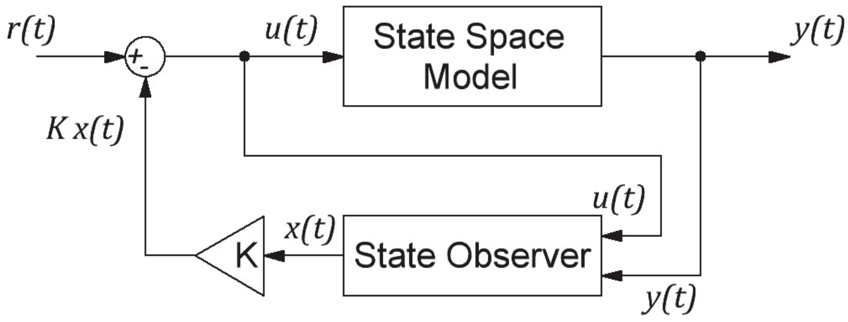

Figure 2.9: Concept of state feedback control

trix $\det[sI-(A-BK)]$. Let $D(s)$ be the desired characteristic polynomial. Then one can find gain vector K with the formula 2.55, where $D(A)$ is the desired characteristic polynomial evaluated at matrix A.

$$K = [0, 0, \cdots, 0, 1]C^{-1}D(A) \tag{2.55}$$

It should be also mentioned that Matlab software package contains an embedded function for robust pole placement which implements the numerical algorithms discussed in [?] and [?].

2.9.2 Linear Quadratic Regulator

According to [20] Linear quadratic regulator minimises a quadratic cost-function $J(u)$ for a linear time invariant system in state-space form, see equation 2.56. This variational equation transforms into an algebraic Riccatti equation 2.57, which is to be solved with respect to S. Then, the feedback gains vector is found as shown in equation 2.58.

$$\begin{aligned} \dot{x} &= Ax + Bu \\ J(u) &= \int_0^\infty \left(x^T Q\, x + u^T R\, u + 2\, x^T N\, u\right) dt \end{aligned} \tag{2.56}$$

$$A^T S - SA - (SB + N)R^{-1}(B^T S + N^T) + Q = 0 \tag{2.57}$$

$$K = R^{-1}(B^T S + N^T) \tag{2.58}$$

For practical purposes, it is important to remember that matrices Q, R and N are positive-definite and represent the penalties for various cross-products of system's states and the control effort. In practice, the penalties for the cross terms are often not used and set equal to zero. It can be convenient in many cases to have Q as a diagonal matrix of penalties given to each individual state. Thus the higher diagonal element of Q signifies the penalty for a higher system state. For example, an element q_{44} gives a penalty for state x_4. The matrix R represents the penalty for the controller effort which is typically kept small. Matrix N is the cross-penalty of the state and the control effort and is set to zero in the majority of cases.

2.9.3 Luenberger State Observer

In [38], it is also explained that a state observer is nothing but a copy of the plant. State observers are usually implemented digitally on micro-controllers. The idea of having a copy of the plant is that we can force our digital copy to converge to plant's true states by placing another feedback gain L into it. As seen in figure 2.10, two signals are collected from the real plant: the output y and the input u. Given these two, one can duplicate the plant numerically with additional feedback gain L. The feedback L is required to correct any deviation between the real plant output and the predicted output of the copy such that the copy will always tend to converge to the real plant's state.

2.9.4 Kalman State Observer

According to [42], given a continuous plant 2.59, one can construct a state estimate $\hat{x}$ that minimises the state estimation error covariance $P = E\left[(x - \hat{x}) \cdot (x - \hat{x})^T\right]$. Here, u is the known input, w is the white process noise, v is the white measurement noise, that satisfy 2.60. Matrices Q, R, N are named process noise covariance matrix, measurement noise covariance matrix, process-measurement covariance matrix, correspondingly. Then, the optimal solution is the Kalman filter with equations 2.61,

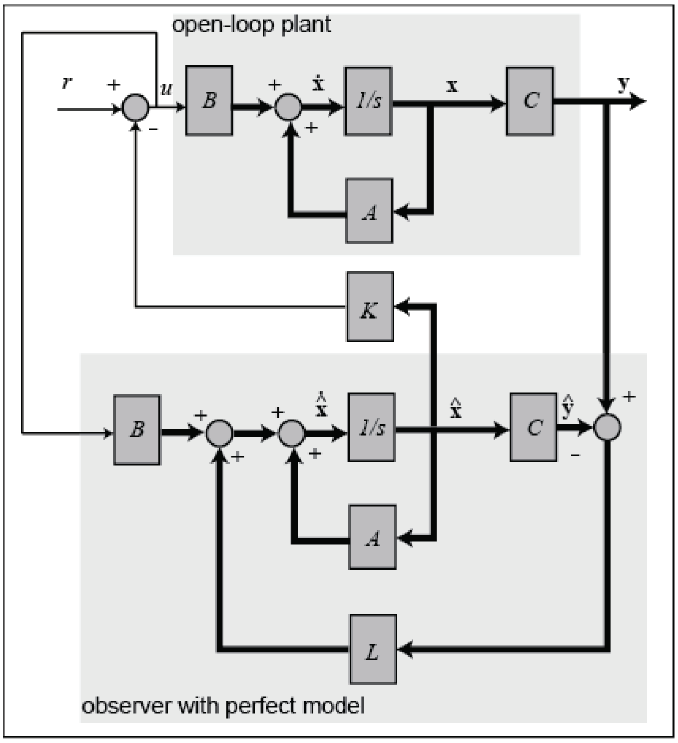

Figure 2.10: Luenberger state observer

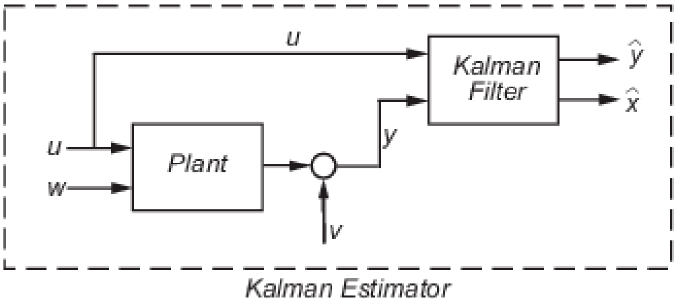

Figure 2.11: Kalman filter as typically connected within a control diagram

where the following conventions are taken: 2.62. Typical usage of Kalman filter is shown on a control diagram in figure 2.11.

$$\begin{aligned} \dot{x} &= Ax + Bu + Gw \\ y &= Cx + Du + Hw + v \end{aligned} \tag{2.59}$$

$$
\begin{aligned}
E\left[w\right] = E\left[v\right] = 0 \\
E\left[w\,w^T\right] = Q \\
E\left[w\,v^T\right] = N \\
E\left[v\,v^T\right] = R
\end{aligned}
\tag{2.60}
$$

$$
\begin{aligned}
L &= \left(P\,C^T + \overline{N}\right) \\
\dot{P} &= A\,P + P\,A^T + \overline{Q} - L\,\overline{R}\,L^T \\
\dot{\hat{x}} &= A\hat{x} + Bu + L\left(y - C\hat{x} - Du\right)
\end{aligned}
\tag{2.61}
$$

$$
\begin{aligned}
\overline{Q} &= G\,Q\,G^T \\
\overline{R} &= R + H\,N + N^T\,H^T + H\,Q\,H^T \\
\overline{N} &= G\left(Q\,H^T + N\right)
\end{aligned}
\tag{2.62}
$$

2.10 Fourier Transform

In our experiments, we used Fourier analysis to process experimental data and measure the frequency response of the mechanical system. As per [43], Fourier analysis is one of the most powerful techniques for temporal data processing. In this section, we review the properties and formulas of the Fourier transform as such and the discrete Fourier transform in particular that was useful to us in our analysis.

2.10.1 Continuous Fourier Transform

In general, Fourier transform is given by 2.63

$$
\hat{f}(\omega) = \frac{1}{\sqrt{2\pi}} \int_{-\infty}^{+\infty} f(t)e^{-i\omega t}dt \tag{2.63}
$$

The meaning of 2.63 is that we examine the function $f(t)$ for incorporating si-

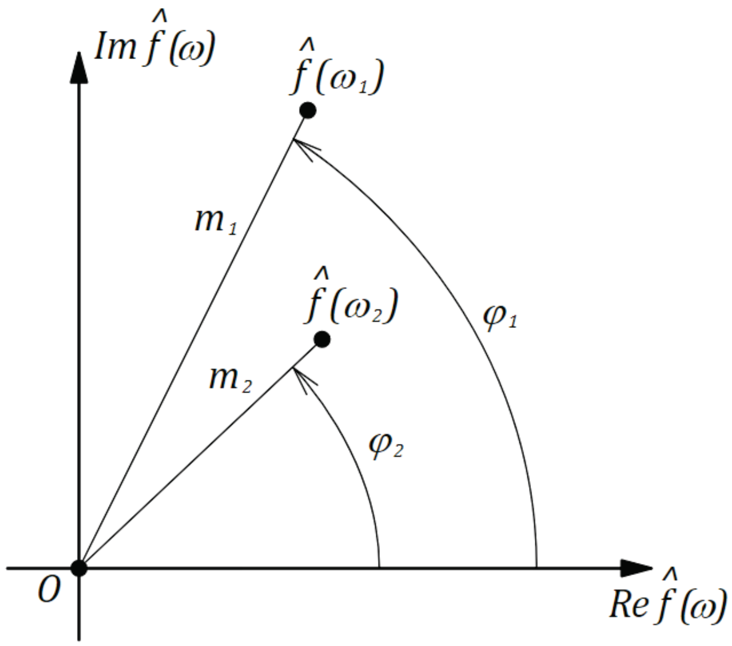

Figure 2.12: Fourier complex amplitudes $\hat{f}(\omega)$ mapped on complex plane for two arbitrary frequencies ω_1 and ω_2

nusoidal contributions of certain frequencies. Thus, the image $\hat{f}(\omega)$ represents the magnitude and phase angle of the corresponding harmonic $f_\omega(t)$. The expressions for magnitude $m(\omega)$, phase $\varphi(\omega)$ and the harmonic $f_\omega(t)$ are given in 2.64. The set of complex amplitudes $\hat{f}(\omega)$ forms a Hermitian symmetric space, i.e. complex pseudo Euclidean infinite dimension space due to the orthogonality of sinusoidal function. Each complex amplitude can be mapped to a complex plane, see figure 2.12.

$$\begin{aligned} m(\omega) &= \left|\hat{f}(\omega)\right|, \qquad \varphi(\omega) = \arg\left(\hat{f}(\omega)\right), \\ f_\omega(t) &= m(\omega)\sin\left(\omega t + \varphi(\omega)\right) \end{aligned} \tag{2.64}$$

2.10.2 Discrete Fourier Transform

In many applications, using discrete Fourier transform [44] turns out to be more practical. Suppose, we measure variable x in time with sampling rate of f_N samples per second. Thus, we have a discrete finite set of measurements $\{x_n\}$, where $n = 0, 1, \dots, N-1$. Then, we can apply discrete Fourier transform 2.65 to analyse frequency properties of $x(t)$.

$$X_k = \sum_{n=0}^{N-1} x_n \exp\left(-i\frac{2\pi k}{N} n\right) \tag{2.65}$$

In 2.65 $k \in [0,\, 1,\, \ldots,\, N-1]$ should be understood as the number of a harmonic and X_k - as the corresponding complex amplitude with its magnitude and phase. As mentioned, N is the length of the sample, and n is the number of discrete time periods passed since the beginning of the measured sequence $\{x_n\}$, that is the time index.

$$f_N = \frac{1}{T} \tag{2.66}$$

$$f_k \le \frac{f_N}{2} \tag{2.67}$$

Let T be the sampling time in seconds. Then, the sampling rate f_N, which is also referred to as Nyquist frequency, is given by 2.66. It should be noted that according to Nyquist sampling theorem [45], only the components having frequency smaller or equal to half of the sampling rate can be resolved 2.67. Therefore, only the first half of discrete spectrum $\{X_k\}$, $k = 0,\, 1,\, \ldots,\, N/2$ carries useful information, whilst the second half being nothing but a mirror image of the first one about the point $k = N/2$, see figure 2.13. One can find the real frequency of k-th harmonic with formula 2.68. The corresponding harmonic of the signal, then, is given by 2.69.

$$f_k = \frac{k}{N} f_N, \qquad \omega_k = 2\pi f_k \tag{2.68}$$

$$x_{\omega_k}(t) = |X_k| \sin\left(\omega_k t + \arg(X_k)\right) \tag{2.69}$$

2.11 Laplace Transform

Laplace transform is widely used in engineering. In this thesis, we used some properties of the transform in our analysis and modelling. Here, we briefly review the

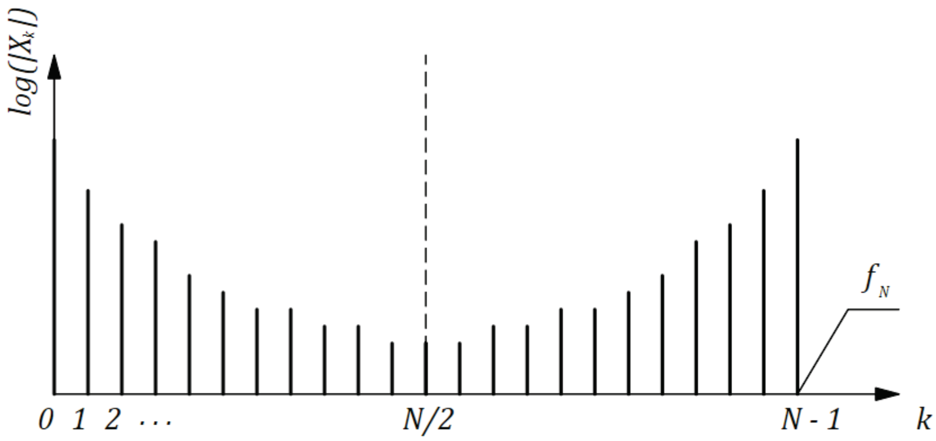

Figure 2.13: Typical discrete Fourier spectrum

fundamentals of Laplace transform and some of its essential features.

Similarly to Fourier transform, Laplace transform does nothing but examines its argument function for containing complex exponentials of all possible frequencies and time factors, see 2.70. Note that Laplace transform converts the argument function $f(t)$ to its complex image $\hat{f}(s)$ and thus it maps functions and variables from time-domain to complex s-domain, see formula 2.71, where $1/\sigma$ is the specific time of the process, ω - is the frequency.

Another remarkable property of Laplace transform is how it acts on a function's derivative, see 2.72. This remarkable property allows one to transform ordinary differential equations to algebraic equations with respect to variable s, that are much easier to analyse and solve in s-domain. Moreover, in many practical cases initial conditions $f(0)$, $f'(0)$, ..., $f^{(n)}(0)$ can be assumed zero. The solution in s-domain usually takes the form of a rational function which can be later converted back to time domain with inverse Laplace transform 2.73 or evaluated with a numerical method, e.g. ODE45.

$$\hat{f}(s) = \mathcal{L}\{f\}(s) = \int_0^\infty e^{-st} f(t)dt \tag{2.70}$$

$$s = \sigma + i\omega \tag{2.71}$$

$$
\begin{aligned}
\mathcal{L}\{f'\} &= s\hat{f}(s) - f(0) \\
\mathcal{L}\{f''\} &= s^2\hat{f}(s) - s\,f'(0) - f(0) \\
\mathcal{L}\{f^{(n)}\} &= s^n\hat{f}(s) - \sum_{k=1}^{n} s^{n-k} f^{(k-1)}(0)
\end{aligned}
\tag{2.72}
$$

$$
f(t) = \mathcal{L}^{-1}\{\hat{f}\}(t) = \frac{1}{2\pi i}\lim_{T\to\infty}\int_{\gamma-iT}^{\gamma+iT} e^{st}\hat{f}(s)ds \tag{2.73}
$$

2.12 Bode Plot Stability Margins

In the experimental part of this research, we often used frequency analysis which is associated with the interpretation of Bode plots. A Bode plot is a plot of two graphs where one graph is the magnitude, and the other is the phase of a complex amplitude, both plotted versus the frequency as illustrated by figure 2.14. Stability margins are the amount of additional gain and phase delay that can be introduced into a closed-loop system without making the system unstable.

2.12.1 Gain Margin

Suppose, we add some gain to the system. Then, it will only affect the top graph from figure 2.14. Namely, it will make the magnitude graph shift up or down by an amount of dB as per the gain chosen. Gain margin is the amount of additional gain required to reach 0 dB level at a frequency where phase turns -180 degrees. In other words, the system is stable as long as at the point of inverse phase gain remains below 0 dB.

2.12.2 Phase Margin

Similarly to the gain, if we add an arbitrary amount of phase delay to the system, then it will only affect the phase graph from figure 2.14. Phase margin is the amount of phase delay that can be added to the system without crossing the level of -180 degrees at a frequency where gain turns 0 dB. In other words, the system is stable as

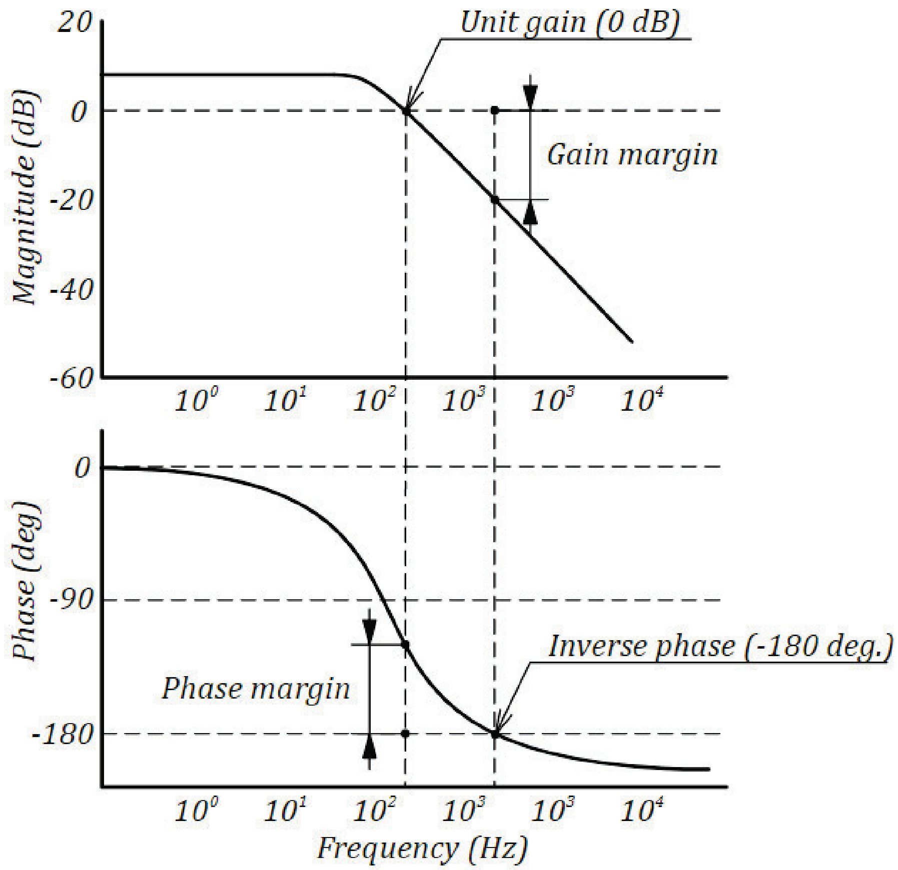

Figure 2.14: Stagility margins

long as the phase delay at the frequency corresponding to 0 dB gain remains greater than -180 degrees.

2.13 Akaike's Final Prediction Error

As per [46], Akaike's final prediction error is used as a measure of goodness of the fitted model to the observation data. In this project, we used Akaike's final prediction error in our identification experiments to get an idea about the validity of the identified models. FPE denotes Akaike's final prediction error in the identification reports generated in Matlab. For readers information, we define Akaike's final prediction error in expression 2.74.

$$FPE = \det\left[\frac{1}{N}\sum_{1}^{N} e(t,\hat{\theta}_N)\left(e(t,\hat{\theta}_N)\right)^T\right]\left(\frac{1+d/N}{1-d/N}\right) \tag{2.74}$$

Here N is the number of values in the estimation data set, $e(t)$ is an $n \times 1$ vector of prediction errors, θ_N represents the estimated parameters, d is the number of estimated parameters.

Chapter 3

Modification of the Existing Setup

3.1 Half-Car Testing Rig

The experimental part of this project was done on a setup which is currently located in UTS building 11 at level B4 in the Dynamics Lab. The setup is named Half-Car Testing Rig and was built in the year 2005 by Laboratory Engineer Christopher Chapman and a PhD student Wade Smith under the supervision of Professor Nong Zhang. The picture of the original setup is taken from Wade Smith's PhD thesis [12] (see figure 3.1). The main elements of the rig are shown on diagram 3.2

As seen in the figure 3.1 and the diagram 3.2, the setup is built upon a massive steel frame serving as a support. The half-car body itself is made of a horizontal frame holding an additional block of mass for the inertia properties. The frame is suspended on two suspension springs located on the left and the right. The hydraulically interconnected suspension system is embedded into the setup. The hydraulic system provides anti-roll functionality also serving as suspension damping. There are two minor frames on the sides that represent the unsprung masses that in a real situation would be the wheels and the tires. The effect of tire stiffness is reproduced by two tire springs of much higher stiffness. Additional mass blocks can be put onto the horizontal frame on the left and on the right to increase the inertia of the system. The bearing in the middle is restricted by the support frame to have only one vertical degree of freedom and can move only in the vertical direction allowing roll inclination as well. Note that suspension springs are omitted from the schematic diagram, although they are present at the real setup. Overall, the system would react to external disturbances such as, for example, lateral force and road inputs, as a real car would react regarding vertical displacements of its elements and the body roll angle.

Figure 3.1: Half-Car Testing Rig designed and built by Wade Smith and Chris Chapman in 2005

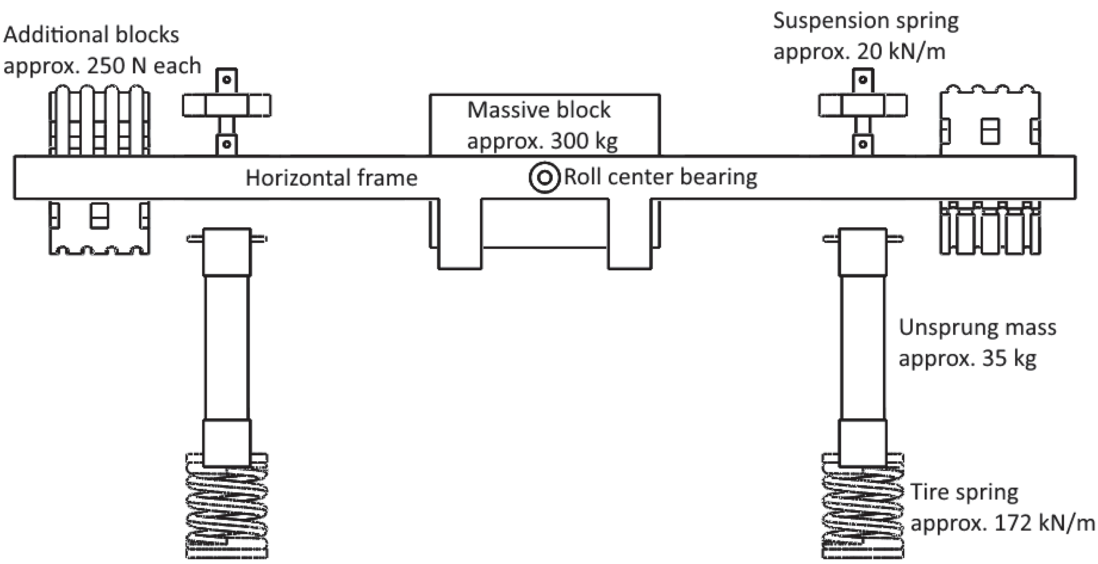

Figure 3.2: Half-Car Testing Rig schematic diagram

3.1.1 Parameters Identification

We started our practical work with identifying as many parameters of the half-car testing rig as possible to the maximum possible precision. It should be mentioned that not all parameters of the setup were well known initially. Therefore we needed to identify the parameters of the setup experimentally. We identified stiffness of springs by direct measurements. Inertia and damping were derived indirectly from experimental data.

Spring Stiffness Identification

In spring stiffness identification experiment we were adding extra load blocks of 250 N each to the frame on the left and the right, and measured spring deflections with linear voltage displacement transducers. In the table of measurements 3.1, are shown the relative displacements of the half-car elements versus the additional load. The data in the table was averaged over multiple repetitions. Thus, we can identify the springs' ratings as a linear regression of the data points obtained.

Table 3.1: Springs identification experiment

Force	Δx_s	Δx_t
N	**mm**	**mm**
0	0.00	0.00
250	13.00	1.25
500	25.75	2.75
750	36.75	4.25
1000	48.75	6.00

In figure 3.3 are shown the graphs of suspension and tire spring stiffness. As the setup has two springs of each type, the data was averaged over the identical springs. We assumed here that minor parameter uncertainties were unimportant to us at least at this stage. With regression analysis applied to the data points collected, we identified suspension springs to have stiffness of $k_s = 20.0 \pm 0.5$ (kN/m) and tire spring stiffness - $k_t = 172.0 \pm 0.5$ (kN/m).

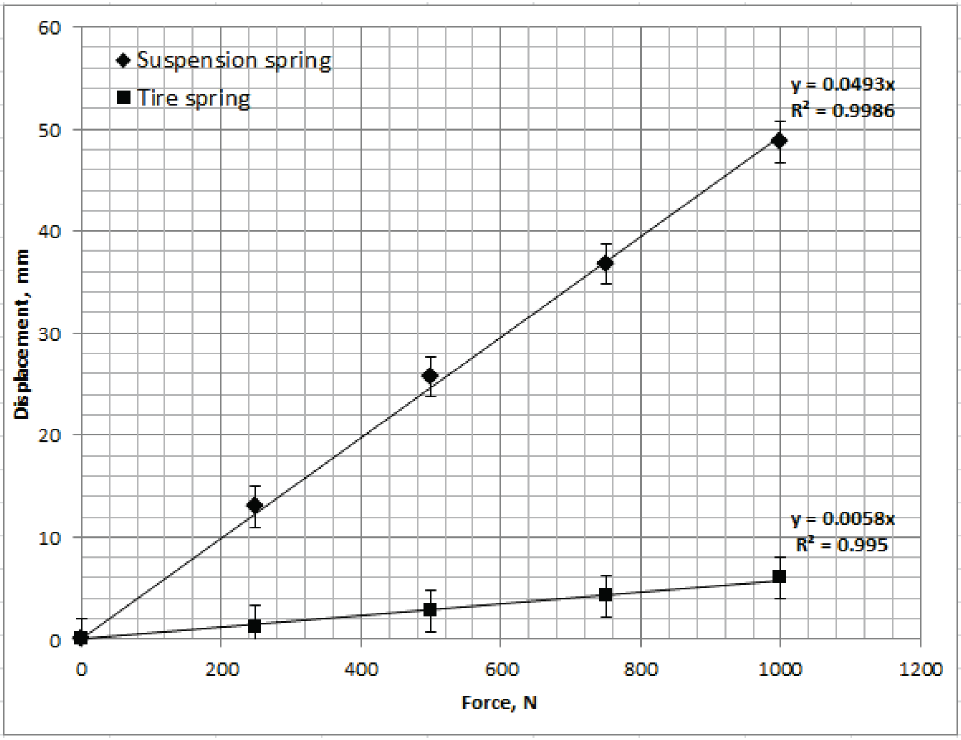

Figure 3.3: Suspension spring and tire stiffness identification

Inertia and Damping Identification

To determine inertia properties and damping properties of the setup we used the knowledge of 2nd order dynamical systems as discussed in section 2.5. To identify inertia properties and damping we conducted two individual experiments, that is free vibration of the car body in vertical direction and free vibration of car body in the roll plane. We found the amplitude values of the vibration responses measured. Given the solution of homogeneous second order differential equation (see equation 3.1) we graphed exponential envelopes for the two modes of vibration that are the bounce and the roll modes. In figures 3.4 are shown the free vibration responses of half-car body to a step input excitation. In figures 3.5 are shown the exponential envelopes graphed in logarithmic scale such that the envelope exponential curve becomes a straight line. The corresponding data can be found in tables 3.2 and 3.3. The identified decay parameters for the bounce mode and the roll mode are $\gamma_{bounce} = 0.507$ s^{-1} and $\gamma_{roll} = 1.823$ s^{-1} respectively. The corresponding vibration angular frequencies are found to be $\omega_{bounce} = 8.726$ rad/s and $\omega roll = 14.411$ rad/s. Now we can also find the natural frequency of oscillation of the setup when no damping is assumed. The natural frequencies turn out to be $\omega_{0\,bounce} = 8.741$ rad/s and $\omega_{0\,roll} = 14.525$ rad/s. This now allows us to find the body mass and body roll inertia as $m_s = 475$ kg and $I_s = 120$ kg.m^2. We can find the equivalent suspension damping coefficient that is produced by the hydraulic system as $c_s = 240$ N/m.s^{-1}.

It should be noted that figure 3.5(a) has three outlier data points that are taken in a red box. The outliers can be explained by the system having some dry friction between its parts which is known not to follow the general law of friction which is usually assumed by default. Unlike the general law when the friction force is assumed proportional to velocity in dry friction the force is constant and therefore it may result in the deviation from exponential decay such as observed in figure 3.5(a). In our analysis, of course, we disregarded the outlier data points as those would have led us to a somewhat distorted result.

To summarise our findings, we made a table of all parameters that were identified in this free vibration experiment (see table 3.4).

$$x(t) = x_0 e^{-\gamma t} \sin \omega t \tag{3.1}$$

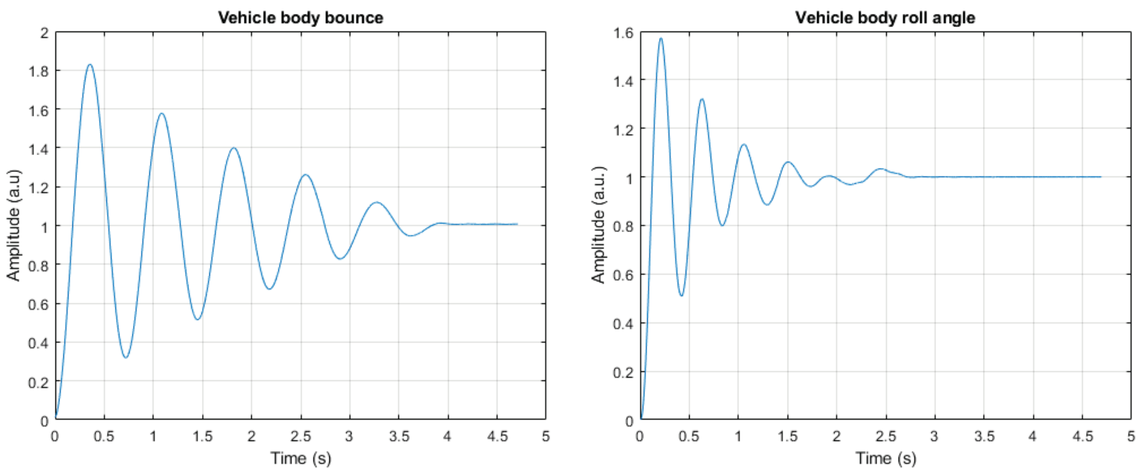

(a) Free bounce vibration (b) Free roll vibration

Figure 3.4: Experimental graphs of half-car responses when subjected to a step input

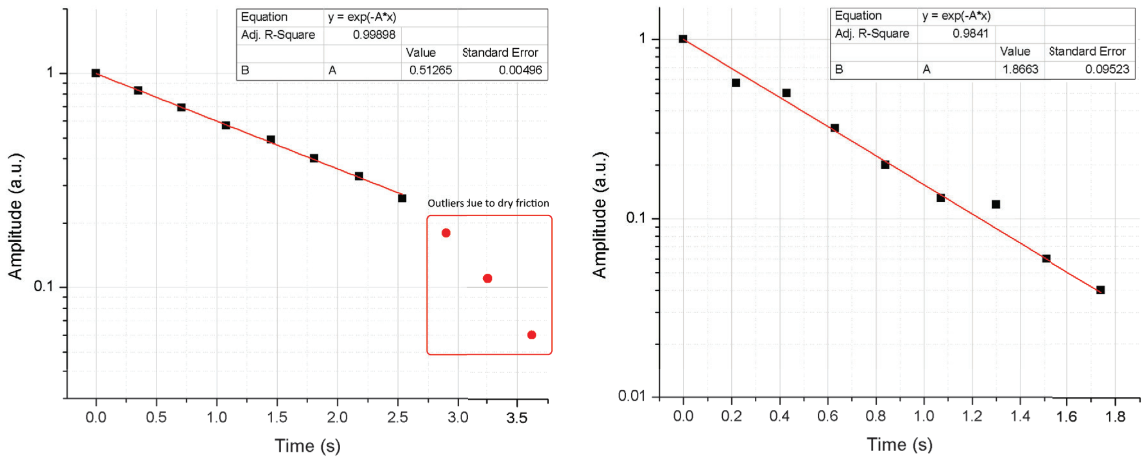

(a) Bounce mode (b) Roll mode

Figure 3.5: Exponential envelopes for the bounce and the roll free vibration modes

Table 3.2: Bounce exponential envelope

Time	**Ampl.**
s	**a.u.**
0.00	1.00
0.35	0.83
0.71	0.69
1.08	0.57
1.45	0.49
1.81	0.40
2.18	0.33
2.54	0.26
2.90	0.18
3.26	0.11
3.62	0.06

Table 3.3: Roll exponential envelope

Time	**Ampl.**
s	**a.u.**
0.00	1.00
0.22	0.57
0.43	0.50
0.63	0.32
0.84	0.20
1.07	0.13
1.30	0.12
1.51	0.06
1.74	0.04

Table 3.4: Half-car rig specifications identified experimentally

Parameter	Notation	Value	Units
Half-car body mass	m_s	475	kg
Half-car body roll inertia	I_s	120	kg.m^2
Unsprung mass	m_u	35	kg
Suspension spring stiffness	k_s	20	kN/m
Tire stiffness	k_t	172	kN/m
Equivalent HIS damping	c_s	240	N/m.s^{-1}

Table 3.5: Active hydraulically interconnected suspension specifications

Parameter	Notation	Value	Units
Accumulator precharge pressure	P_0	250	kPa
Accumulator volume	V_0	0.32	L
Operating pressure	P	14	bar
Upper HIS cylinder area	a_1	5.1×10^{-4}	m^2
Lower HIS cylinder area	a_2	4.1×10^{-4}	m^2
Actuator cylinder area	a_3	1.2×10^{-3}	m^2

3.2 Hydraulic Interconnected Suspension

As for the parameters of the hydraulically interconnected suspension system, many of them are hidden and can not be obtained by direct measurement. Even experimentally, it is hard to measure such parameters as, for instance, the linear loss coefficients. When working on the half-car testing rig, we could choose such parameters as precharge accumulator pressure and working hydraulic pressure. Other parameters were known from our designs and technical documentation. Those are the piston areas. In this section, we made a joint table (see table 3.5) of all known parameters of the active hydraulically interconnected suspension system to the best of our knowledge. The parameters are also explained in figure 3.6.

3.3 Modifications to the Existing Rig

We started our designs by reproducing a 3D model of the existing half-car testing rig as shown in figure 3.7. The uncertainties in the drawing in figure 3.7 are as small as ± 20 mm. The drawings and 3D models are also attached to this thesis as they represent a significant part of our work.

As our experiments imply testing anti-roll capability of active hydraulically inter-

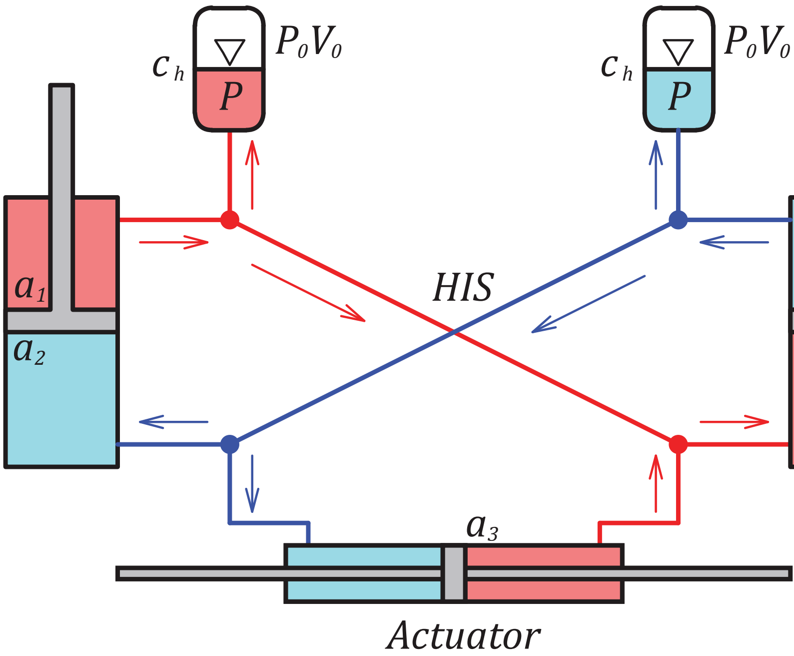

Figure 3.6: Diagram explaining known active hydraulically interconnected suspension system parameters

connected suspension, then we needed to add an external disturbance in the existing setup that would simulate the effect of lateral force emerging from a rapid turning maneuver. To simulate the external lateral force, we proposed to build a roll frame which is to be attached to the main body from the bottom and connected with a hydraulic actuator pushing the attached frame at the bottom against the roll centre bearing. We refer to this actuator as roll actuator further in the text.

We demonstrate the idea of roll actuator on a schematic diagram 3.8. One can see that as the roll actuator is pushing or pulling against the roll centre bearing, the car body will incline in the roll plane. It should be noted that the actuator is driven hydraulically and has a control unit allowing us to deliver an arbitrary force acting on the roll frame.

3.3.1 Attached Roll Frame

We designed a frame (see figure 3.9(a)) which is taking the lateral load from the roll actuator. The frame is attached to the bottom of the half-car horizontal frame which represents the car body. The frame was then built in metal at the UTS FEIT

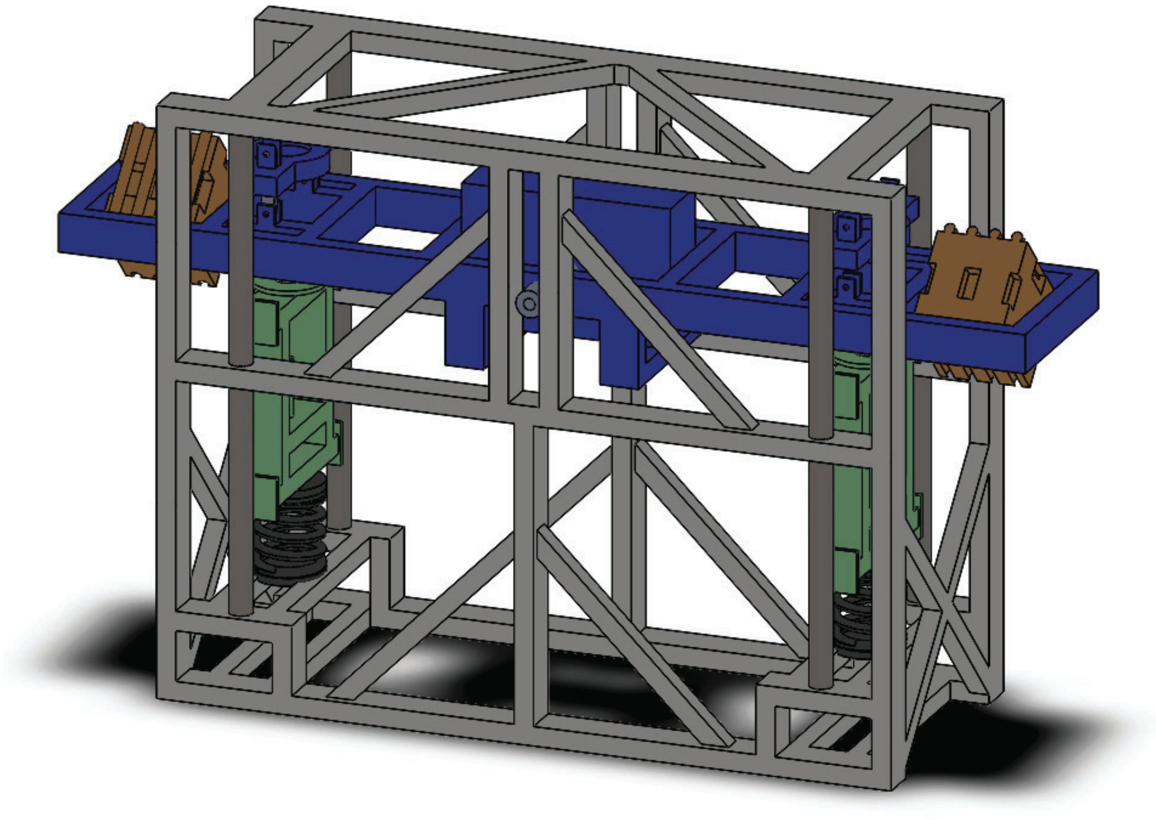

Figure 3.7: 3D CAD model of the original half-car testing rig

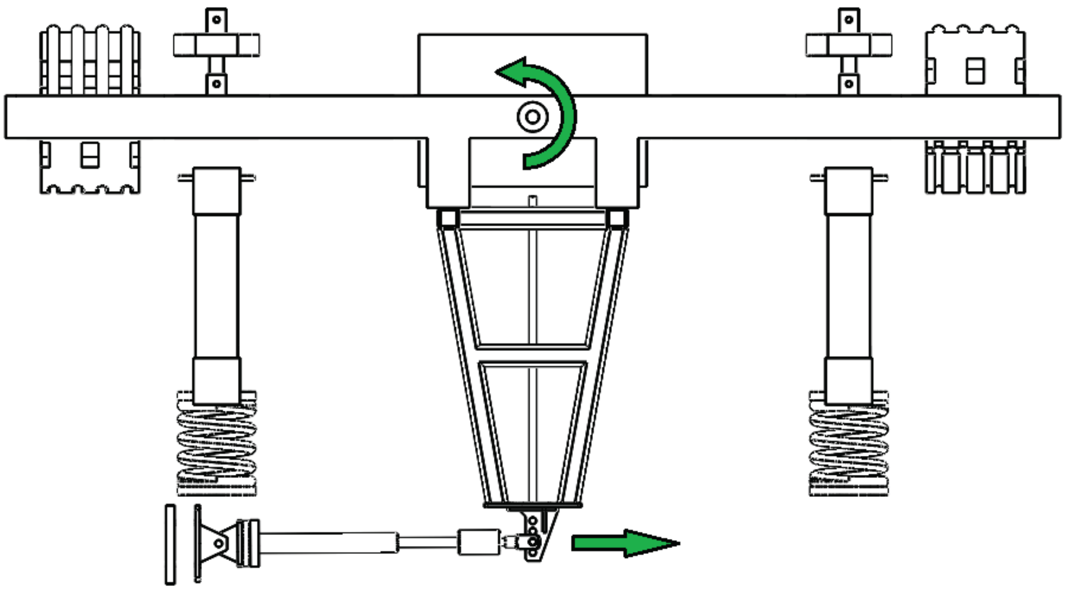

Figure 3.8: Schematic diagram showing how roll moment is translated from the actuator to the half-car body

workshop according to the drawings provided. The body of the frame is welded of 50×50 mm steel channel. In figure 3.9(b) is shown the photo of the real roll frame as it was received from the FEIT workshop. The frame is designed to take loads as high as 10 kN by order of magnitude.

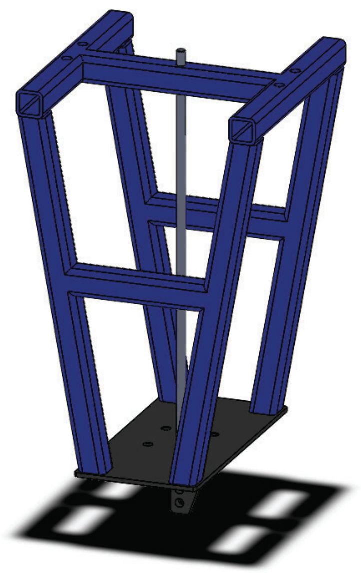

(a) Designed

(b) Manufactured

Figure 3.9: The frame serving to pass the force moment from the roll actuator to the half-car body

3.3.2 Roll Actuator

We, then, designed the roll actuator to push and pull the roll frame against the roll-centre bearing. In figure 3.10(a) is shown the 3D computer-aided graphical design and in figure 3.10(b) is shown a photo of actuator assembly with its mount brackets. The brackets separately are shown in figure 3.11. The actuator installed in place at the half-car rig is shown in figure 3.10(c).

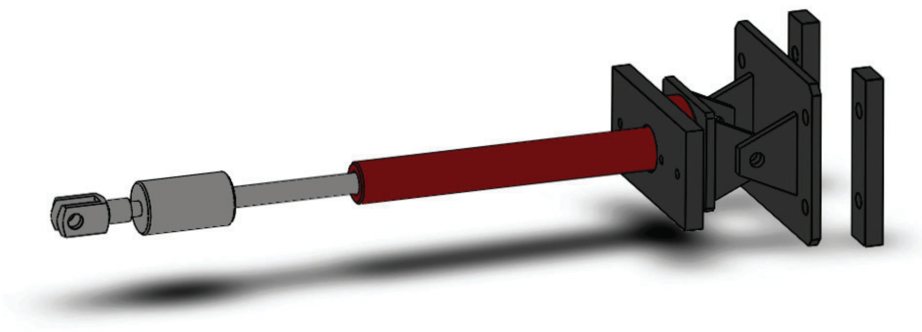

(a) Designed

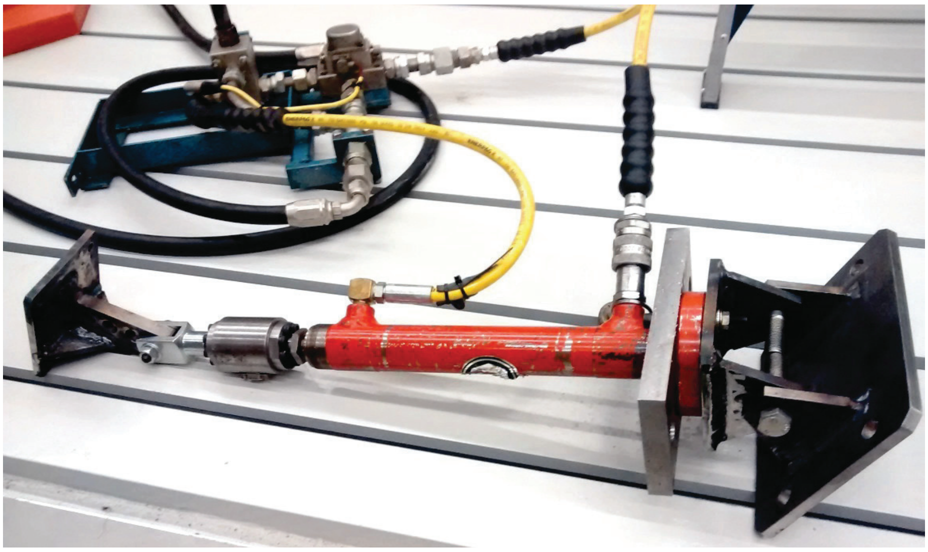

(b) Manufactured

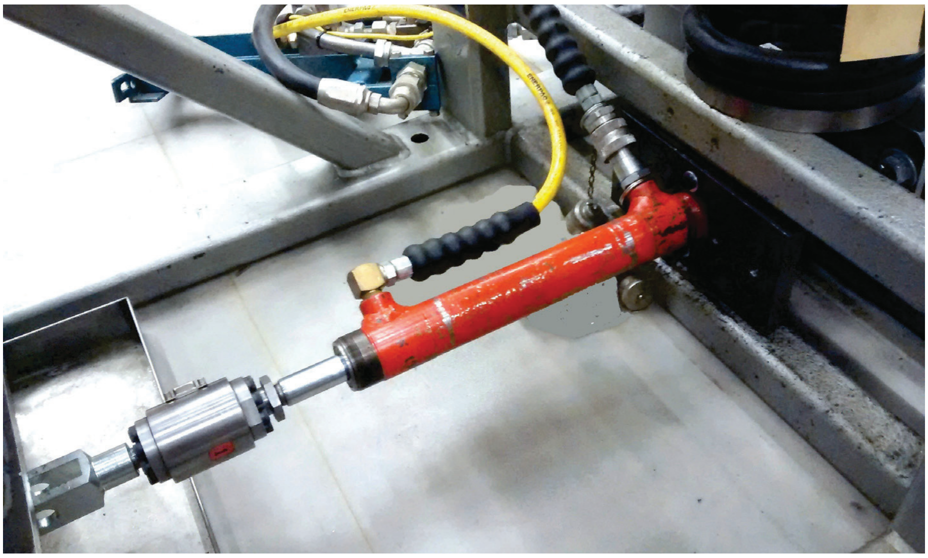

(c) Installed

Figure 3.10: Roll actuator assembly

3.3.3 Modified Half-Car Rig

After all modifications the half-car rig is capable of simulating roll moment applied to the car body as an external disturbance. The modified half-car testing rig is shown in figure 3.12. The 3D CAD drawing 3.12(a) and the photo 3.12(b) give reader the evidence of work that we had done.

3.4 Active HIS Actuator

To have an ability to control the half-car roll angle from the suspension side, we designed and built an actuator for the hydraulically interconnected suspension system. As shown in figure 3.6 a dual-acting double-rod cylinder represents the actuator. As the cylinder moves, the hydraulic fluid flows from one side to another creating pressure difference between the two sides of the hydraulic circuit. The differential pressure is then converted into an additional anti-roll force exerted by the hydraulically interconnected suspension on the car body.

In reality, we approached the design of such actuator taking into account the cost of a dual-acting double-rod custom hydraulic cylinder. Since such part is a quite rare mechanical component, the cost of it in the market varies in the approximate range between \$3000 and \$7000. Therefore, in our designs, we decided to combine two standard cheap cylinders offered by an Australian agriculture machinery manufacturer named Catford Engineering at an affordable price of only around \$200 per piece. The quality of the cylinders is satisfactory, and after more than two years usage the cylinders remain in good condition.

Another expensive component of the design is the servomotor with its control unit. These hardware pieces were borrowed from a different project of UTS which was discontinued long time ago. Thus, the estimated cost of the assembled design is only around \$600.

3.4.1 Rough Calculation

Before we begin to design the actuator for active hydraulically interconnected suspension, it seems important to us to make a preliminary rough estimation of such key parameters as differential pressure and actuator axial force. This calculation will then give us an approximate idea of the loads experienced by the system and conditions at which the actuator will work. When doing the estimation, we assume the hydraulically interconnected system parameters to be equal to those listed in table 3.5. Additionally, we need to assume the half-car parameters equal to those in table 3.4. In this calculation we consider a half-car subjected to the lateral acceleration of as much as $a_l = 1g$ by order of magnitude.

Let us first find the lateral force exerted on the vehicle body due to a rapid turning maneuver. From second Newton's law we find that $F_l = m_s a_l = 4.6$ kN. The lateral force will result in the roll moment of as much as $M = F_l * h = 2.3$ kN.m which is also applied to the vehicle body. Equivalently, this roll moment will be distributed over the car suspension which is to generate an opposing force F_s creating an opposing roll moment of presumably same magnitude. Then we can write $M = F_s\,2b$ or $F_s = M/2b = 1.4$ kN. Then force is, of course, generated by all suspension elements, but for now, as we are only looking for orders of magnitude, we may disregard the suspension springs and dampers and assume that all the force comes from the hydraulically interconnected suspension. Under such an assumption the differential pressure induced in the hydraulic system will be as high as $\Delta P = F_s/a_3 = 12$ bar.

Thus we obtained two critical parameters to be accounted for in our designs. Those are the suspension force $F_s \approx 1.4$ kN which by value is equal to the axial force required to move the actuator, and the differential pressure $\Delta P \approx 12$ bar which can be useful to us when designing the actuator as well as in modelling and simulations.

3.4.2 Actuator Design

The design of this actuator includes some third-party components such as the servomotor, the cylinders, the ball-screw actuator. Therefore, we first modelled all these components in 3D CAD software named SolidWorks. Then we designed the assembly and some custom parts that were somewhat complicated from the CAD and manufacturing perspective. Custom parts were later manufactured in the FEIT Workshop using CNC machinery. The final assembly was built in FEIT Workshop too.

Two custom parts were designed for the actuator. One is the linkage arm between the ball screw and the hydraulic cylinders which connect the rod of a cylinder to the ball screw actuator as shown in figure 3.13. The other part is the coupling for the motor which couples the motor to the ball screw shaft as shown in figure 3.14. The final assembly is shown in figure 3.15.

The author would like to give credit and say thanks to the head of the Workshop Laurence Stonard for valuable discussions on the designs and making things and his willingness to help and collaborate. The author is thankful to the CNC machine operator Siegfried Holler who manufactured all custom parts and assemblies with high professionalism and responsibility in addressing specific needs of the project. The author wants to say special thanks to the Dynamics Lab Engineer Christopher Chapman who was consistently helping in so many different ways from carrying heavy parts and to giving professional and competent pieces of advice when critical decisions needed to be made.

3.4.3 Specifications

It may be useful to other PhD students who will probably use this setup in future to have technical information available. Here we made two tables with the information that is known about the active HIS actuator setup. The bill of materials for the active HIS actuator assembly is given below in table 3.6. The specifications of the active HIS actuator are listed in table 3.7.

Table 3.6: Bill of materials for active HIS actuator

#	**Part**	**Manufacturer**	**P/N**	**Qty**
1	Steel channel base	unknown	unknown	1
2	Hydraulic cylinder	Catford Engineering	CR28	2
3	Ball screw	Machifit	SFU1605-400	1
4	Loaded ball screw support	Machifit	BK12	1
5	Free ball screw support	Machifit	BF12	1
6	Hydraulic adaptor	Ryco	S101-0912	4
7	Servomotor	Baldor	BSM-80A-275-BA	1
8	Motor coupling	UTS Workshop	Custom design	1
9	Ball screw linkage	UTS Workshop	Custom design	2
10	Motor mount bracket	UTS Workshop	Custom design	1

Table 3.7: Active HIS actuator consolidated specifications

Parameter	**Value**	**Units**
Cylinder bore diameter	2	inch
Cylinder shaft diameter	1.25	inch
Cylinder annular area	1.2×10^{-3}	m^2
Cylinder bore cross-section area	2.0×10^{-3}	m^2
Cylinder rated working pressure	3000	PSI
Cylinder max extension force	3.5 4.2	tonnes @ 2500 PSI tonnes @ 3000 PSI
Cylinder max retraction force	2.2	tonnes @ 2500 PSI
Actuator stroke	±150	mm (approx.)
Ball screw pitch	5	mm/rev
Ball screw rated dynamic load	630	kg
Ball screw rated static load	1260	kgf
Motor continuous stall torque	3.20	N.m
Motor peak stall torque	11.86	N.m
Motor rated torque	3.19 3.13	N.m @ 2000 RPM N.m @ 4000 RPM
Motor max speed	7000	RPM

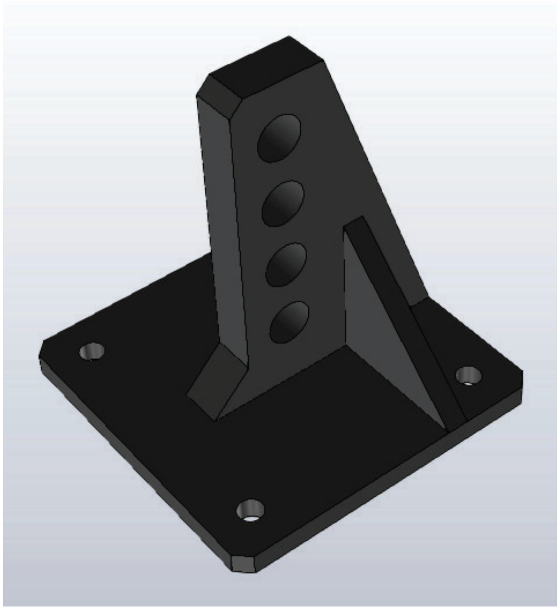

(a) Designed

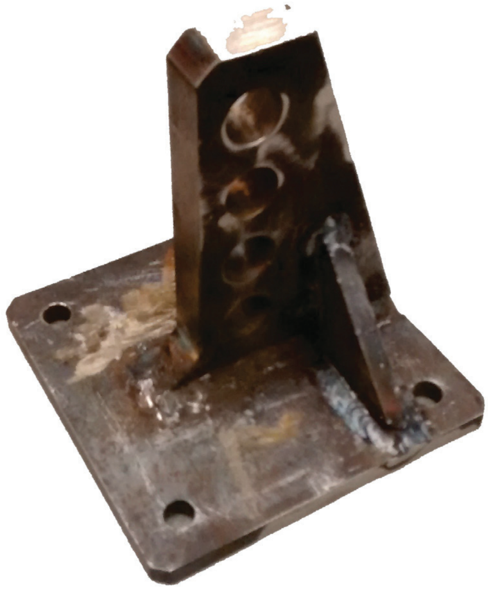

(b) Manufactured

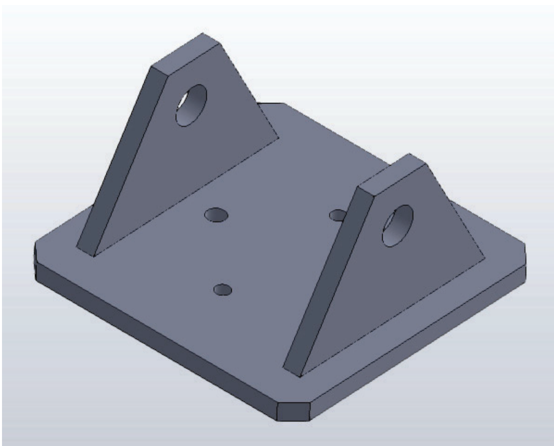

(c) Designed

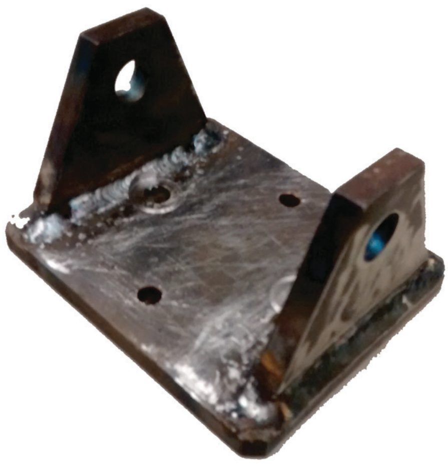

(d) Manufactured

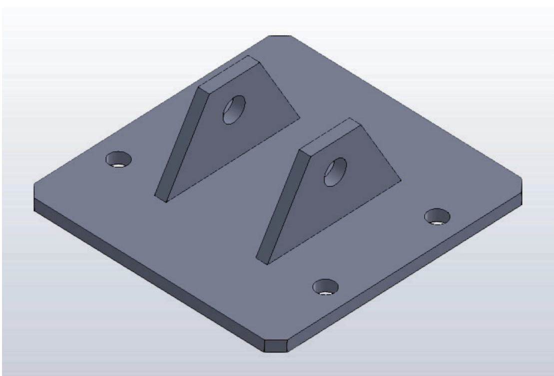

(e) Designed

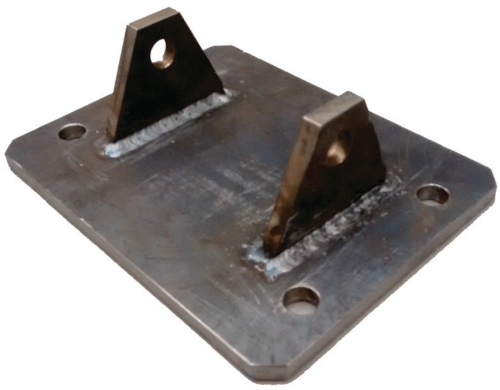

(f) Manufactured

Figure 3.11: Roll actuator mount brackets

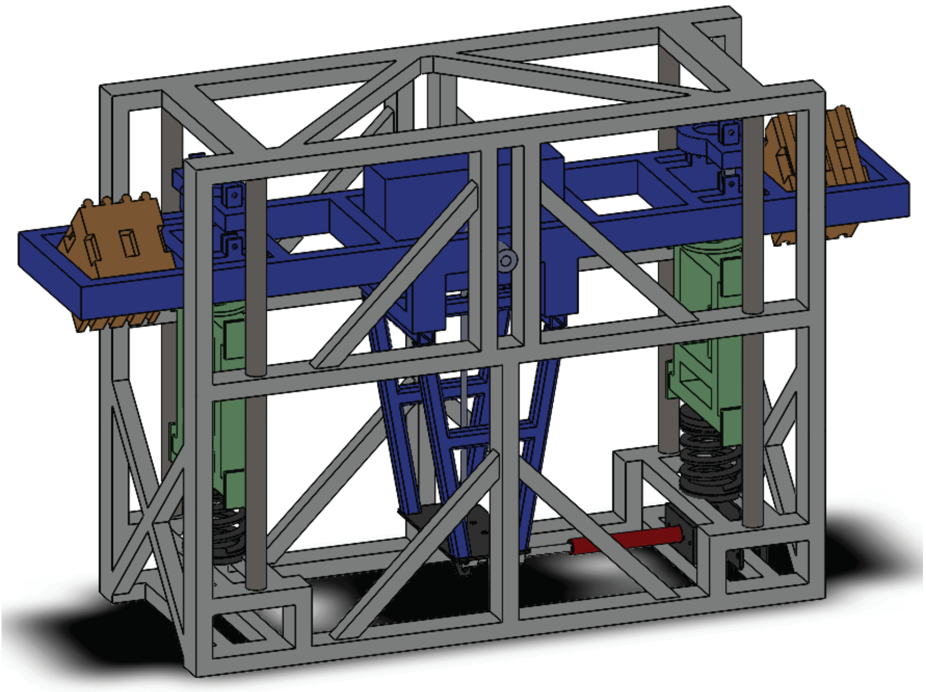

(a) Design

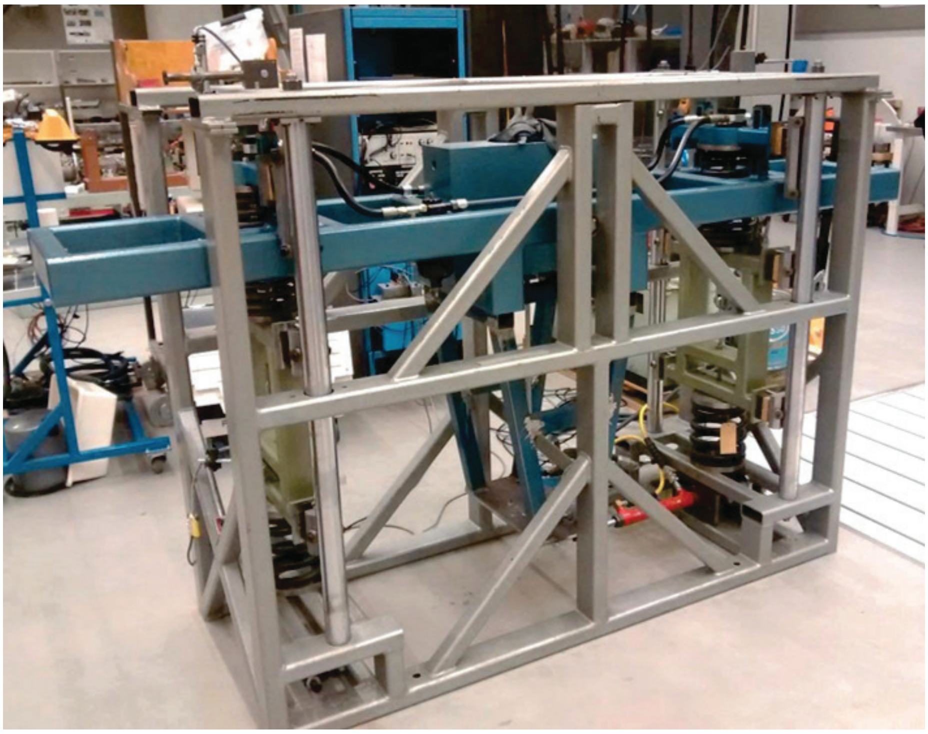

(b) Photo

Figure 3.12: Half-car testing rig after modification

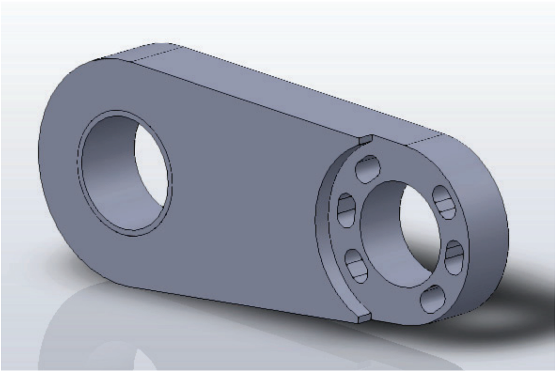

(a) Designed

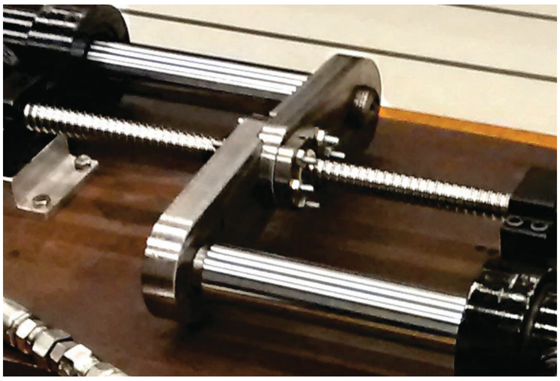

(b) Manufactured

Figure 3.13: Linkage for active HIS actuator

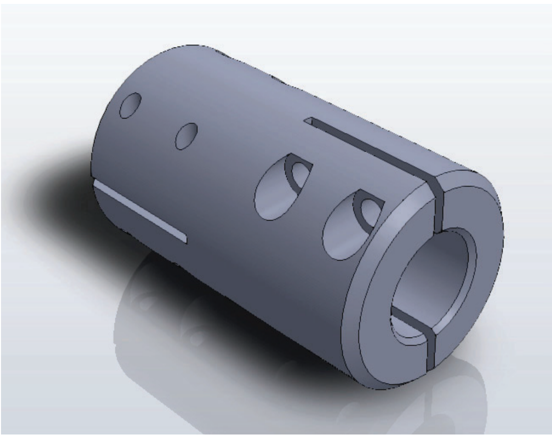

(a) Designed

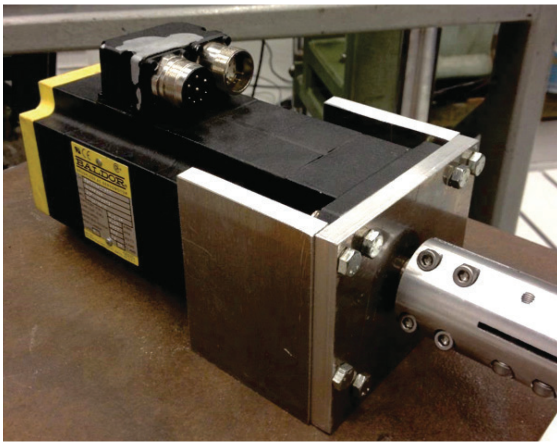

(b) Manufactured

Figure 3.14: Motor coupling

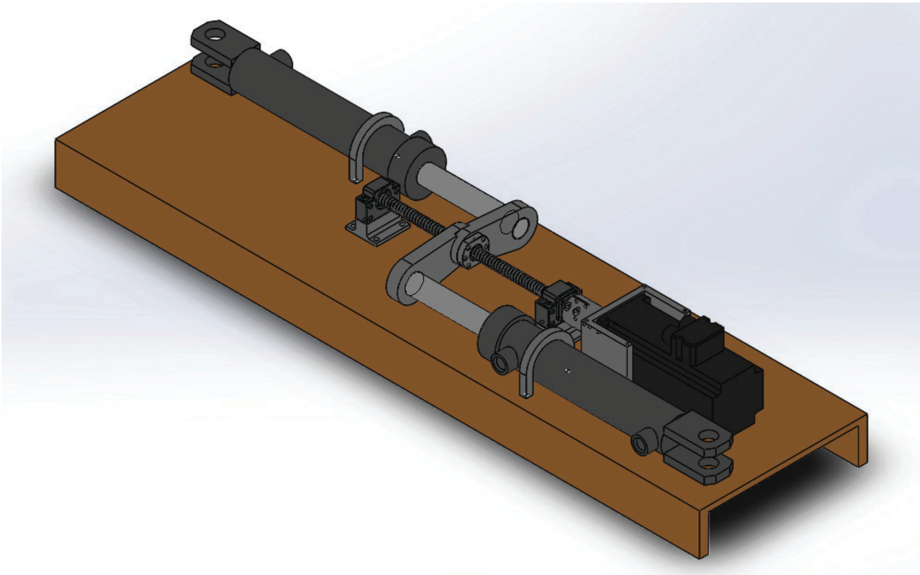

(a) Designed

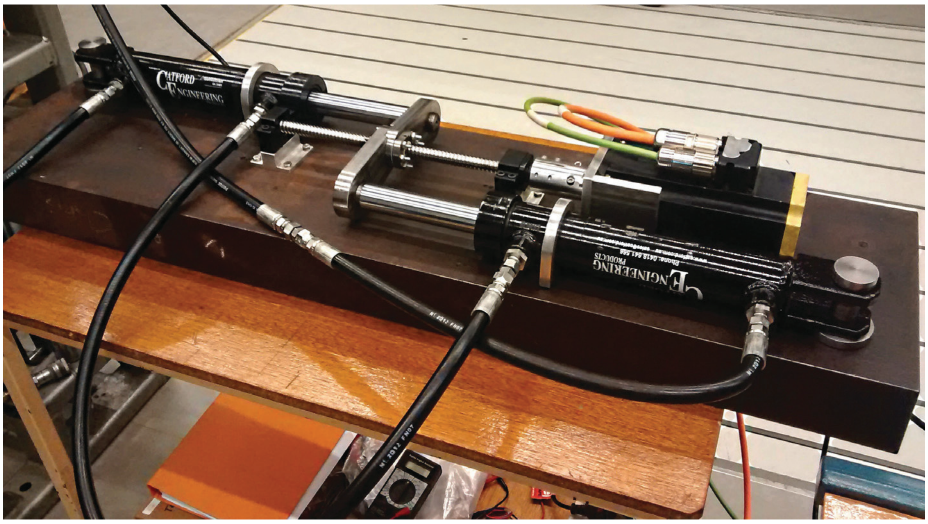

(b) Assembled

Figure 3.15: Active HIS actuator

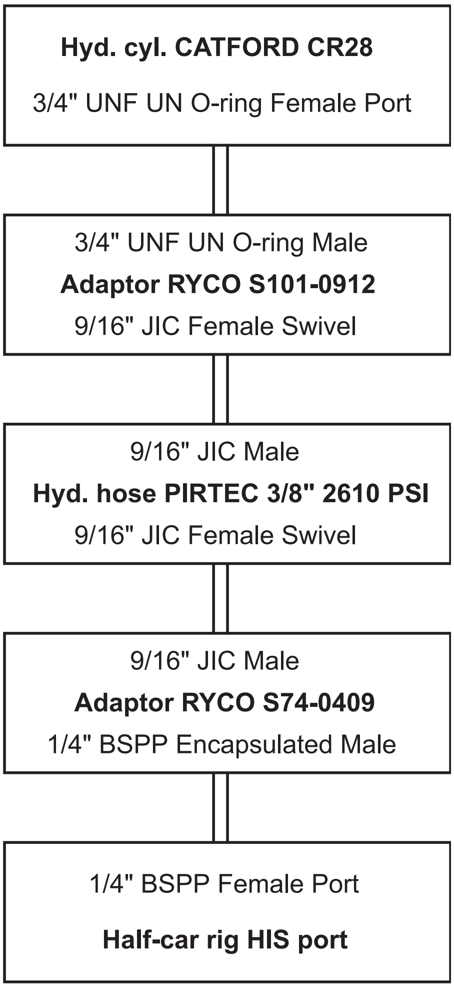

Figure 3.16: Hydraulic connections flow diagram of the active HIS actuator

Chapter 4

Modelling

In this chapter, we obtain the half-car model with active HIS system embedded. The half-car equations of motion are obtained by applying the Lagrange method for systems with non-conservative forces to the mechanical model as described in 2.1. The active HIS system model is obtained by applying the Kirchhoff's laws discussed in section 2.4.5 to the hydraulic circuit. The above two subsystems connect with each other via the hydraulic-to-mechanical boundary condition.

4.1 Augmented Half-Car Model

In this section, we derive an augmented half-car model (see figure 4.1) which has a few amendments compared to the conventional one. Along with two standard road disturbance inputs (u_1, u_2) the augmented model takes three other inputs: $f = (f_1, f_2, f_r)^T$, where f_1 and f_2 are the additional suspension forces and f_r is the equivalent roll force which originates from the centrifugal force $f_c = m_s a_l$ exerted on the car body due to a turning manoeuvre. Both models: conventional and augmented will be used in our research.

In figure 4.1 the half-car model with embedded active HIS system is shown. The massive block represents the car body having the mass m_s (subscript "s" stands for "sprung") and inertia moment about the roll axis I_s. The two smaller blocks represent the unsprung masses of the wheels m_u. The car body is suspended on the wheels through suspension springs and dampers, k_s and c_s being the spring stiffness and the damping coefficient of a damper correspondingly. Tire stiffness is modelled by coefficient k_t. Tire damping is modelled by c_t. Also, we introduce wheel track width as $2b$. Table 4.1 summarises the parameters of the half-car model.

Note that according to Huygens-Steiner theorem the moment of inertia about the roll axis of the vehicle is found as $I_s = I_{xx} + m_s d^2$, where I_{xx} being the intrinsic vehicle body roll moment of inertia and d - the distance between the roll centre and the centre of gravity of the vehicle. For the statement of the theorem, refer to section 2.2.

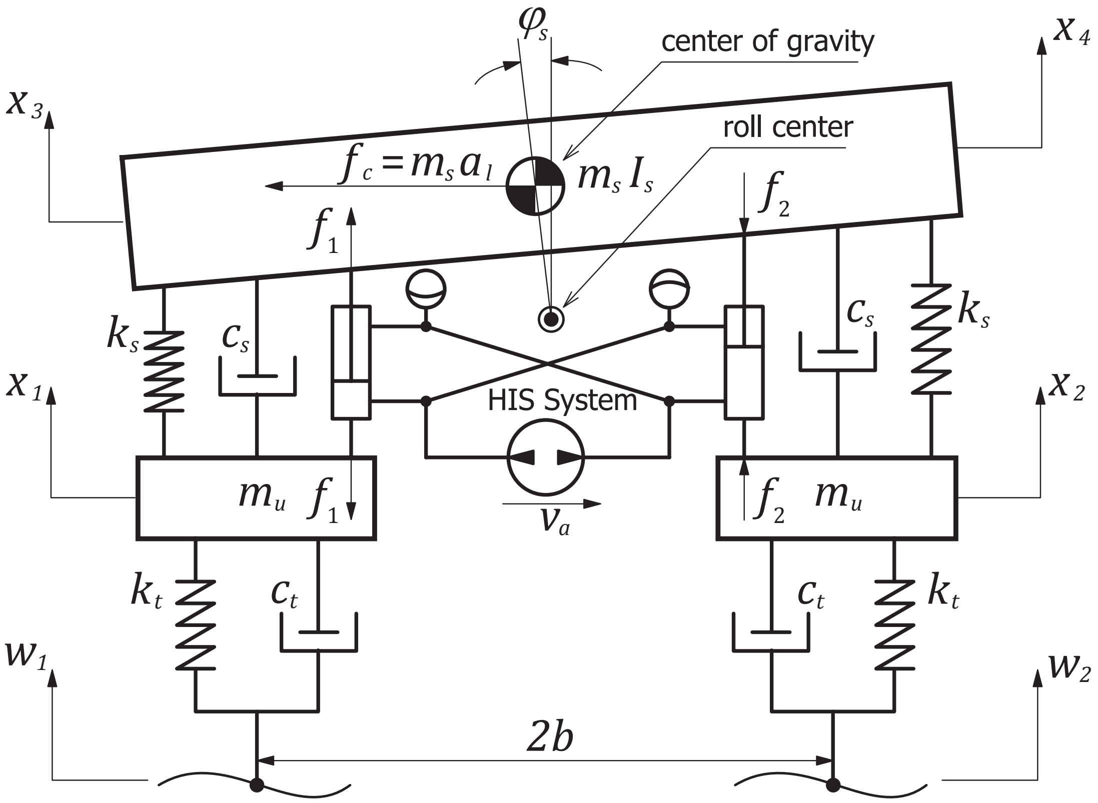

Figure 4.1: Half-car model with active HIS

The variables of the model can be divided into three groups: state variables, inputs and outputs. Let us briefly address each group. State variables are those that describe the inner state of the model. The choice of state variables can be made differently. In this model, the state variable is chosen to be a vector of four displacements that uniquely define the position of the vehicle and all its inertia elements. The inputs of the model are three disturbances: left road input, right road input, lateral acceleration and two additional suspension forces to account for the HIS system. The outputs are two unsprung mass displacements, vehicle body bounce and vehicle body roll angle. The model variables are summarised in table 4.2.

Table 4.1: Augmented half-car model parameters

Parameter	**Symbol**	**Unit**
Vehicle body mass	m_s	kg
Vehicle body moment of inertia	I_s	kg.m^2
Suspension spring stiffness	k_s	N/m
Tire stiffness	k_t	N/m
Suspension damping	c_s	N/(m.s^{-1})
Tire damping	c_t	N/(m.s^{-1})
Center of gravity height	h	m
Wheel track width	$2\,b$	m

Table 4.2: Augmented half-car model variables

Variable	**Symbol**	**Unit**
State variable: $x = (x_1, x_2, x_3, x_4)^T$		
Left wheel vertical displacement	x_1	m
Right wheel vertical displacement	x_2	m
Vehicle body vertical displacement on the left	x_3	m
Vehicle body vertical displacement on the right	x_4	m
Input variables: $f = (f_1, f_2, f_r)^T$ and $w = (w_1, w_2)^T$		
Left road input disturbance	w_1	m
Right road input disturbance	w_2	m
Lateral acceleration	a_l	m/s^2
Additional suspension force on the left	f_1	N
Additional suspension force on the right	f_2	N
Equivalent roll force due to lateral accel.	f_r	N
Output variable: $y = (x_1, x_2, x_s, \varphi_s)^T$		
Left wheel vertical displacement	x_1	m
Right wheel vertical displacement	x_2	m
Vehicle center of gravity vertical displacement	x_s	m
Vehicle body roll angle	φ_s	rad

Now we can write down the expressions for kinetic energy, potential energy and the Rayleigh dissipation function as it was discussed in section 2.1. The expression for kinetic energy 4.1, Rayleigh dissipation function 4.2 and potential energy of the system 4.3 follow here.

$$\begin{aligned}\mathcal{T} &= \frac{1}{2}m_u\dot{x}_1^2 + \frac{1}{2}m_u\dot{x}_2^2 + \frac{1}{2}m_s\dot{x}_s^2 + \frac{1}{2}I_s\dot{\varphi}_s^2 \\ \mathcal{T} &= \frac{1}{2}m_u\dot{x}_1^2 + \frac{1}{2}m_u\dot{x}_2^2 + \frac{1}{8}m_s(\dot{x}_3 + \dot{x}_4)^2 + \frac{1}{8b^2}I_s(\dot{x}_3 - \dot{x}_4)^2\end{aligned} \tag{4.1}$$

$$\mathcal{D} = \frac{1}{2}c_s(\dot{x}_3 - \dot{x}_1)^2 + \frac{1}{2}c_s(\dot{x}_4 - \dot{x}_2)^2 + \frac{1}{2}c_t(\dot{x}_1 - \dot{w}_1)^2 + \frac{1}{2}c_t(\dot{x}_2 - \dot{w}_2)^2 \tag{4.2}$$

$$\mathcal{U} = \frac{1}{2}k_s(x_3 - x_1)^2 + \frac{1}{2}k_s(x_4 - x_2)^2 + \frac{1}{2}k_t(x_1 - w_1)^2 + \frac{1}{2}k_t(x_2 - w_2)^2 \tag{4.3}$$

We then plug these into Lagrange equation 4.4 to obtain the equations of motion 4.5.

$$\frac{d}{dt}\frac{\partial\mathcal{T}}{\partial\dot{q}_i} + \frac{\partial\mathcal{D}}{\partial\dot{q}_i} + \frac{\partial\mathcal{U}}{\partial q_i} = \mathcal{F}_i \tag{4.4}$$

$$\begin{aligned}m_u\ddot{x}_1 + c_s(\dot{x}_1 - \dot{x}_3) + c_t(\dot{x}_1 - \dot{w}_1) \ + \ k_s(x_1 - x_3) + k_t(x_1 - w_1) &= -f_1 \\ m_u\ddot{x}_2 + c_s(\dot{x}_2 - \dot{x}_4) + c_t(\dot{x}_2 - \dot{w}_2) \ + \ k_s(x_2 - x_4) + k_t(x_2 - w_2) &= -f_2 \\ m_p\ddot{x}_3 + m_n\ddot{x}_4 + c_s(\dot{x}_3 - \dot{x}_1) + k_s(x_3 - x_1) &= f_1 - f_r \\ m_p\ddot{x}_4 + m_n\ddot{x}_3 + c_s(\dot{x}_4 - \dot{x}_2) + k_s(x_4 - x_2) &= f_2 + f_r\end{aligned} \tag{4.5}$$

Here the following conventions took place, see 4.6.

$$\begin{aligned}m_p &= \frac{1}{4}\left(m_s + \frac{I_s}{b^2}\right) \\ m_n &= \frac{1}{4}\left(m_s - \frac{I_s}{b^2}\right) \\ f_r &= f_c\frac{h}{b} = m_s a_l\frac{h}{b}\end{aligned} \tag{4.6}$$

We can now formalise the equations of motion 4.5 into a matrix form 4.7

$$M\ddot{x} + C\dot{x} + Kx = Gf + Hw + J\dot{w} \tag{4.7}$$

Here follow the matrices M, C, K, G, H, J. See corresponding expressions 4.8, 4.9, 4.10, 4.11, 4.12, 4.13.

$$M = \begin{bmatrix} m_u & 0 & 0 & 0 \\ 0 & m_u & 0 & 0 \\ 0 & 0 & m_p & m_n \\ 0 & 0 & m_n & m_p \end{bmatrix} \tag{4.8}$$

$$C = \begin{bmatrix} c_s + c_t & 0 & -c_s & 0 \\ 0 & c_s + c_t & 0 & -c_s \\ -c_s & 0 & c_s & 0 \\ 0 & -c_s & 0 & c_s \end{bmatrix} \tag{4.9}$$

$$K = \begin{bmatrix} k_s + k_t & 0 & -k_s & 0 \\ 0 & k_s + k_t & 0 & -k_s \\ -k_s & 0 & k_s & 0 \\ 0 & -k_s & 0 & k_s \end{bmatrix} \tag{4.10}$$

$$G = \begin{bmatrix} -1 & 0 & 0 \\ 0 & -1 & 0 \\ 1 & 0 & -1 \\ 0 & 1 & 1 \end{bmatrix} \tag{4.11}$$

$$H = \begin{bmatrix} k_t & 0 \\ 0 & k_t \\ 0 & 0 \\ 0 & 0 \end{bmatrix} \tag{4.12}$$

$$J = \begin{bmatrix} c_t & 0 \\ 0 & c_t \\ 0 & 0 \\ 0 & 0 \end{bmatrix} \tag{4.13}$$

For further modelling it is convenient to have two slices of matrix G such that $G = [G_1\, G_2]$ see equation 4.14.

$$G_1 = \begin{bmatrix} -1 & 0 \\ 0 & -1 \\ 1 & 0 \\ 0 & 1 \end{bmatrix} \qquad G_2 = \begin{bmatrix} 0 \\ 0 \\ -1 \\ 1 \end{bmatrix} \tag{4.14}$$

In listing A.1 is given the code initialising the parameters of a half-car model and the matrices mentioned above.

4.2 Conventional Half-Car Model

Given the equations of motion in matrix form 4.7, we can obtain a state-space for a conventional half-car model, see equations 4.15, 4.16, 4.17, 4.18, 4.19. In state-space equations 4.15 the new state variable is constructed from the original one as follows: $x \to (x, \dot{x})^T = (x_1, \ldots, x_8)^T = x$. The equations are written in assumption that $J = 0$ for simplicity sake. The input variable here is $u = (w_1, w_2, f_r)^T$. The variables of conventional half-car model are explicitly explained in table 4.3. In listing A.2 is given the code initialising a conventional half-car model.

$$\begin{aligned} \dot{x} &= \mathcal{A}x + \mathcal{B}u \\ y &= \mathcal{C}x + \mathcal{D} \end{aligned} \tag{4.15}$$

$$\mathcal{A} = \begin{bmatrix} [\,0\,]_{4\times4} & [\,I\,]_{4\times4} \\ -M^{-1}K & -M^{-1}C \end{bmatrix}_{8\times4} \tag{4.16}$$

$$\mathcal{B} = \begin{bmatrix} [\,0\,]_{4\times 3} \\ M^{-1}[H\,G_2] \end{bmatrix}_{8\times 3} \tag{4.17}$$

$$\mathcal{C} = \begin{bmatrix} \begin{bmatrix} 1 & 0 & 0 & 0 \\ 0 & 1 & 0 & 0 \\ 0 & 0 & \frac{1}{2} & \frac{1}{2} \\ 0 & 0 & -\frac{1}{2b} & \frac{1}{2b} \end{bmatrix} & [\,0\,]_{4\times 4} \end{bmatrix}_{4\times 8} \tag{4.18}$$

$$\mathcal{D} = [\,0\,]_{4\times 3} \tag{4.19}$$

Table 4.3: Conventional half-car model variables

Variable	Symbol	Unit
State variable: $x = (x_1, x_2, x_3, x_4, \dot{x}_1, \dot{x}_2, \dot{x}_3, \dot{x}_4)^T$		
Left wheel vertical displacement	x_1	m
Right wheel vertical displacement	x_2	m
Vehicle body vertical displacement on the left	x_3	m
Vehicle body vertical displacement on the right	x_4	m
Input variables: $u = (w_1, w_2, f_r)^T$		
Left road input disturbance	w_1	m
Right road input disturbance	w_2	m
Equivalent roll force due to lateral accel.	f_r	N
Output variable: $y = (x_1, x_2, x_s, \varphi_s)^T$		
Left wheel vertical displacement	x_1	m
Right wheel vertical displacement	x_2	m
Vehicle center of gravity vertical displacement	x_s	m
Vehicle body roll angle	φ_s	rad

4.3 Hydraulically Interconnected Suspension Model

In this section, we derive the equations for active hydraulically interconnected suspension. In figure 4.2 is shown the diagram of the hydraulic circuit. The circuit consists of two suspension cylinders that are connected to the vehicle at the suspension struts. The cylinders are cross-connected for anti-roll action. Thus, the circuit is divided into two parts, each having an accumulator attached. The accumulators

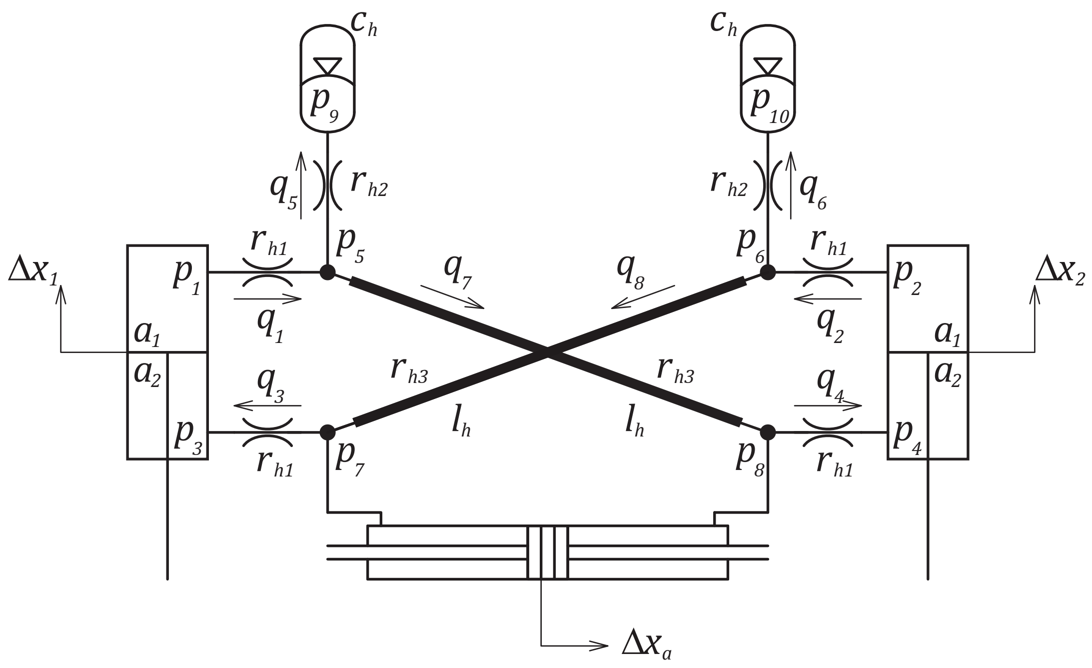

Figure 4.2: Active HIS

act as air springs and accommodate the residual fluid alongside with storing some potential energy of the system. Additionally, the circuit has an actuator which can operate to enhance suspension anti-roll performance. In the model involved the effect of hydraulic losses is accounted for by three linear loss coefficients. These coefficients physically correspond to orifices and long hoses. The effect of fluid inertia is accounted for by the hydraulic inertance coefficient.

4.3.1 Implicit and Hidden Parameters

Here we would like to discuss any implicit or hidden parameters of the model. Firstly it should be mentioned that along with the parameters that can be directly measured, the model contains some parameters that are difficult or almost impossible to obtain by direct measurements.

In the mechanical part of the system, such parameters are moments of inertia and I_{xx} in particular as they can be only derived from system dynamics. For instance, one could measure free vibration responses and derive moments of inertia assuming the system follows 2nd order equations. This method was used precisely in the previous

Table 4.4: Hydraulic circuit parameters

Parameter	Symbol	Unit
Suspension cylinder upper area	a_1	m^2
Suspension cylinder lower area	a_2	m^2
Actuator cylinder annular area	a_3	m^2
Circuit working pressure	P	Pa
Accumulator precharge pressure	P_0	Pa
Accumulator gas specific heat ratio	γ	–
Accumulator volume	V_0	m^3
Acc. gas volume at wrk. pressure	V	m^3
Accumulator capacitance	c_h	m^3/Pa
First linear loss coefficient	r_{h1}	Pa/($m^3.s^{-1}$)
Second linear loss coefficient	r_{h2}	Pa/($m^3.s^{-1}$)
Third linear loss coefficient	r_{h3}	Pa/($m^3.s^{-1}$)
Hydraulic inertance	i_h	Pa/($m^3.s^{-2}$)

Table 4.5: Hydraulic circuit variables

Variable	Symbol	Unit
State variables		
Hydraulic pressure $(p_1, \ldots, p_{10})^T$		Pa
Volumetric hydraulic flow $(q_1, \ldots, q_8)^T$		m^3/s
Input variable $\Delta x = (\Delta x_1, \Delta x_2, \Delta x_a)^T$		
Left suspension deflection	Δx_1	m
Right suspension deflection	Δx_2	m
Actuator displacement	Δx_a	m
Output variable $p = (p_1, p_2, p_3, p_4)^T$		
Pressure in upper chamber of left susp. cyl.	p_1	Pa
Pressure in upper chamber of right susp. cyl.	p_2	Pa
Pressure in lower chamber of left susp. cyl.	p_3	Pa
Pressure in lower chamber of right susp. cyl.	p_4	Pa
Other variables specification (for reference)		
Pressure in left accumulator	p_9	Pa
Pressure in right accumulator	p_{10}	Pa

chapter for mechanical parameters identification.

Another source of model uncertainty originates from hydraulic system linear loss coefficients r_{h1}, r_{h2}, r_{h3}. In our modelling, we only introduce three linear loss coefficients however one can always add more. It should be noted that the linear loss coefficients can only be measured when physically isolated from the rest of the hydraulic circuit. Any attempt to identify the coefficients indirectly meets a fundamental obstacle that three coefficients form an under-defined system of simultaneous equations which cannot be resolved.

4.3.2 Sub-models

Provided suspension deflections are denoted by Δx_1 and Δx_2 and the piston areas - a_1 and a_2, then a cylinder can be modelled with the following set of equations 4.20.

$$\begin{aligned} q_1 &= a_1 \Delta \dot{x}_1, \quad q_2 = a_1 \Delta \dot{x}_2, \\ q_3 &= a_2 \Delta \dot{x}_1, \quad q_4 = a_2 \Delta \dot{x}_2 \end{aligned} \tag{4.20}$$

For simplicity hydraulic capacitor is linearized at a point (P, V), and thus has an approximate capacitance given in 4.21. The accumulator follows the dynamic equations 4.22.

$$c_h \approx \frac{1}{\gamma} \frac{V}{P} \tag{4.21}$$

$$\begin{aligned} p_9 &= \frac{1}{c_h} \int q_5 \, dt, \qquad q_5 = c_h \dot{p}_9 \\ p_{10} &= \frac{1}{c_h} \int q_6 \, dt, \qquad q_6 = c_h \dot{p}_{10} \end{aligned} \tag{4.22}$$

An orifice can be modelled with the Poiseuille's law 4.23, where r_h is the linear loss coefficient and Δp stands for the pressure drop across the orifice. A hose can be modelled with a combination of the Poiseuille's law and the hydraulic inertance law

4.24, where i_h is the hydraulic inertance coefficient.

$$\Delta p = r_h q \tag{4.23}$$

$$\Delta p = r_h q + i_h \dot{q} \tag{4.24}$$

4.3.3 Active HIS Model Derivation

The hydraulically interconnected suspension is modelled with the theory discussed in section 2.4. As per derivation, the resulting model has only the zeros and no poles. This fact agrees with the straightforward nature of the hydraulic equations taking into account that the variable sought is the pressure. However, when the hydraulically interconnected suspension model is later embedded into the half-car mechanical model, it contributes to the mechanical stiffness, damping and inertia matrices which creates a superimposed half-car with active hydraulically interconnected suspension model.

We use Kirchhoff's laws to derive the equations of the model. Equations 4.25 result from applying Kirchhoff's current law to all junctions in the system. Then we apply Kirchhoff's 2nd law to the elements of the system and thus obtain a set of equations 4.26. Additionally, we have four equations for the accumulators, see equation 4.22 and four equations for the cylinders, see equation 4.20. We solve equations 4.25, 4.26, 4.22 and 4.20 simultaneously for pressure and obtain the output vector $p = (p_1, p_2, p_3, p_4)^T$, as expressed through $\Delta x = (\Delta x_1, \Delta x_2, \Delta x_a)^T$, which is required for the calculation of force, see equation 4.27. The expressions for hydraulic matrices of elastance S_h, resistance R_h and inertance I_h are given in 4.28, 4.29, 4.30 correspondingly. In listing

A.3 is given the code initialising an active HIS system.

$$
\begin{aligned}
q_1 &= q_5 + q_7 \\
q_2 &= q_6 + q_8 \\
q_3 &= q_8 - a_3 \Delta \dot{x}_a \\
q_4 &= q_7 + a_3 \Delta \dot{x}_a
\end{aligned}
\tag{4.25}
$$

$$
\begin{aligned}
p_1 - p_5 &= r_{h1} q_1 \\
p_2 - p_6 &= r_{h1} q_2 \\
p_7 - p_3 &= r_{h1} q_3 \\
p_8 - p_4 &= r_{h1} q_4 \\
p_5 - p_9 &= r_{h2} q_5 \\
p_6 - p_{10} &= r_{h2} q_6 \\
p_6 - p_7 &= r_{h3} q_8 + i_h \dot{q}_8 \\
p_5 - p_8 &= r_{h3} q_7 + i_h \dot{q}_7
\end{aligned}
\tag{4.26}
$$

$$
p = S_h \Delta x + R_h \Delta \dot{x} + I_h \Delta \ddot{x} \tag{4.27}
$$

$$
S_h = \frac{1}{c_h} \begin{bmatrix} a_1 & -a_2 & a_3 \\ -a_2 & a_1 & -a_3 \\ -a_2 & a_1 & -a_3 \\ a_1 & -a_2 & a_3 \end{bmatrix} \tag{4.28}
$$

$$R_h = \begin{bmatrix} a_1(r_{h1}+r_{h2}) & -a_2 r_{h2} & a_3 r_{h2} \\ -a_2 r_{h2} & a_1(r_{h1}+r_{h2}) & -a_3 r_{h2} \\ -a_2(r_{h1}+r_{h2}+r_{h3}) & a_1 r_{h2} & -a_3(r_{h2}+r_{h3}) \\ a_1 r_{h2} & -a_2(r_{h1}+r_{h2}+r_{h3}) & a_3(r_{h2}+r_{h3}) \end{bmatrix} \tag{4.29}$$

$$I_h = i_h \begin{bmatrix} 0 & 0 & 0 \\ 0 & 0 & 0 \\ -a_2 & 0 & -a_3 \\ 0 & -a_2 & a_3 \end{bmatrix} \tag{4.30}$$

As we will see later, it is convenient to slice matrices S_h, R_h and I_h in the same manner as we did it with matrix G in 4.14. We keep first two columns in the first slice and third column - in the second, such that equations 4.31 are satisfied.

$$\begin{aligned} S_h &= [S_{h1}\, S_{h2}] \\ R_h &= [R_{h1}\, R_{h2}] \\ I_h &= [I_{h1}\, I_{h2}] \end{aligned} \tag{4.31}$$

4.4 Hydraulic-to-Mechanical Boundary Condition

Now that we have derived the equations for the half-car (4.7) and the HIS system (4.27), we need to write down the hydraulic-to-mechanical boundary conditions to link the two systems with one another.

Hydraulic interconnected suspension has its inputs in the form of suspension deflections, i.e. relative displacements. Therefore we need a matrix to convert from vector $x = (x_1, x_2, x_3, x_4)^T$ of the mechanical model into a vector of relative deflections $\Delta x = (\Delta x_1, \Delta x_2)^T$. This conversion is exactly performed with matrix G_1, which is given in equation 4.14. Equations 4.32 and 4.33 explicitly demonstrate the conversions.

The output of the HIS model is in form of pressure vector $p = (p_1, p_2, p_3, p_4)^T$. Pressures need to be converted into forces $f = (f_1, f_2)^T$ to be fed in the mechanical model as inputs. Thus, we write down another conversion matrix A_h which is the matrix containing piston area values, see equations 4.33. Now we can obtain equivalent mechanical matrices that are super-induced by the HIS system, see equation 4.35. Matrices G_1 and A_h are given in equation 4.34. The resultant matrices from equation 4.35 are explained in table 4.6. In listing A.4 is given the code that implements hydraulic-to-mechanical boundary conditions.

$$\Delta x = G_1^T\, x \tag{4.32}$$

$$f = A_h\, p \tag{4.33}$$

$$\begin{aligned} G_1^T &= \begin{bmatrix} -1 & 0 & 1 & 0 \\ 0 & -1 & 0 & 1 \end{bmatrix} \\ A_h &= \begin{bmatrix} -a_1 & 0 & a_2 & 0 \\ 0 & -a_1 & 0 & a_2 \end{bmatrix} \end{aligned} \tag{4.34}$$

$$\begin{aligned} M_{h1} &= G_1\, A_h\, I_{h1}\, G_1^T \\ C_{h1} &= G_1\, A_h\, R_{h1}\, G_1^T \\ K_{h1} &= G_1\, A_h\, S_{h1}\, G_1^T \\ \\ M_{h2} &= G_1\, A_h\, I_{h2} \\ C_{h2} &= G_1\, A_h\, R_{h2} \\ K_{h2} &= G_1\, A_h\, S_{h2} \end{aligned} \tag{4.35}$$

Table 4.6: Equivalent matrices explained

Matrix	Description
M_{h1}	equivalent mechanical inertia superimposed by HIS
C_{h1}	equivalent mechanical damping superimposed by HIS
K_{h1}	equivalent mechanical stiffness superimposed by HIS
M_{h2}	equivalent inertial reaction to actuator input
C_{h2}	equivalent damped reaction to actuator input
K_{h2}	equivalent stiff reaction to actuator input

4.5 Transfer Function Model Initialisation

In this section, we initialise the transfer function model of the half-car with active hydraulically interconnected suspension. It should be noted that this model, out of all, has a minimum number of assumptions and simplifications. Due to the fluid inertia, this model will have a direct term from input to output. As it is agreed to have tire damping accounted for, this model will also have a more complicated representation and higher order. The hydraulic system is described here with a dynamic model, and therefore it brings another source of complication in the resulting model. Overall the only simplification made in this derivation is the assumption of linear accumulator behaviour which is not the case in the real system. However, such an assumption represents a weaker condition on roll-over stability of a vehicle and thus if we can achieve stability with linear accumulators, then non-linear accumulator will enhance the stability even more.

To derive the transfer-function model we need to write down the expressions for the numerator matrix $N(s)$ and the denominator matrix $D(s)$. If s is the Laplace domain variable, then we can seek for the numerator matrix in the form given in equation 4.36. The expressions for the right side matrices R_0, R_1 and R_2 are given in 4.37. On the other hand, the denominator matrix $D(s)$ is constructed of the mechanical matrices M, C, K and equivalent hydraulic matrices M_{h1}, C_{h1}, K_{h1}, M_{h2}, C_{h2}, K_{h2} from 4.35. For the denominator matrix see equation 4.38. Provided matrices $N(s)$ and $D(s)$ are defined, we can now construct the transfer function matrix $G(s)$ as shown in equation 4.39. For reader's reference we have equation 4.40 which is satisfied for matrix $G(s)$ and the input and output variable vectors u and y respectively. The corresponding equation of motion is given in 4.41. In table 4.7 the input and output variables of the transfer function model are explicitly explained. In listing A.5 is given the code for transfer function initialisation for a half-car with active hydraulically interconnected suspension.

$$N(s) = R_0 + sR_1 + s^2 R_2 \tag{4.36}$$

$$\begin{aligned} R_0 &= [H \quad G_2 \quad K_{h2}] \\ R_1 &= [J \quad [\,0\,]_{4\times 1} \quad C_{h2}] \\ R_2 &= [[\,0\,]_{4\times 3} \quad M_{h2}] \end{aligned} \tag{4.37}$$

$$D(s) = s^2(M - M_{h1}) + s(C - C_{h1}) + (K - K_{h1}) \tag{4.38}$$

$$G(s)_{4\times 4} = D^{-1}(s)\, N(s) \tag{4.39}$$

$$\hat{y}(s) = G(s)\, \hat{u}(s) \tag{4.40}$$

$$(M - M_{h1})\, \ddot{y} + (C - C_{h1})\, \dot{y} + (K - K_{h1})\, y = R_0\, u + R_1\, \dot{u} + R_2\, \ddot{u} \tag{4.41}$$

4.6 State-Space Model

Now we can also derive a state-space for the model involved. In this derivation, we assume the matrices of the right side that multiply the first and the second derivative of the input to be equal to zero: $R_1 = 0$ and $R_2 = 0$. Such an assumption allows us to keep the formalisation relatively human-friendly and straightforward as well as to preserve the physical meaning of the system states. Although the resulting state-

Table 4.7: Transfer function model variables

Variable	**Symbol**	**Unit**
Input variable $u = (u_1, u_2, u_3, u_4)^T$		
Left road input	u_1	m
Right road input	u_2	m
Equivalent roll force	u_3	N
Hydraulic actuator displacement	u_4	m
Output variable $y = (y_1, y_2, y_3, y_4)^T$		
Left wheel vertical displacement	y_1	m
Right wheel vertical displacement	y_2	m
Vehicle body vertical displacement on the left	y_3	m
Vehicle body vertical displacement on the right	y_4	m

space model is derived under these assumptions, it is often more practical to use this very model rather than using a more complicated transfer function model.

We now derive the state-space for half-car with active hydraulically interconnected suspension as it is described in section 2.7 under the assumptions mentioned above. The matrices $\mathcal{A}$, $\mathcal{B}$, $\mathcal{C}$, $\mathcal{D}$ that satisfy the state space equation 4.15 are given in expressions 4.42, 4.43, 4.44, 4.45. The variables of the state-space model are explicitly explained in table 4.8. The code initialising the state-space for the half-car with active hydraulically interconnected suspension is given in listing A.6.

$$\mathcal{A} = \begin{bmatrix} [\,0\,]_{4\times4} & [\,I\,]_{4\times4} \\ -(M - M_{h1})^{-1}(K - K_{h1}) & -(M - M_{h1})^{-1}(C - C_{h1}) \end{bmatrix}_{8\times4} \tag{4.42}$$

$$\mathcal{B} = \begin{bmatrix} [\,0\,]_{4\times4} \\ (M - M_{h1})^{-1}[H\, G_2\, K_{h2}] \end{bmatrix}_{8\times4} \tag{4.43}$$

$$\mathcal{C} = \begin{bmatrix} \begin{bmatrix} -1 & 0 & 1 & 0 \\ 0 & -1 & 0 & 1 \\ 0 & 0 & \frac{1}{2} & \frac{1}{2} \\ 0 & 0 & -\frac{1}{2b} & \frac{1}{2b} \end{bmatrix} & [\,0\,]_{4\times4} \end{bmatrix}_{4\times8} \tag{4.44}$$

Table 4.8: State-space model variables

Variable	Symbol	Unit
State variable: $x = (x_1, x_2, x_3, x_4, \dot{x}_1, \dot{x}_2, \dot{x}_3, \dot{x}_4)^T$		
Left wheel vertical displacement	x_1	m
Right wheel vertical displacement	x_2	m
Vehicle body vertical displacement on the left	x_3	m
Vehicle body vertical displacement on the right	x_4	m
Input variables: $u = (w_1, w_2, f_r, \Delta x_a)^T$		
Left road input disturbance	w_1	m
Right road input disturbance	w_2	m
Equivalent roll force due to lateral accel.	f_r	N
Actuator displacement	Δx_a	m
Output variable: $y = (\Delta x_1, \Delta x_2, x_s, \varphi_s)^T$		
Left suspension deflection	Δx_1	m
Right suspension deflection	Δx_2	m
Vehicle center of gravity vertical displacement	x_s	m
Vehicle body roll angle	φ_s	rad

$$\mathcal{D} = [\,0\,]_{4\times 4} \tag{4.45}$$

4.7 System Order Analysis

Finally, we obtained the model for the half-car with the active hydraulically interconnected suspension which in our codes is stored in a matrix object variable named `SYSSS`. (system state-space). The model is generally of 8-th order and has multiple inputs and multiple outputs. However, practically, the order of the model can be reduced within acceptable tolerance and accuracy bounds. Particularly for control system design are useful the following two terms of the state-space matrix: $\mathtt{SYSSS}_{43}\mathtt{(s)}$ and $\mathtt{SYSSS}_{44}\mathtt{(s)}$ that are originally of 8-th order. Element $\mathtt{SYSSS}_{43}\mathtt{(s)}$ stands for the car body roll angle response to lateral force excitation. Element $\mathtt{SYSSS}_{44}\mathtt{(s)}$ is responsible for the roll angle response to the input from the controlled actuator.

According to [36] Hankel singular values calculated for a model signify model states' contributions to the behaviour of the system. Thus, by checking Hankel singular values, one can examine the impact of every state on the system. This allows one to effectively truncate a model to a reasonable order and simplify further analysis as well as the design of a control system. The respective Hankel singular values for transfer functions `SYSSS`$_{43}$`(s)` and `SYSSS`$_{44}$`(s)` are shown in figure 4.3.

In figure 4.3 one can see that for both systems first two states are dominant, whereas the third and the fourth states' contributions are orders of magnitude smaller. Based on this information we suppose that it is safe to truncate the models down to second order with Matlab command `reduce(SYSSS(4,4),2,'Algorithm','balance')`.

To validate the truncation one can compare the Bode diagrams of the two systems before and after truncation and see how well the reduced and original models match within the range of frequencies of the interest. As discussed in the Introduction to this thesis, the frequency range of interest for us is $f = 0.1 \dots 10$ Hz. In figure 4.4 the Bode diagrams are displayed. We consider the agreement of the models before and after truncation that is seen in the figures as acceptable and satisfactory. The truncated models will be then used in the next chapter for control system design and simulations.

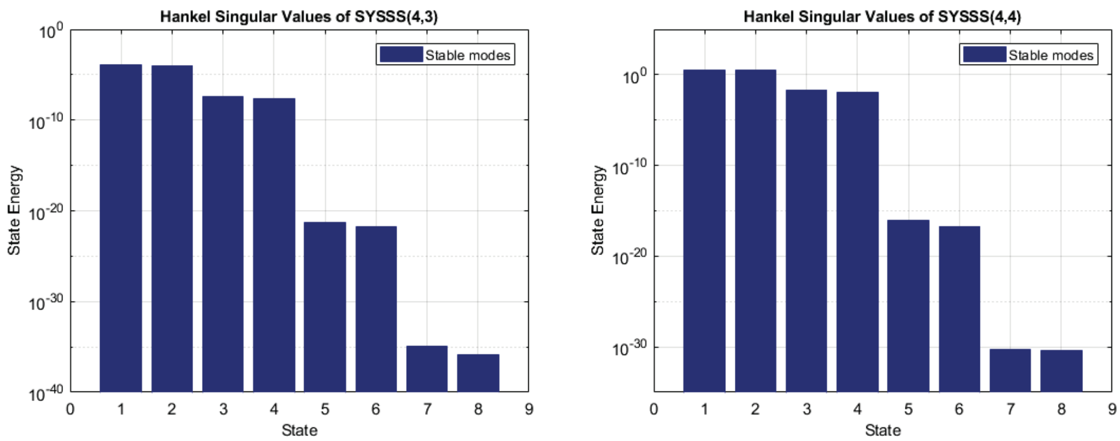

(a) `SYSSS`$_{43}$`(s)`

(b) `SYSSS`$_{44}$`(s)`

Figure 4.3: Hankel singular values

4.8 Control System Design

For control system design we followed the tutorial from [38]. We consider a multi-input-multi-output linear time-invariant system having two inputs and four outputs. The system is constructed of two terms of the transfer function matrix `SYSSS(s)`,

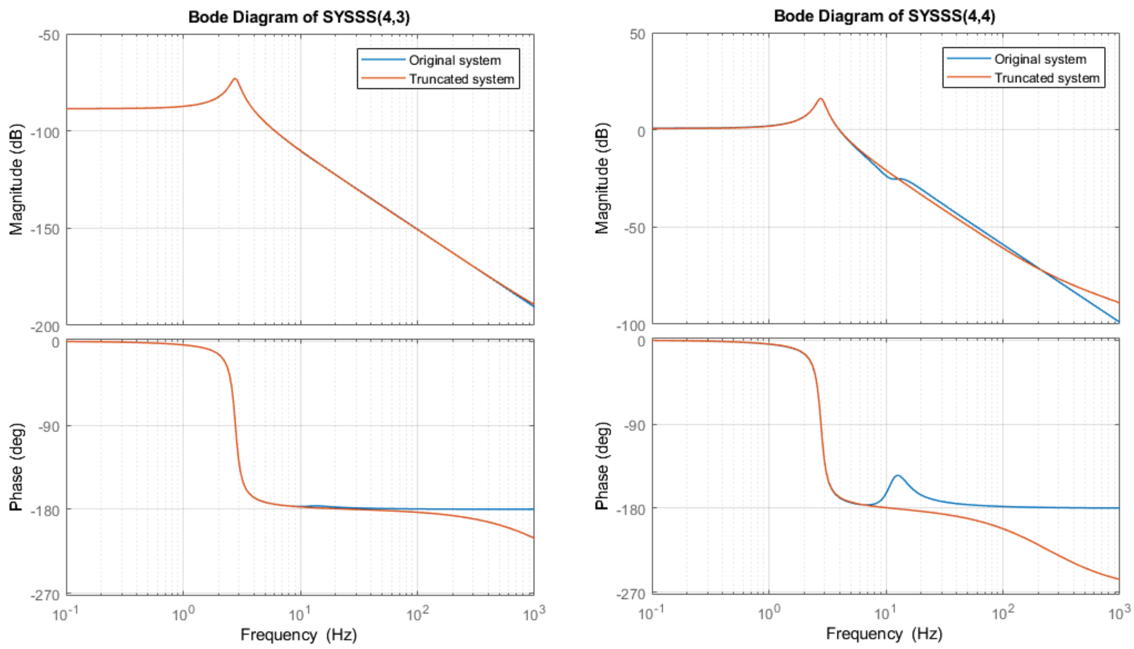

(a) `SYSSS`$_{43}$`(s)` (b) `SYSSS`$_{44}$`(s)`

Figure 4.4: Bode diagrams compared

namely `SYSSS`$_{43}$`(s)` and `SYSSS`$_{44}$`(s)`. As they both belong to the same output which is the roll angle, they share the same denominator whereas the numerator is different. The `SYSSS`$_{43}$`(s)` term is responsible for the disturbance exerted on vehicle body by the lateral force. The `SYSSS`$_{44}$`(s)` term takes account of the anti-roll actuator effort influence on the system.

We, first, truncate the subsystem `SYSSS`$_{44}$`(s)` to the order of two and store the result in a variable `SYSR(s)`. Then we design a linear quadratic regulator to enhance the stability of `SYSR(s)`. The subsystem `SYSR(s)` is initially stable, although near marginal, as the poles of `SYSR(s)` are located relatively close to the imaginary axis in the left half-plane. As seen in figure 4.5, the poles of the original system appear at points $-1.47 \pm 17.5i$ s^{-1}, resulting in an overshoot of 76.8%.

4.8.1 Linear Quadratic Regulator

To stabilise the plant `SYSR(s)` we find the state feedback gains $\mathcal{K}$ as a solution of linear quadratic regulator problem. In Matlab, one can do it easily with the command `K = lqr(SYSR,Q,R,N);`. It is still up to the engineer to choose the penalties. By trial and error, we find the appropriate values of penalties that are given in equation 4.46.

It is common to give higher penalty $q_{22} = 10$ to a higher state x_2 as this should normally result in the reduction of the absolute value of the error. We also assign somewhat smaller penalty $q_{11} = 1$ to the lower state x_1 as it is always a good practice to have compensation for the error rate too. If not critical, we can keep the penalty for the control effort R relatively small. Unless otherwise required, we are safe to keep the cross terms all N equal to zero.

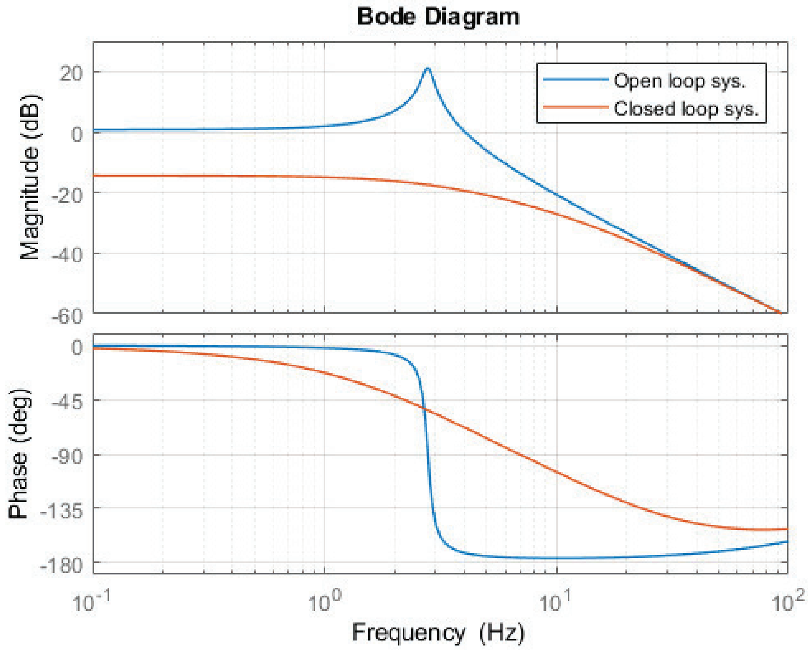

(a) Bode diagram

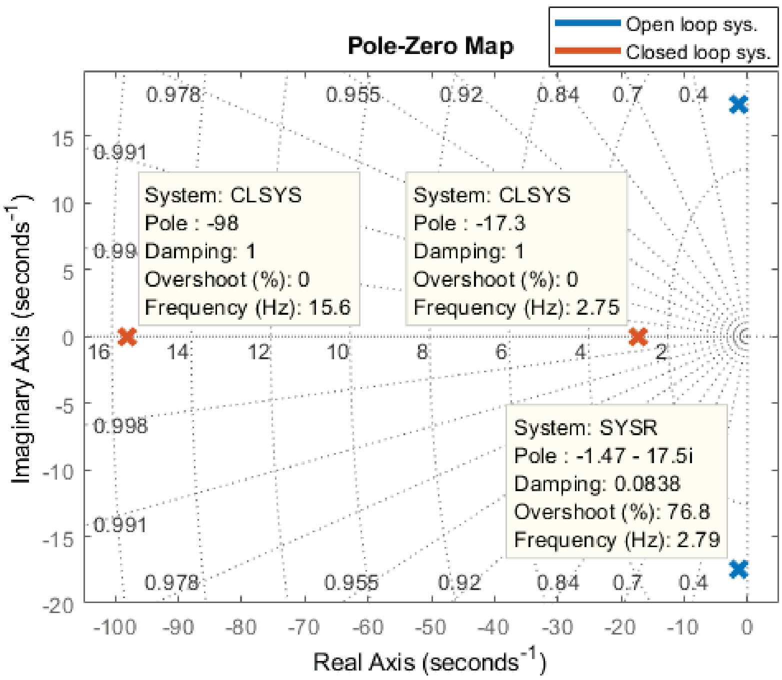

(b) Pole-zero map

Figure 4.5: Open loop model compared with closed loop model

$$Q = \begin{bmatrix} 1 & 0 \\ 0 & 10 \end{bmatrix}$$

$$R = 0.01 \tag{4.46}$$

$$N = \begin{bmatrix} 0 \\ 0 \end{bmatrix}$$

Now that we have the state-feedback gains vector $\mathcal{K}$ we can construct the closed loop model. Provided $\mathcal{A}$, $\mathcal{B}$, $\mathcal{C}$, $\mathcal{D}$ are the state-space matrices of the open loop system, and $\mathcal{A}'$, $\mathcal{B}'$, $\mathcal{C}'$, $\mathcal{D}'$ are the state-space matrices of the closed-loop system, we formalise the closed loop system as shown in equation 4.47. The linear quadratic regulator enhances the closed-loop system stability. In figure 4.5 are shown the poles of the closed-loop system as compared with the poles of the open loop system. One can see that the closed loop system has its poles located along the real axis and farther to the left which results in zero overshoot, no oscillation when subjected to a step input and a much faster settling time. For reference, is given the bode plot which is compared between the two systems.

$$\mathcal{A}' = \mathcal{A} - \mathcal{B}\,\mathcal{K}$$

$$\mathcal{B}' = \mathcal{B}$$

$$\mathcal{C}' = \mathcal{C} \tag{4.47}$$

$$\mathcal{D}' = 0$$

4.8.2 State Observer Design

To apply state-feedback control in practice, one also needs to design a state observer. In our simulations, we are going to use Luenberger state observer as the one which is easy to comprehend. To design the observer means to relocate the poles of a system with state space matrices $\mathcal{A}^T$, $\mathcal{C}^T$. Relocation of poles can be done with Matlab command `L = place(A',C',[-200,-201])';` which returns observer feedback gains vector $\mathcal{L}$. One should remember that the observer must converge faster than the observed model, that is the poles of the observer must be located farther away to the left. As seen from the Matlab command above, our choice of observer poles is $(-200, -201)$ which is perhaps about ten times faster than the observed model. The observer itself can be defined as a state-space model with matrices $\mathcal{A}''$, $\mathcal{B}''$, $\mathcal{C}''$, $\mathcal{D}''$ that are given in equation 4.48. The script implementing the algorithms described in this section are implemented in listing A.7.

$$\begin{aligned}
\mathcal{A}'' &= \mathcal{A} - \mathcal{L}\,\mathcal{C} - \mathcal{B}\,\mathcal{K} \\
\mathcal{B}'' &= \mathcal{L} \\
\mathcal{C}'' &= [\,I\,]_{2\times 2} \\
\mathcal{D}'' &= 0
\end{aligned} \tag{4.48}$$

4.9 Scripts Call Sequence

The final piece of our modelling process is the simulation diagram. We build a simulation diagram in Simulink environment which inherits all variables defined in Matlab workspace. The diagram is shown in figure 4.6 and can be easily reproduced. To produce valid models the scripts must be invoked in a particular sequence. This call sequence is given in listing A.8.

All codes given in this section are consistent with one another, operational and bug-free to the best of author's knowledge. The author grants a permission to use and modify these codes for research purposes. The author waives any responsibility if these codes are used for commercial purposes.

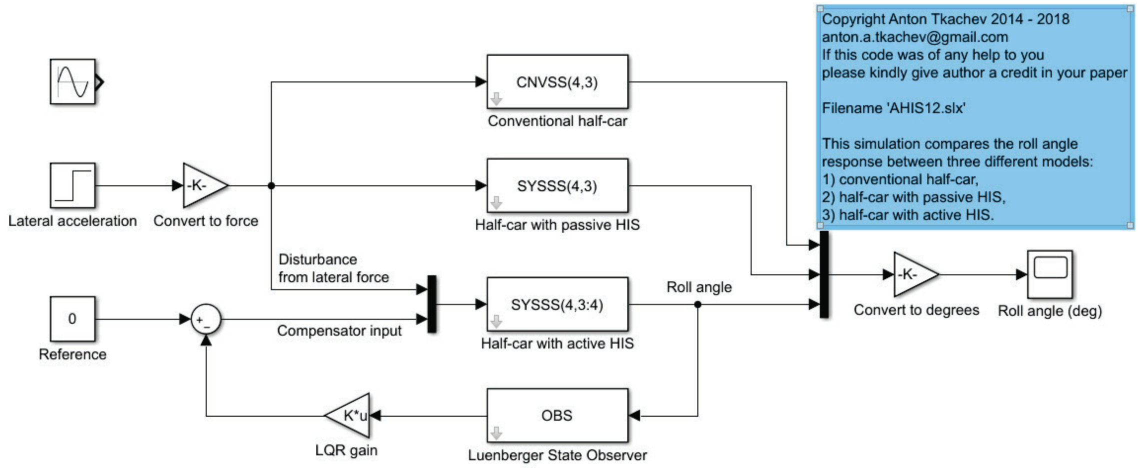

Figure 4.6: Simulink model for active HIS

Chapter 5

Simulations

5.1 Controller Validation

Before we can start simulations, it is essential to validate the controller which we designed in the previous chapter. There may be many ways of doing it. We prefer to compare the controlled and uncontrolled responses of the system when subjected to the same disturbance input as it is shown in figure 5.1. In the figure, one can see two sub-models being tested from disturbance input to roll angle output. To judge on the effectiveness of the controller designed we compare the Bode diagrams of the same model when it is controlled against the situation when the model is uncontrolled and exposes its passive behaviour, see figure 5.2. As seen in the figure, the diagram of the controlled system efficiently does not feature any resonant frequency at all and has consistently smaller magnitude than the uncontrolled model. At this stage, we can conclude that we are quite satisfied with the controller and can proceed to simulations.

5.2 Limitations of the Experimental Setup

In our simulations we pursue the following three objectives:

- to validate the simulation models,
- to demonstrate the feasibility of proposed methodology,
- to estimate the key physical parameters of the setup for design purposes.

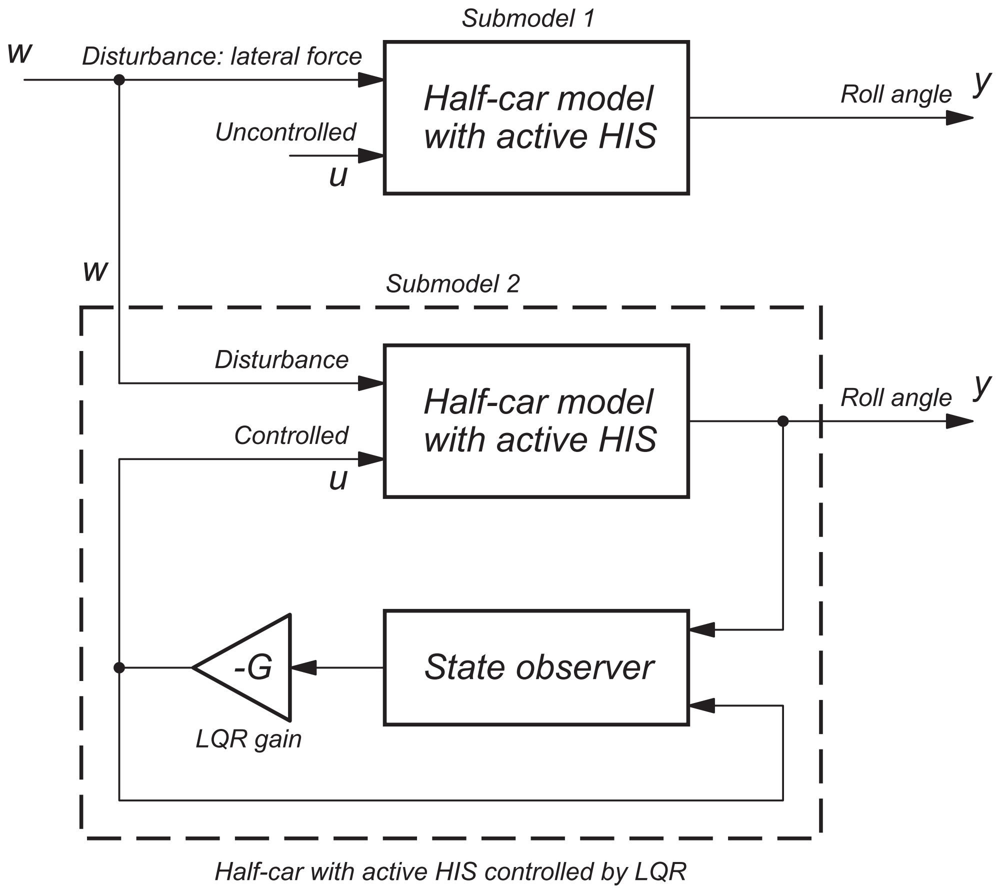

Figure 5.1: Controlled versus uncontrolled model comparison

Therefore we need to keep an eye on the maximum parameter ratings that the experimental setup can physically handle. For convenience, we listed the most critical parameters along with their absolute or desired maximum ratings in table 5.1.

Table 5.1: Desired maximum ratings

Variable	**Symbol**	**Limit**	**Unit**
Actuator displacement	Δx_a	100	mm
Actuator speed	$\Delta \dot{x}_a$	1000	mm/s
Ball screw axial load	F_a	10	kN
Mechanical power	P_m	1.0	kW
Motor speed	Ω_m	4000	rpm
Motor torque	T_m	3.2	N.m
Volumetric flow	Q_v	20	L/min
Differential pressure	ΔP	28	bar

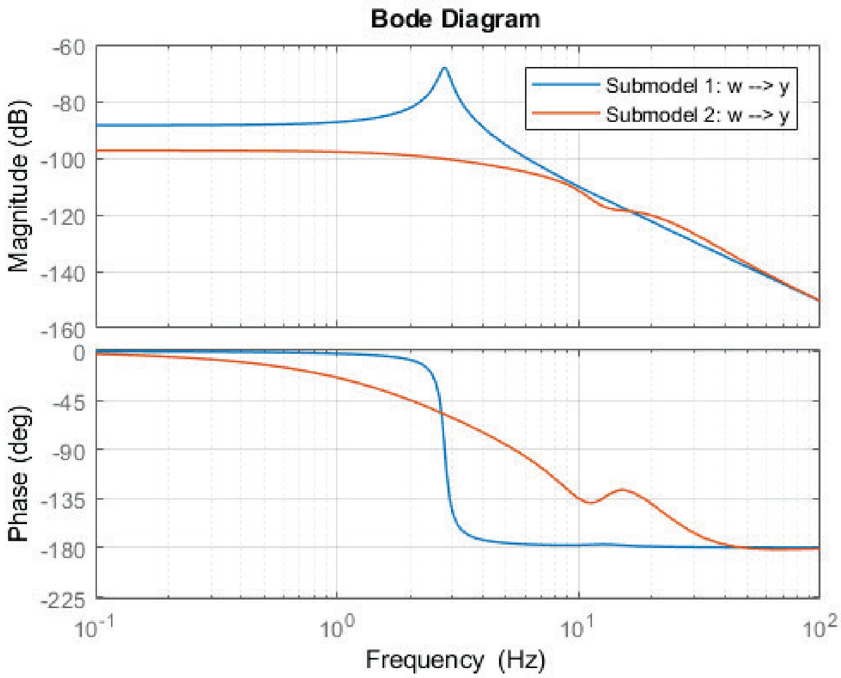

Figure 5.2: Controlled versus uncontrolled model Bode plot compared

5.3 Time Domain Simulations

Having in mind the goals, formulated above, we believe it will be sufficient to subject the system to three different scenarios in our simulations. The first scenario is a step input excitation. Since the Fourier spectrum of a step-function contains all possible signal frequencies, testing the system with a step input is an efficient way of judging about the stability and performance. Not only step input is helpful for testing system's stability properties, but also it will result in the system achieving its maximum limits across many physical parameters. The most critical simulation results for this scenario are shown in figure 5.3.

The second scenario used is a non-resonant sine-wave excitation. This scenario will help us understand how the system is going to perform in normal non-critical conditions. How much power is typically used, what are the typical loads, torques, pressures and so forth. See the simulation results in figure 5.4.

The third scenario is a sine-wave excitation with a frequency that would be resonant to the passive HIS system. This scenario is important because it concentrates all excitation energy in just one single harmonic and also forces the active elements of the system to work against such concentrated excitation and expose maximum performance possible. In other words, this is the worst case scenario the system must be capable of coping with. The simulation results are shown in figure 5.5.

5.4 Important Parameters Monitoring

In all simulations, we monitor the critical parameters of the setup to account for in our future designs. To conclude about the simulations we made a table of peak parameter values for three different testing scenarios, see table 5.2. From the table, one can see that in all three cases the maximum ratings were not exceeded. Therefore, here we conclude that the system we modelled proves the feasibility of the project and demonstrates sufficient level of anti-roll performance under different excitation conditions. We can also conclude that the stability of the system is significantly enhanced with the controller proposed.

Table 5.2: The table of peak parameter values

Parameter	**Maximum**	**Peak value**		
		Step	**Non-res.**	**Resonant**
Actuator displacement	100 mm	28 mm	25 mm	34 mm
Ball-screw axial load	10 kN	2.8 kN	2.5 kN	3.1 kN
Mechanical power	1 kW	0.42 kW	0.25 kW	1 kW
Motor speed	4000 rpm	340 rpm	300 rpm	400 rpm
Motor torque	3.2 N.m	2.2 N.m	2.1 N.m	2.5 N.m
Diff. pressure	28 bar	21 bar	22 bar	26 bar

5.5 Ride and Handling Ability Simulations

To understand the effect of active hydraulically interconnected suspension on vehicle ride and handling ability we simulate three scenarios: vehicle response to road roughness, vehicle response to single line shifting, vehicle response to double line shifting.

As seen from figure 5.6, in each of the three scenarios, active hydraulically interconnected suspension system controlled by a linear quadratic regulator significantly outperforms both the conventional suspension and the passive hydraulically interconnected suspension.

In response to road roughness, both conventional suspension and passive hydraulically interconnected suspension systems exhibit a lot of roll oscillation whereas the active hydraulically interconnected suspension effectively suppresses road disturbance and keeps vehicle roll angle to a minimum.

In response to single and double line shifting, the conventional suspension and passive hydraulically interconnected suspension oscillate and feature some transient behaviour. At the same time, the active hydraulically interconnected suspension eliminates all transition processes and makes the vehicle stick to the steering.

Overall we can conclude that the introduction of the active actuator into the hydraulically interconnected suspension enhances its performance drastically both in terms of ride comfort and also handling ability and driving safety.

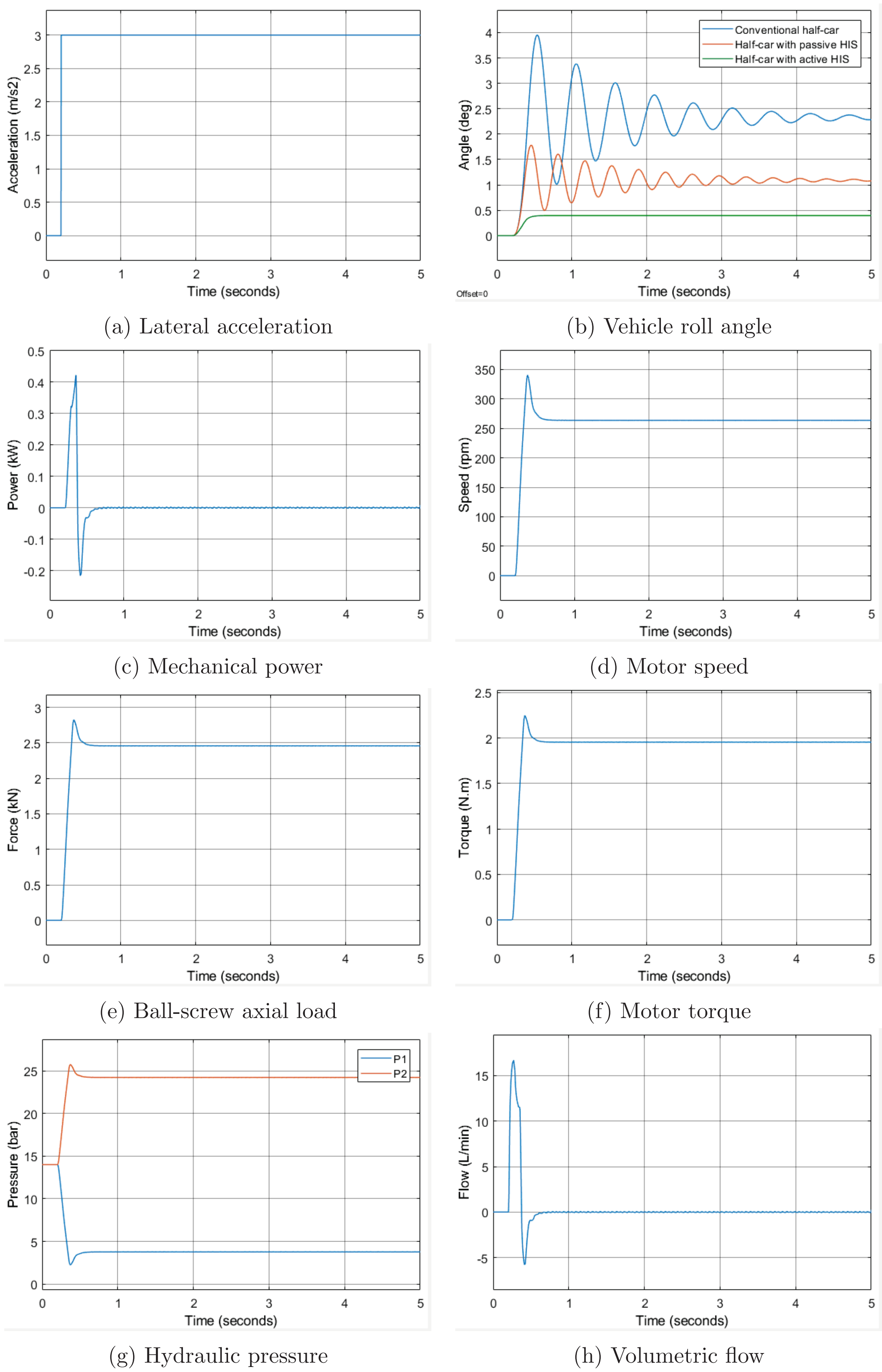

(a) Lateral acceleration
(b) Vehicle roll angle
(c) Mechanical power
(d) Motor speed
(e) Ball-screw axial load
(f) Motor torque
(g) Hydraulic pressure
(h) Volumetric flow

Figure 5.3: Step input responses

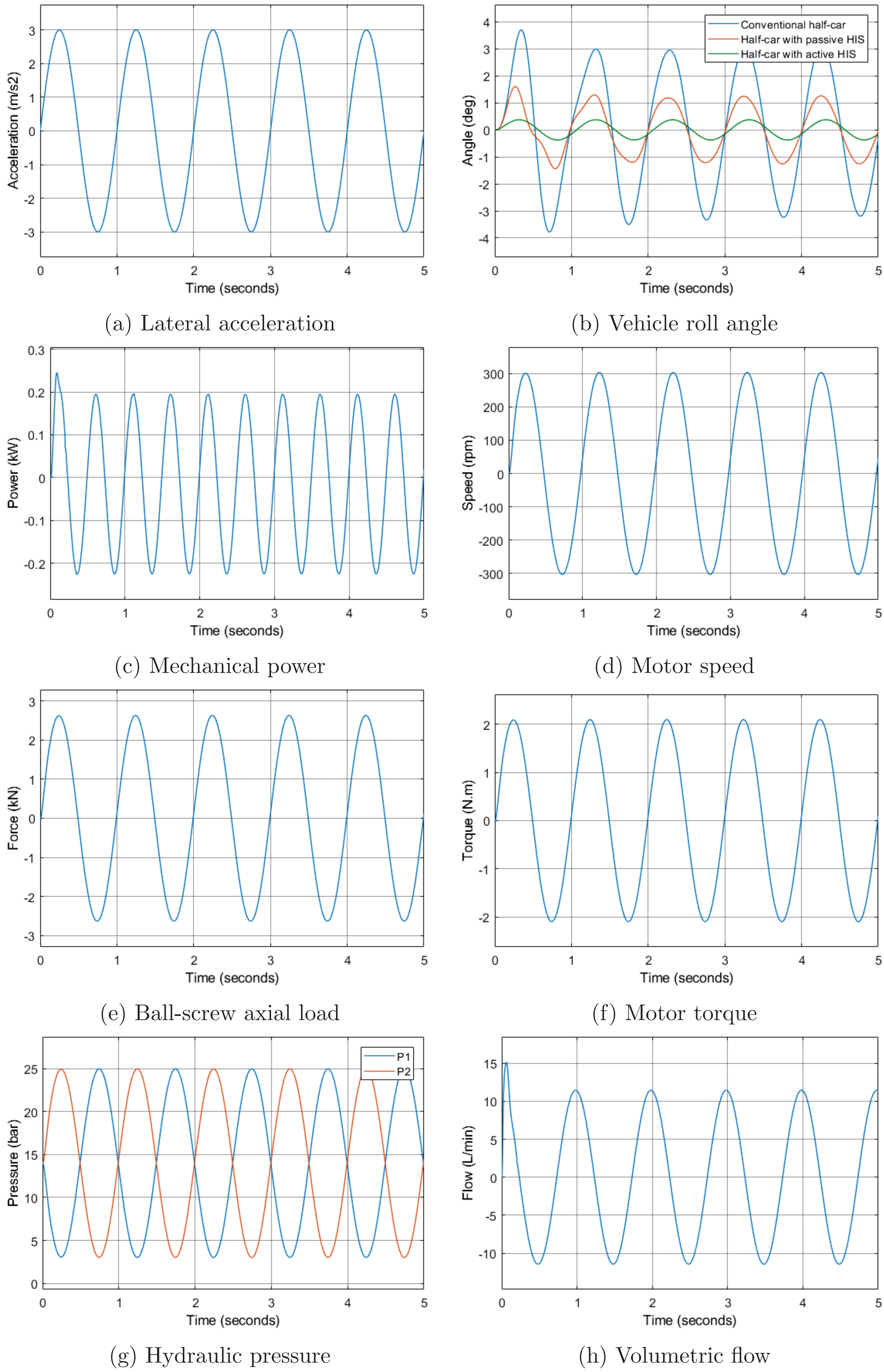

(a) Lateral acceleration

(b) Vehicle roll angle

(c) Mechanical power

(d) Motor speed

(e) Ball-screw axial load

(f) Motor torque

(g) Hydraulic pressure

(h) Volumetric flow

Figure 5.4: Non-resonant arbitrary sinewave input responses ($f = 1$ Hz)

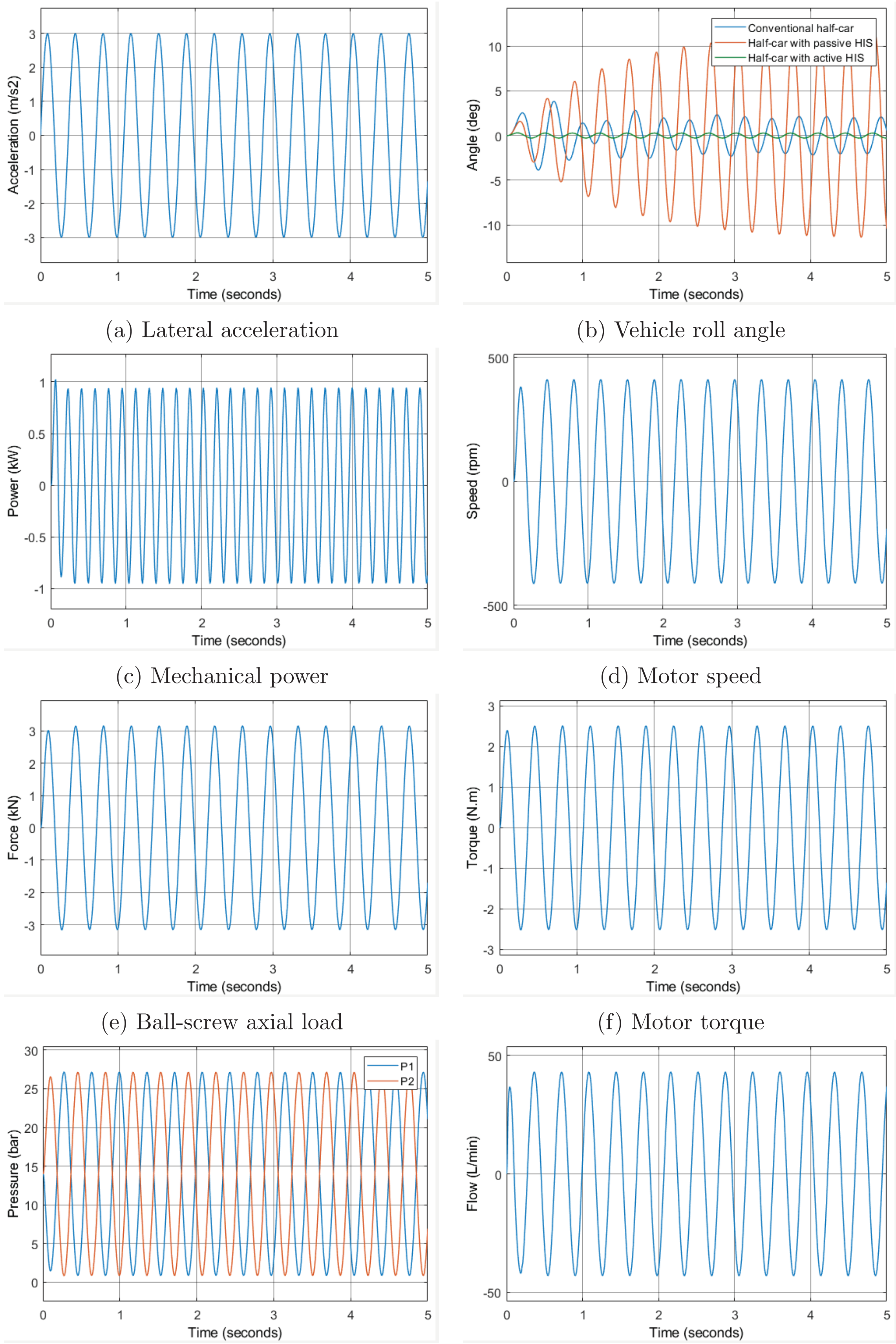

(a) Lateral acceleration (b) Vehicle roll angle

(c) Mechanical power (d) Motor speed

(e) Ball-screw axial load (f) Motor torque

(g) Hydraulic pressure (h) Volumetric flow

Figure 5.5: Responses to a sinewave input which is resonant for half-car with passive HIS ($\omega = 17.5$ rad/s)

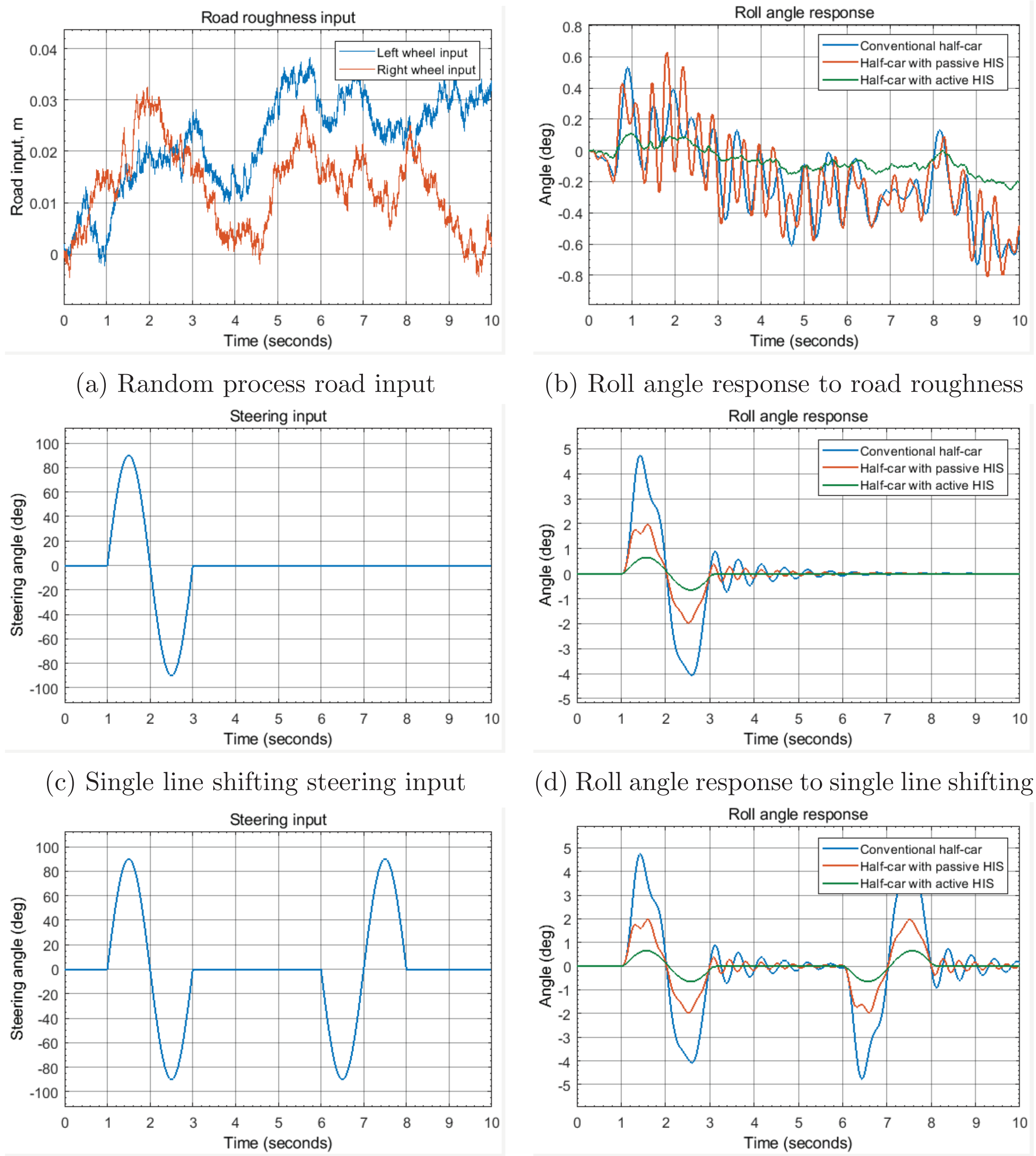

(a) Random process road input

(b) Roll angle response to road roughness

(c) Single line shifting steering input

(d) Roll angle response to single line shifting

(e) Double line shifting steering input

(f) Roll ang. response to double line shifting

Figure 5.6: Vehicle ride and handling ability simulations

Chapter 6

Commissioning Work

After the setup was ready, there was still a lot of commissioning work to be done before we could obtain first experimental results. In this chapter, we address the main stages of our commissioning work. And provide somewhat more detailed technical information about the experimental setup. To better understand the physical connections of the setup, please refer to diagram 6.1.

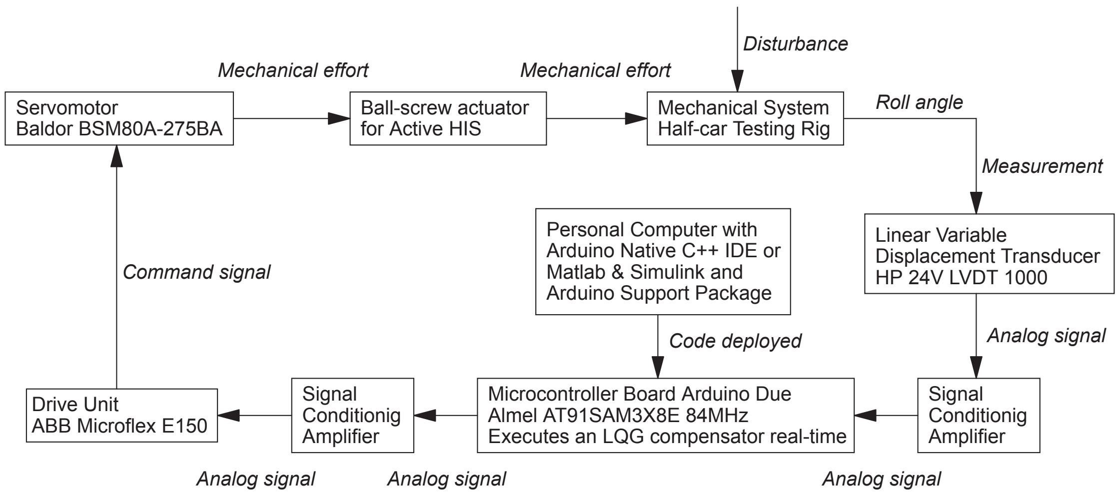

Figure 6.1: Physical connections diagram of the half-car testing rig closed loop control, anti-roll performance validation of the active HIS actuator

As seen in the diagram, the roll angle is measured with linear variable displacements transducers. The signals then pass through a signal conditioning amplifier to match the voltage levels between two different pieces of hardware. The signals are fed into the ADC inputs of the microcontroller, where a linear quadratic Gaussian compensator is digitally executed in real time. The output signals are collected from DAC pins of the micro-controller and are proportional to the desired motor speed. The signals are conditioned again before they are fed into the drive unit and then passed in a native form to the motor. The motor drives the ball-screw actuator in attempt to compensate the body roll of the half-car testing rig. The actuator itself is another physical system which needs to be accounted for in the compensator design. Thus, the control loop closes, and the process eventually stabilises at the roll angle equal to zero. The appropriate compensator is primarily designed using Matlab and Simulink or Arduino C++ IDE and the codes deployed on a micro-controller before the setup runs.

6.1 Linear Variable Displacement Transducers HP 24V LVDT 1000

A linear variable displacement transducer is an electromechanical device used to convert linear displacement into a voltage signal. In our project, we used Hewlett Packard 24V LVDT 1000. This is an old model which is no longer manufactured. The conversion principle of this particular model is electromagnetic. That is an LVDT work as a voltage transformer with the variable core. This was also the reason why the electromagnetic pickup noise was significantly high in our measurements. Nevertheless, we managed to tackle the noise problem with advanced control methods such as Kalman state observer. Below is the table of calibration 6.1 and the calibration line graph 6.2. The corresponding calibration equation is given in 6.1 which has its validity as high as $R^2 = 0.9947$.

$$D = -6.0037\,V + 133.61 \tag{6.1}$$

Table 6.1: LVDT calibration data

Voltage	Displacement
V	mm
0.015	132.05
0.028	134.86
-2.749	149.89
-1.005	140.10
-4.402	159.93
-6.201	170.12
-7.750	180.73
-9.550	189.70
-10.030	196.35
-10.690	196.60

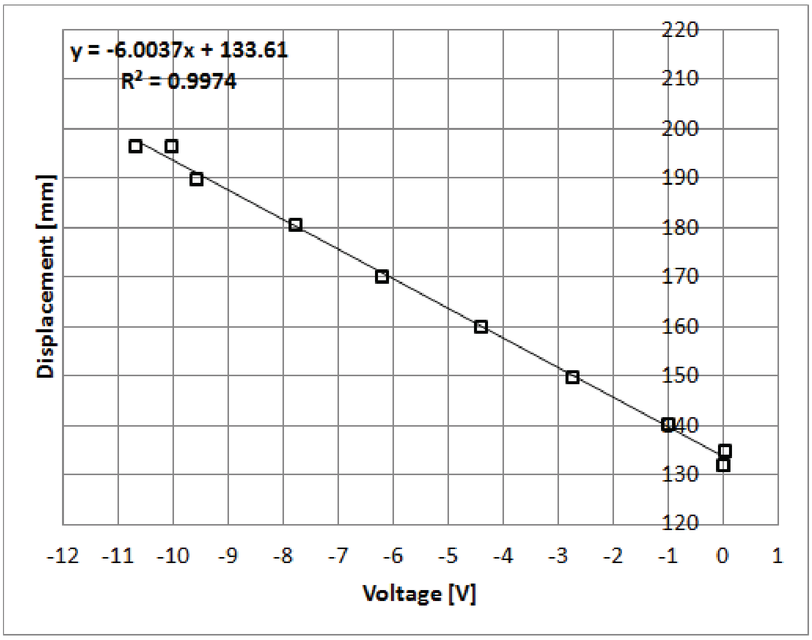

Figure 6.2: LVDT calibration line

6.2 Hydraulic Pressure Transducers TE Connectivity AST4100

A pressure transducer is a device which converts pressure readings into a voltage signal. In this project, we used TE Connectivity AST4100 series pressure transducers part number C00100B3D0000. The specifications of the transducers are given in 6.2. As per the specification, the transducer maps pressure range from 0 - 100 bar to a voltage range from 1 - 5 V. Therefore, we can find corresponding calibration equations as shown in 6.2, where P_1, V_1 and P_2, V_2 are the pressures and transducer voltages on the left and on the right of the HIS respectively. The $V_{0\,left} = 1.036$ V and $V_{0\,right} = 0.940$ V are the corresponding offset voltages.

$$\begin{aligned} P_1[\text{bar}] &= 25 \cdot (V_1 - 1.036) \\ P_2[\text{bar}] &= 25 \cdot (V_2 - 0.940) \end{aligned} \tag{6.2}$$

Table 6.2: Pressure Transducer AST4100-C00100B3D0000 Specifications

Parameter	**Value**
Process Connection	1/4” BSPP Male
Pressure Range	0 - 100 Bar
Pressure Unit	Bar
Output Voltage Range	1 - 5 V

6.3 Baldor Servomotor BSM80A-275BA

In this project, we used a servomotor model Baldor BSM80A-275BA. The servomotor’s parameters are listed in table 6.3.

6.4 ABB Motor Drive Microflex E150

The motor was driven by the ABB Microflex E150 universal motor drive. Below, we give some information about the drive which is important to the project. ABB Microflex E150 has the following features:

- is a single axis drive for AC brushless servo motors,
- has a current rating of 6 A,
- can be powered with single phase 115/230V or 230V 3 phase AC voltage,
- position, velocity and current control,
- has two analog control inputs ±10 V,
- analog inputs are subject to first order embedded filter,
- works with ABB Mint Workbench software,
- connects to a PC via USB or Ethernet interface.

Table 6.3: Baldor Servomotor BSM80A-275BA Specifications

Parameter	**Value**	**Unit**
Max Speed	7000	rpm
Peak Torque	12.8	N.m
Rated Torque	3.20	N.m
Rated Speed	4000	rpm
Agency Approvals	CE CSA TUV UR	-
Ambient Temperature	25	°C
Bearing Grease	TypePolyrex EM	-
Duty Rating	CONT	-
Insulation Class	F	-
Motor Lead Quantity/Wire Size	3 @ 18 AWG	-
Mounting Arrangement	F1	-
Rated Current	4.28	A
Rated Power Output	1.25	kW
Number of Poles	4	-
Peak Current	16.3	A

6.5 Signal Conditioning Amplifier

As mentioned above, ABB Microflex E150 drive takes two analog control signals rated at ± 10 Volts. At the same time, the LVDTs produce can produce a signal of approximately ± 6 Volts. Moreover, there is a micro-controller in between the LVDTs and the motor drive, which encloses the control loop. As per the controller specifications, that are also given below, the microcontroller is only capable of handling signals in the range of 0 - 5 Volts, that is the microcontroller's ADC and DAC are both rated at the range 0 - 5 Volts. Therefore, we needed to make a signal conditioning amplifier to scale and shift the signals to the appropriate ranges between different pieces of hardware.

Thus, we designed a general purpose tunable amplifier for signal conditioning. The schematic of the amplifier and the simulation diagram are shown in figure 6.3. The amplifier is an analog voltage-to-voltage converter with the possibility of gain and offset adjustment.

The amplifier allows tuning the gain and the offset in a wide range which is helpful when one needs to do analog signal manipulations such as discussed above. The SPICE simulation diagrams are shown in figure 6.4.

We soldered four units of this amplifier and used them for analog signal conditioning in our project. The 3D cad of a PCB is shown in figure 6.5 and the bill of materials for making a single unit is given in table 6.4.

The amplifiers were used for signal scaling and shifting as an analog interface between the LVDT transducers and the microcontroller and also between the microcontroller output and the Flex II Drive unit.

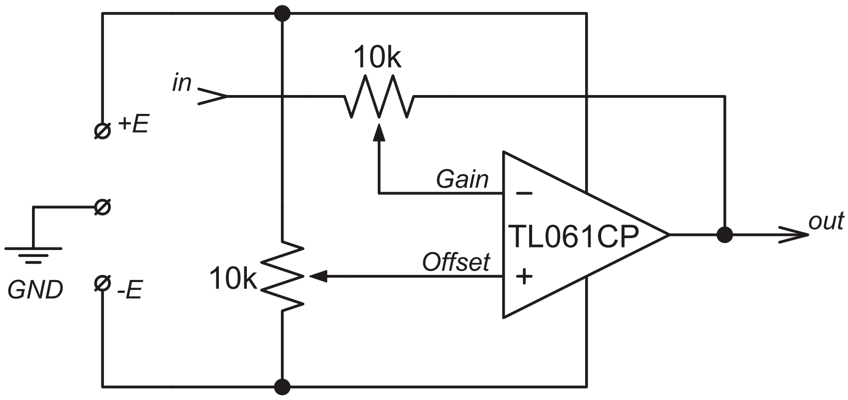

(a) Schematic capture

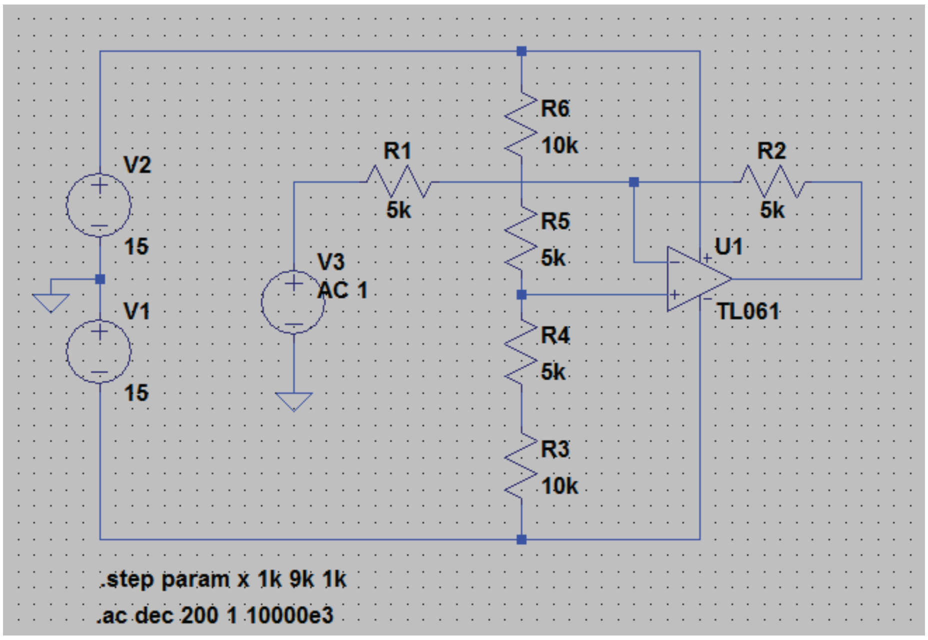

(b) SPICE simulation diagram

Figure 6.3: Signal conditioning amplifier

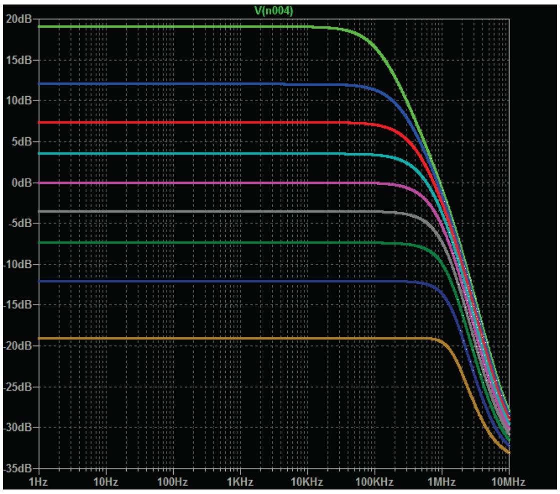

(a) Gain tuning

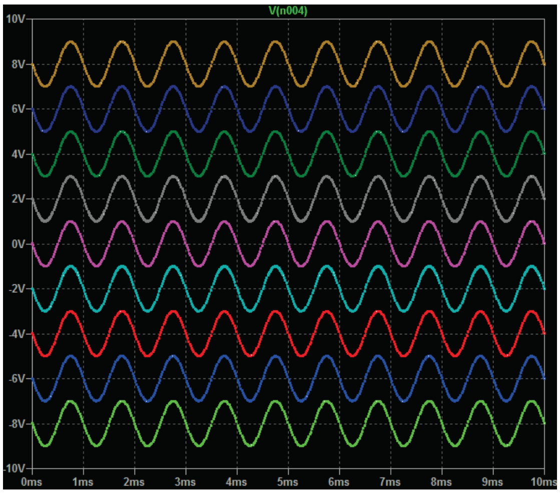

(b) Offset tuning

Figure 6.4: Signal conditioning amplifier amplifier SPICE simulations

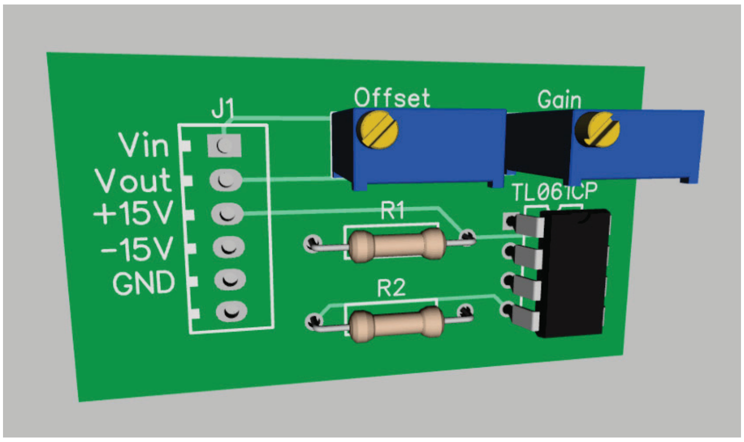

(a) CAD model of PCB

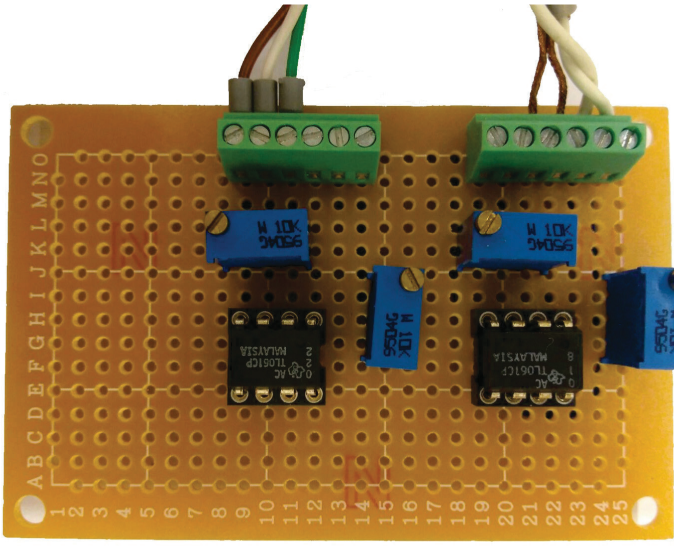

(b) Prototype

Figure 6.5: Signal conditioning amplifier

Table 6.4: Bill of materials for signal conditioning amplifier

Component	Manufacturer	P/N	Qty
Operational amplifier	Texas Instruments	TL061CP	1
Metal film resistor 10kOhm	TE Connectivity	LR1F10K	2
Trimmer Resistor 10kOhm	Bourns	3296W-1-103LF	2
PCB Terminal Block	Phoenix Contact	1725698	1

6.6 Dynamic Control with a Micro-Controller

We used Arduino Due micro-controller board for dynamic control. Arduino provides an outstandingly cheap alternative to such commercial products as, for example, LabVIEW Real-Time Module (A$4,741). The cost of top Arduino board model is two orders of magnitude less and is as low as only A$30. Despite the low price, Arduino Due board is capable of handling real-time control loops at relatively high sampling frequencies with the sampling time as fast as approximately 100 μs. The specifications of the board are given in table 6.5. One should note that there are multiple ways to go about programming Arduino. In this project, we used two different ways of doing it. The first way is to do C++ coding in native Arduino IDE. With this one gets more flexibility as well as more responsibility to handle lookup arrays, timer interrupts, memory allocation, time-efficient coding and so forth. This allows one to produce faster codes at the cost of more work and programming skill required to achieve the same result. On the other hand, one can use Arduino Support Package for Simulink. With that, one can create the codes that are more complicated although at the cost of slightly longer time of execution. With Arduino Support Package for Simulink, only the essential knowledge of hardware side is required from an engineer. Namely, one needs to specify the sampling rate which complies with the hardware capabilities and the solving method such as, for instance, first-order Euler's algorithm.

6.6.1 Arduino Coding with Native C++ IDE

In this project, we started debugging our experimental setup with Arduino IDE implementing a Proportional Integral Derivative compensator for the system in the velocity form.

Table 6.5: Arduino Due micro-controller board specifications

Specification	**Value**
Microcontroller	AT91SAM3X8E
Operating Voltage	3.3V
Input Voltage (recommended)	7-12V
Input Voltage (limits)	6-16V
Digital I/O Pins	54
Digital PWM Outputs	12
Analog Input Pins	12
Analog Output Pins	2 (DAC)
Total DC Output Current	130 mA
DC Current for 3.3V Pin	800 mA
DC Current for 5V Pin	800 mA
Flash Memory	512 KB
SRAM	96 KB
Clock Speed	84 MHz
Length	101.52 mm
Width	53.3 mm
Weight	36 g

6.6.2 PID Controller in Velocity Form

In this application, the actuator is a servomotor. Therefore, the actuator displacement cannot be directly changed but only altered by motor speed.Thus, we need to use the control algorithm in velocity form which will have its output signal proportional to the motor speed. In "s"-domain the velocity form for a PID controller is given by the the expression 6.3, where K_p, K_i, K_d are proportional, integral and derivative gains respectively.

$$\begin{aligned} C(s) &= s\left(K_p + \frac{K_i}{s} + sK_d\right) \\ C(s) &= sK_p + K_i + s^2 K_d \end{aligned} \tag{6.3}$$

Thus, the feedback signal is differentiated once for the proportional action and twice for the derivative action of the controller. One should note that the s operator gain grows as fast as the angular frequency ω of the signal, and the s^2 operator gain - grows as fast as ω^2. Therefore, high-frequency noise, although initially negligible, is amplified with extremely high gains after the differentiation and the controller output becomes unacceptable because of the noise. This effect is often observed as the chattering of the motor or high-frequency spikes on the control signal waveform.

6.6.3 The Effect of Sensor Noise

Suppose, a low-frequency signal is collected from a sensor. For simplicity we assume a sine-wave (see equation 6.4) with an amplitude of $a = \sqrt{2}$ and angular frequency of $\omega = 1$ rad/s. Let us now add some white noise $\xi(t)$ (see figure 6.6(b)) with a relatively small variance of $\sigma = 1 \cdot 10^{-3}$ to the original signal. Note that the noise added to the signal is so small that it is not even seen by naked eye on the graph 6.6(a). Using the definition of signal-to-noise ratio (see figure 6.5) we obtain $SNR_u = 60$ dB for the initial signal which is shown in figure 6.6(a).

$$u(t) = a\sin(\omega t) + \xi(t) \tag{6.4}$$

$$SNR_{dB} = 10\log_{10}\left(\frac{\sigma^2_{signal}}{\sigma^2_{noise}}\right) \tag{6.5}$$

Suppose the controller has a sampling rate of $f_N = 1$ kHz meaning that the sampling period is $T = 1 \cdot 10^{-3}$ seconds. Then, it can be shown that 1st derivative of the signal $\dot{u}(t)$ will have signal-to-noise ratio of $SNR_{\dot{u}} = -2.9$ dB, see figure 6.6(c). And 2nd derivative $\ddot{u}(t)$ will have $SNR_{\ddot{u}} = -67.8$ dB, see figure 6.6(d).

In our experiments, we measured the signal-to-noise ratio of the sensor signals to be as small as approximately $SNR = 30$ dB. Thus, we can conclude that a PID compensator is too sensitive to noise in the measurement signals and fails to provide acceptable performance under the condition of even tiny noise in the sensors. However, we can try to design a discrete filter to make the collected signals somewhat smoother.

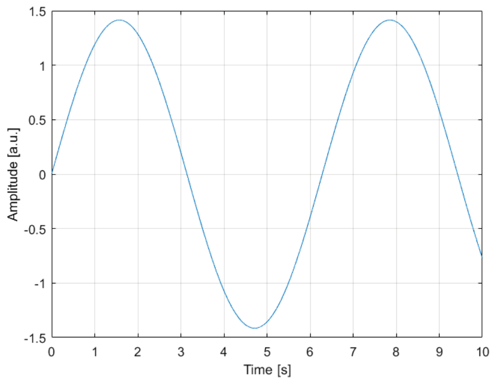

(a) Original signal

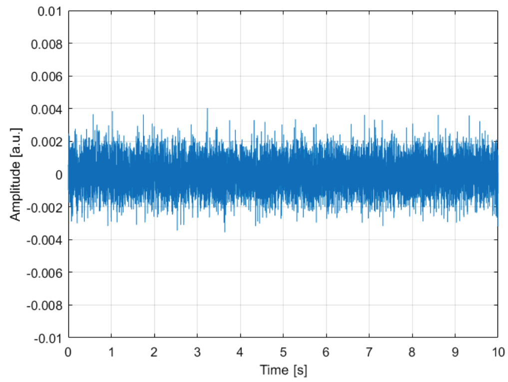

(b) Gaussian noise

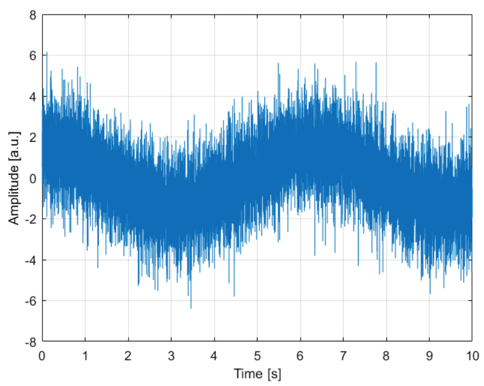

(c) First differentiation

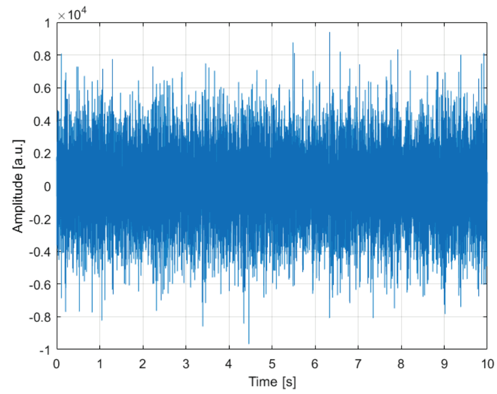

(d) Second differentiation

Figure 6.6: The effect of noise on PID controller

6.6.4 Discrete Filter Design

To make the measured signals smoother we can implement one of the common discrete filters on the controller. Typical frequency responses of most commonly used filters are shown in figure 6.7. The figure is taken from [47]. We choose to use an elliptic filter as it has the sharpest cut-off region of all.

A digital low-pass filter in discrete transfer function form can be easily designed with Matlab command `[b,a] = ellip(n,Rp,Rs,Wp);`, where `n` is the order of the filter, `Rp` is the passband peak to peak ripple measured in dB, `Rs` is stopband attenuation in dB, `Wp` is the normalized cut-off frequency measured in fractions of Nyquist frequency. Vector `b` contains discrete transfer function numerator coefficients. And vector `a` contains discrete transfer function denominator coefficients.

Although with the discrete low-pass filter the measurement signal becomes much smoother it is also subjected to a significant phase delay which imposes a severe

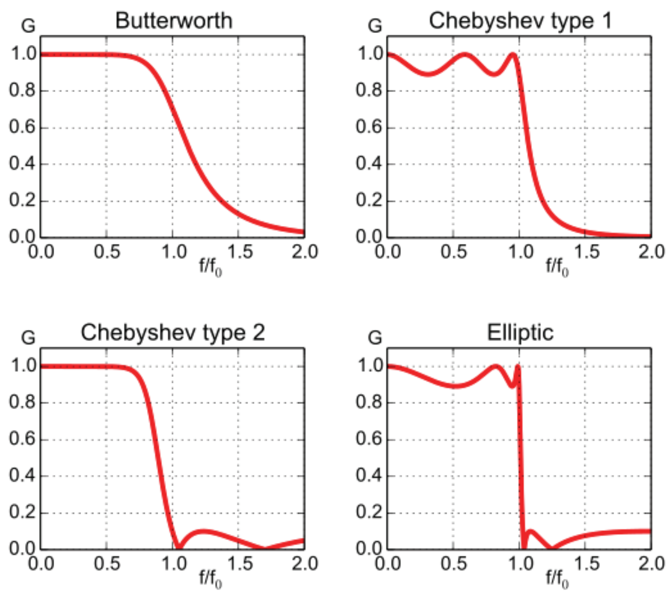

Figure 6.7: Typical frequency responses of most commonly used filters

limitation on the stability of the system. As we found in our experiments, it is almost impossible to tune a PID regulator to a detectable level of performance without making the system unstable. Overall, we conclude that a PID controller, in general, is not suitable for the application due to its high sensitivity to noise and difficulties with tuning. The only part of PID that worked for us was the integral term alone, which is known to be noise robust but slow.

6.6.5 Using Timer Interrupts

However, given a higher sampling rate, one could try using PID in their applications. The author would like to emphasise here one important aspect of dynamic control, which is timer interrupts. It is often wrongly practised to use `loop()` function with `delay()` or `delaymicroseconds()`. The author of the thesis believes this to be a mistake. With such an approach one can not guarantee the consistency of sampling periods, and thus it can lead to any unexpected controller behaviour which will also be difficult to debug.

Instead, one should use timer interrupts and interrupt service routine as demonstrated in the listing below. In listing A.9 is given the C++ code implementing discrete elliptic filter and a PID regulator in velocity form.

In our experiments we used timer interrupts setting of as fast as 1 millisecond in order to guarantee the execution of the previous iteration to be finished by the time the new iteration starts. The choice of this sampling time was made keeping in mind that microcontroller clock speed is as high as 84 MHz.

6.6.6 Matlab and Simulink Arduino Support Package

Another way of programming Arduino micro-controllers is to use Arduino Support Package for Matlab and Simulink. With Arduino for Matlab one can send commands to the board and execute scripts. Simulink support package for Arduino offers all the necessary function blocks (see figure 6.8) to design and execute complex control loops in real time.

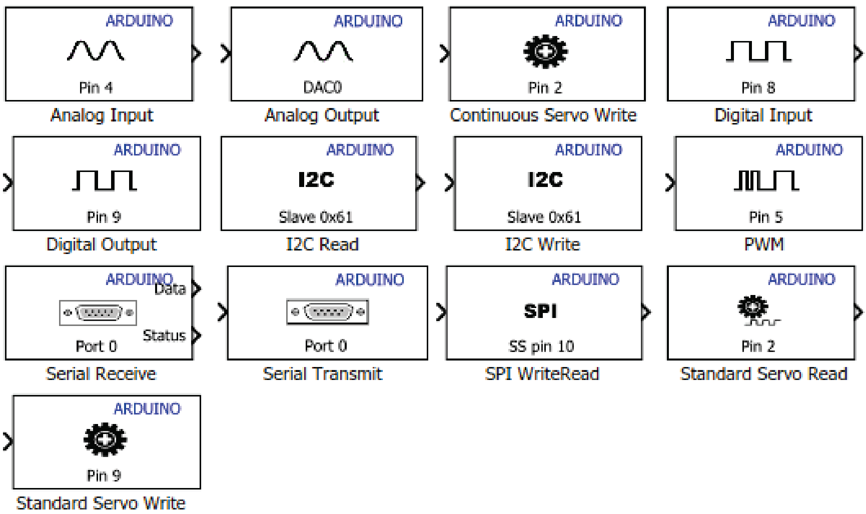

Figure 6.8: Simulink function blocks to work with Arduino

In our Simulink control diagram, we used the sampling time of 1 ms to allow more time for the controller to solve high order differential equations. And we chose the integration method as Euler first order integration to achieve faster performance sacrificing some accuracy which is not so crucial in this real-time application.

Thus, we conclude here that in this section we reviewed most of the commissioning work that we had done. However, we did not mention any work related to the project but not containing any research component such as building and assembling hardware parts and any other work of the kind.

Chapter 7

Identification Experiments

To effectively design a controller for a real physical system one needs to identify the sub-models of interest that will be involved in the design of the compensator. Therefore, in this chapter, we discuss a method of sub-system transfer function identification that we adopted from industry and successfully applied in our project. We should say that in Control Engineering the feedback controllers are classified into two major categories, namely: the model independent methods and the model dependent methods. While model-independent techniques such as, for example, Proportional Integral Derivative control, generally do not require the knowledge of the sub-model and can be tuned easily by trial and error, the other category of model-dependent methods, such as State-Feedback, necessarily require the preceding knowledge of the sub-system transfer function or state-space. As we discussed in chapter 6, Proportional Integral Derivative controller fails to deliver an appropriate level of stability and roll angle reduction for our particular system. Therefore, we needed to think of a more advanced controller to have more flexibility in our designs and achieve higher stability and robustness of the control system.

The following forced vibration experiment was suggested to the author by his co-supervisor Associate Professor Steven Su. The experiment was conducted by the author of this thesis within approximately six months time which also included some commissioning and troubleshooting work. The experimental data were analysed and processed by the author entirely independently as it will be described below in this chapter. For the convenience of other researchers, the author will share the codes for Fourier Analysis of the experimental data too.

7.1 Forced Vibration Experiment

Forced vibration experiment is a powerful technique used for real systems identification. It provides one with accurate equations of the system tested, that can be formalised into a Linear Time-Invariant model, be it a state-space or a transfer function, and allows one to design a model-dependent advanced controller such as Linear Quadratic Gaussian controller or any other of the kind.

7.1.1 Idea of Forced Vibration Experiment

As it is commonly practised when solving linear differential equations to solve the homogeneous equation with zero right side first, and then superimpose that solution with a particular solution for a particular right side, the same procedure can be implemented not only analytically but experimentally on a real system as well.

Solving homogeneous equation from the experimental perspective means free vibration experiment when we excite the system with an external input, either a step or an impulse and then observe system's free oscillation until it entirely decays. Finding a particular solution for an inhomogeneous equation means that we can subject the system to an arbitrary input and measure the response. If we choose a sine-wave of a specific amplitude and frequency to be the arbitrary input, then, as known from the theory of second order systems, the system will respond with a sine-wave of the same frequency but generally of different amplitude and phase. By measuring these two quantities, the amplitude and the phase, we can identify system's transfer function complex value at current frequency, which also places one data point on the Bode diagram of the system. Thus, we can scan system's responses over a range of frequencies of the interest. Provided the number of observations at different frequencies is sufficient, and the frequency range was chosen appropriately one can identify system's transfer function or state-space model using, for example, Matlab System

Identification tools.

One may argue here on the point that an experiment with a step input followed by model identification in time domain only could be sufficient here. The author, then, would argue back that time domain identification is effective only for second-order models, whereas a system can be generally of a higher order. Moreover, if a system being identified contains errors or noise of any nature of origin, then time domain identification becomes completely ineffective regarding the uncertainty of the identified models. As opposed to time domain identification, frequency domain identification yields a result of a much higher fidelity and reliability.

7.1.2 Experiment Layout

As mentioned above, when we subject a system to a sine-wave input excitation the system will respond with a sine-wave of different amplitude and phase. To understand this experiment better we made a quick simulation diagram 7.1 explaining the idea of what is tested, where the excitations are fed and the signals collected.

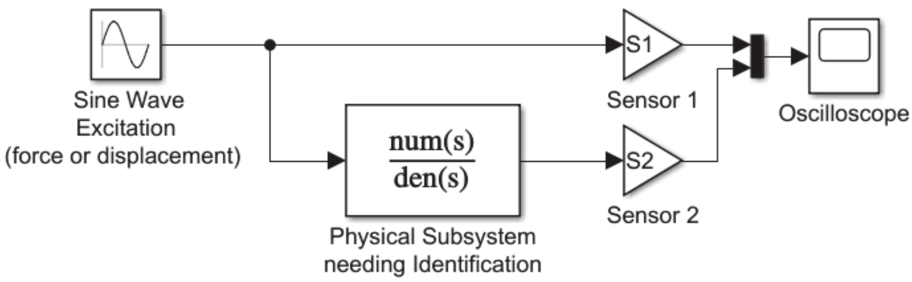

Figure 7.1: Schematic diagram of the forced vibration experiment

As shown in the diagram 7.1, we are testing a physical subsystem by subjecting it to a sinusoidal input excitation which can be any real physical quantity such as force, displacement or actuator speed. The subsystem will physically respond to this with another real physical quantity, for example, roll angle or vertical displacement or what not. To identify the subsystem model equations, we need to collect the signals from sensors measuring both the above quantities at the same time synchronously. This is usually done with an oscilloscope. After measuring the signals at one particular frequency we then switch the excitation input to a different frequency and repeat the procedure as many time as needed to cover the range of frequencies of the interest. The range of frequencies can be estimated from a rough mathematical model or found experimentally. In our case, all the sub-models that we identified in our experiments fall in the range from 0.1 to 10 Hz.

7.2 Fourier Analysis Methodology

Like we already said, every time we measure two graphs: the input and the output. Here, we would like to demonstrate how different can be the simulated graphs and the real ones in the same situation. In figure 7.2 are shown the simulated and the experimental graphs of the same two physical quantities. One can see how on the left figure the graphs are smooth and nice, having neither an offset or drift nor any other distortions. The other graph on the right is obtained in the experiment, and it has an offset. Moreover, it is slightly drifting in time towards the bottom, not to mention the noise which is the result of the uncertainties and mechanical noise in the system as well as sensor errors and electromagnetic pickup and other reasons.

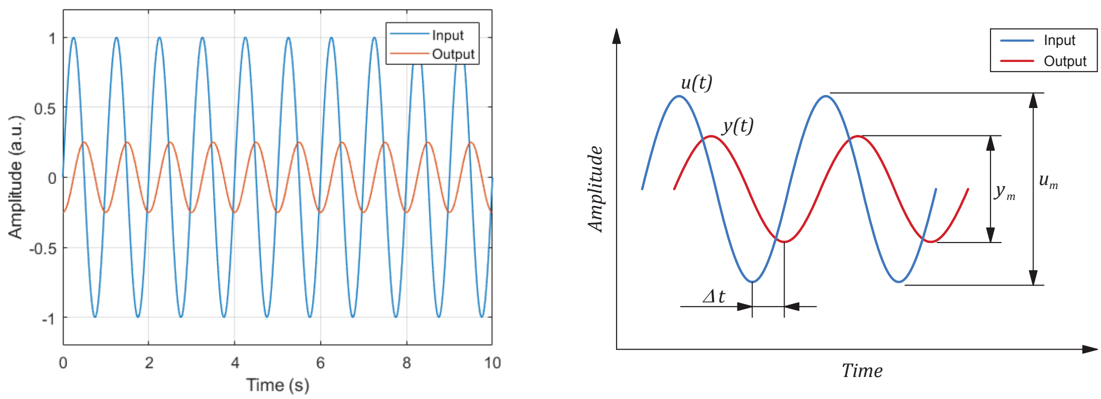

(a) Simulation (b) Time domain analysis

Figure 7.2: Sine-wave excitation response

Although the experimental graphs can sometimes be distorted a lot by the factors of influence mentioned above, we can still extract clean, useful information from our measurements using a powerful technique of Fourier Analysis. In figure 7.3 are shown the analysis graphs. On the one hand, we could analyse all signals in time domain. If we denote $u(t)$ as the input excitation signal and $y(t)$ as the output system response, then this two signals, in theory, are sinusoids that are characterised by their amplitudes u_m and y_m and phases φ_u and φ_y. Equation 7.1 gives the expressions for $u(t)$ and $y(t)$ explicitly, where ω is the excitation frequency which is common for both input and output signals.

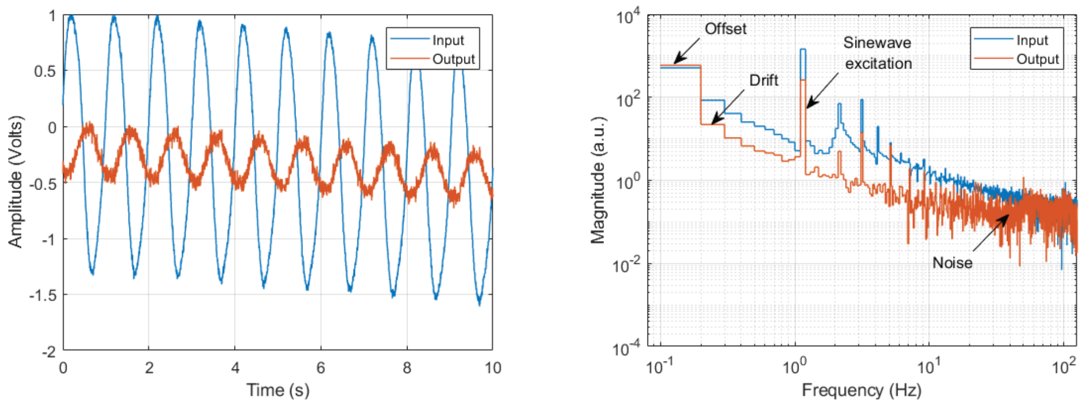

(a) Measured signals (b) Amplitude spectrum

Figure 7.3: Typical experimental data

$$
\begin{aligned}
u(t) &= u_m \sin(\omega t + \varphi_u) \\
y(t) &= y_m \sin(\omega t + \varphi_y)
\end{aligned}
\tag{7.1}
$$

To place a new data point on Bode plot, we need to find two quantities that are the magnitude and the phase. Let $U(\omega)$ and $Y(\omega)$ be the complex Fourier images of the original signals $u(t)$ and $y(t)$ respectively. Both images U and Y are complex numbers having a magnitude and a phase (see equation 7.2). As per the properties of Fourier transform, these two quantities of a complex number: magnitude and phase relate to those of a sine-wave as given by the equation 7.3.

$$
\begin{aligned}
U(\omega) &= U_m(\omega)\, e^{i\varphi_u(\omega)} \\
Y(\omega) &= Y_m(\omega)\, e^{i\varphi_y(\omega)}
\end{aligned}
\tag{7.2}
$$

$$\varphi_y - \varphi_u = \omega\,\Delta t$$

$$\frac{Y_m}{U_m} = \frac{y_m}{u_m} \tag{7.3}$$

Therefore, we can characterise a data point on Bode diagram with another complex number $W(\omega)$ which is the ratio of two Fourier complex amplitudes: output over the input, see equation 7.4. The number $W(\omega)$ signifies how a sinusoidal signal of frequency ω is changed while passing through the system regarding its amplitude and phase. Thus, at any given excitation frequency ω we can decompose both input and output signals into a spectrum with fast Fourier transform. Then in the spectrum we find the components that relate to the excitation frequency ω and take the ratio of their complex amplitudes which makes one point on Bode diagram at frequency ω. Of course, it is possible to automate the entire process. We should say that the benefit of using Fourier transform and spectral analysis is not only automation but also Fourier transform allows us to disregard all signal distortions such as noise, offset and drift, and find the actual amplitude and phase of a sinusoidal signal. Such algorithmic spectral analysis is also free from human error as opposed to one taking measurements of amplitudes and phase shifts between two noisy signals with an eye and a ruler.

$$
\begin{aligned}
W(\omega) &= W_m(\omega)\; e^{i\varphi_w(\omega)} \\
W(\omega) &= \frac{Y(\omega)}{U(\omega)} \\
W_m(\omega) &= \frac{Y_m(\omega)}{U_m(\omega)} \\
\varphi_w(\omega) &= \varphi_y(\omega) - \varphi_u(\omega)
\end{aligned}
\tag{7.4}
$$

7.3 Fourier Analysis Using Matlab

Since in our experiments we obtained hundreds of measurements, we needed a simple and powerful method to analyse the experimental data. Therefore, we developed a code script in Matlab to automatically calculate the magnitude and phase out of a given oscilloscope waveform file. The code in listing A.10 can automatically identify the excitation frequency and find the corresponding complex amplitudes of the input and output signals at that particular frequency. Then it will divide the two complex amplitudes and take the modulus and the argument of the resultant complex number to identify the magnitude and the phase.

In our experiments we were collecting signals of the input disturbance, the output response and the sometimes there was another reference signal which was the command to the disturbance actuator. We were saving the waveforms from an oscilloscope to a CSV file (Comma Separated Values), which is then easily readable by both Matlab and Microsoft Excel. In one experiment we would obtain a series of CSV files that were then processed with the Matlab script. The script first reads a CSV file and parses it into a data structure. Then it identifies the columns of the data structure with variables such as time, reference, input and output. The excitation frequency can be found from the input signal as the frequency featuring highest magnitude in the spectrum of the input signal. If there is a reference signal, then the excitation frequency is obtained from the reference in the same manner. After that, the respective complex amplitudes of the input and the output are found and the magnitude and phase calculated. The results are appended to the end of an output CSV file which is then used for system identification.

7.4 Control Diagram of the Half Car Testing Rig

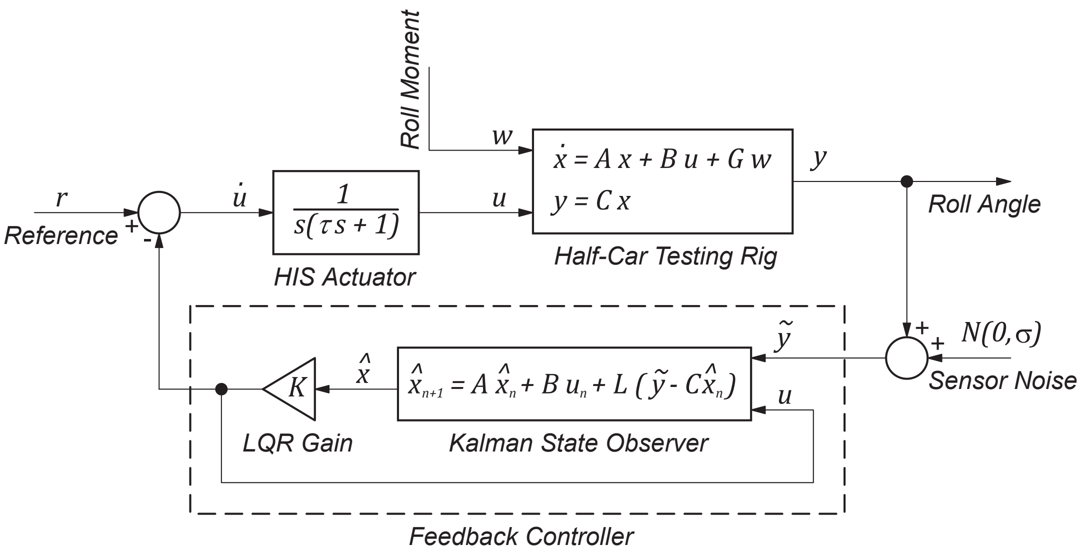

Figure 7.4: Control diagram of the half-car testing rig

The control diagram of the experimental setup is shown in figure 7.4. In the figure, it is seen that the setup includes many sub-models that represent different physical systems as well as those executed numerically on a microcontroller, such as, for example, Kalman state observer. The work-flow of the setup can be described as follows. The setup is subjected to an external disturbance which is created by the roll actuator pushing against the roll centre bearing and applying the roll moment to the vehicle body. In response to this external input the body of the setup inclines which is measured by the linear voltage displacement transducers on the left and the right. The measurements are fed into the analog-digital-converter input of the micro-controller and numerically processed by the Kalman state observer algorithm.

The micro-controller then generates an output signal proportional to the desired speed of the motor. The signal voltages are set on microcontroller's digital-analog converter pins. The motor follows the commands from micro-controllers and drives the actuator of the hydraulically interconnected suspension system to oppose the roll moment disturbance and suppress the absolute value of roll angle as well as the roll rate.

According to the diagram 7.4, in our experiments we identified the following subsystem models:

- the actuator, $\dot{u}$ to u - from motor speed command to actuator displacement;
- the pressure, the hydraulic pressures response to actuator displacement u;
- the half-car model, u to y - from actuator displacement to roll angle;
- the combined model, $\dot{u}$ to y - from motor speed command to roll angle;
- the disturbance, w to y - from roll moment disturbance to roll angle when uncontrolled (open loop);
- the disturbance, w to y - from roll moment disturbance to roll angle when controlled with an LQG compensator at the moderate setting;
- the disturbance, w to y - from roll moment disturbance to roll angle when controlled with an LQG compensator at the aggressive setting;

Note that the last two are not discussed in this chapter but will be given in Chapter 9 - Compensator Validation Experiments. Below follow the results of the experimentally identified models that will be used for the design of a real linear quadratic Gaussian compensator in the next chapter. Each identification experiment is presented with a Bode diagram showing both the identified model and the experimental data points and an identification report which contains the validity value in percent as well as the values for Akaike's final prediction error and mean squared error. The table with the experimental data follows each identified model.

7.5 HIS Actuator $\dot{u} \to u$ Identification Experiment

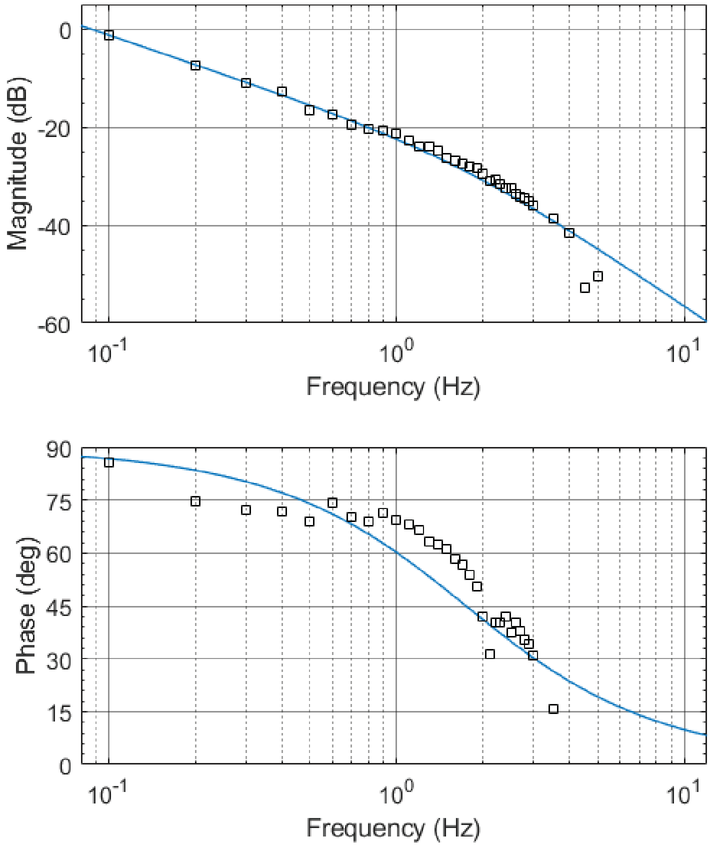

Figure 7.5: HIS actuator identification

Listing 7.1: HIS actuator model identification report

```
  From input "Speed command to motor" to output "HIS actuator
    displacement":
              -5.95
  ------------------------------
  s^2 + 10.96 s + 5.859e-11

Name: tf1
Continuous-time identified transfer function.

Parameterization:
   Number of poles: 2   Number of zeros: 0
   Number of free coefficients: 3
   Use "tfdata", "getpvec", "getcov" for parameters and their
    uncertainties.

Status:
Estimated using TFEST on frequency response data "h".
Fit to estimation data: 90.79% (stability enforced)
FPE: 0.0003111, MSE: 0.0002849
```

7.6 Active HIS Identification Experiment

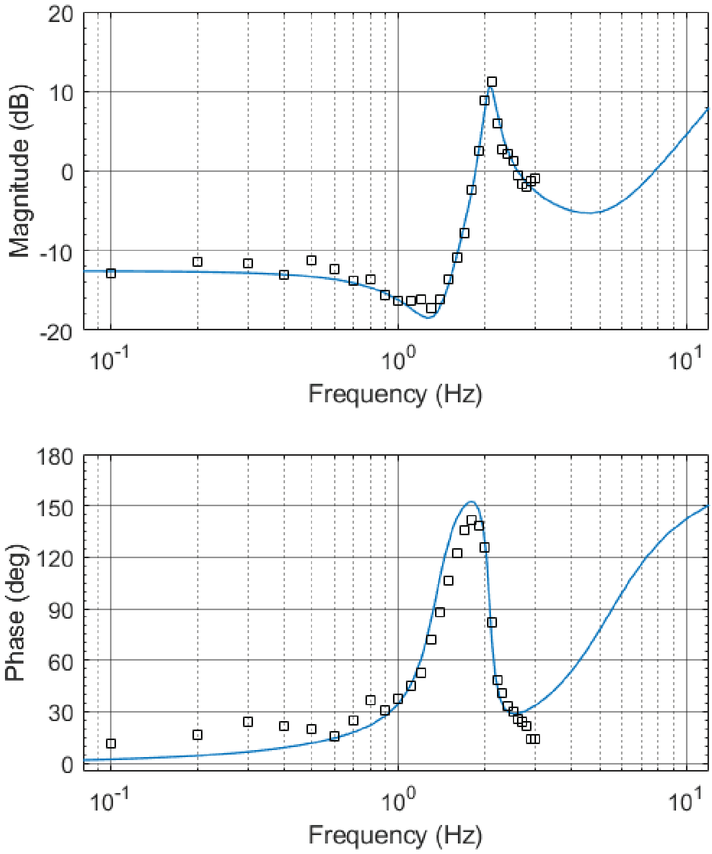

Figure 7.6: Active HIS identification

Listing 7.2: Active HIS identification report

```
 From input "HIS actuator displacement" to output "HIS differential
   pressure":
  0.0004764 s^4 + 0.01676 s^3 + 0.6295 s^2 + 2.639 s + 40.06
 ---------------------------------------------------------------
                       s^2 + 1.184 s + 169.6

Name: tf6
Continuous-time identified transfer function.

Parameterization:
   Number of poles: 2   Number of zeros: 4
   Number of free coefficients: 7
   Use "tfdata", "getpvec", "getcov" for parameters and their
    uncertainties.

Status:
Estimated using TFEST on frequency response data "h".
Fit to estimation data: 84.31% (stability enforced)
FPE: 0.03627, MSE: 0.02869
```

7.7 Half Car Rig $u \to y$ Identification Experiment

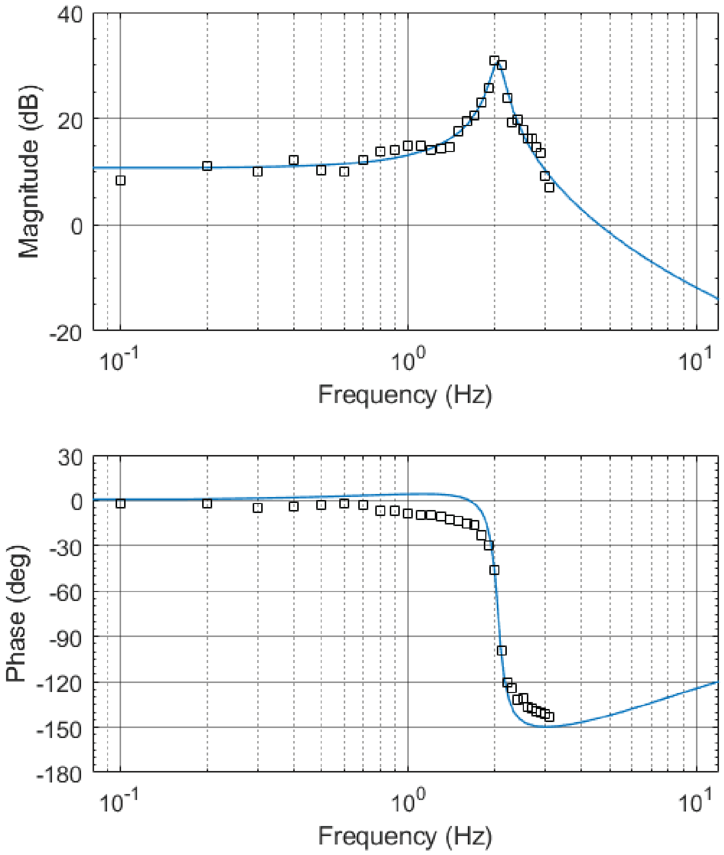

Figure 7.7: Actuator displacement to half-car roll angle identification

Listing 7.3: Actuator displacement to half-car roll angle identification report

```
 From input "Actuator displacement" to output "Roll angle":
    12.55 s + 565.8
 -----------------------
 s^2 + 1.336 s + 165.8

Name: tf1
Continuous-time identified transfer function.

Parameterization:
   Number of poles: 2   Number of zeros: 1
   Number of free coefficients: 4
   Use "tfdata", "getpvec", "getcov" for parameters and their
    uncertainties.

Status:
Estimated using TFEST on frequency response data "h".
Fit to estimation data: 81.05% (stability enforced)
FPE: 4.885, MSE: 4.293
```

7.8 Half Car Rig $w \to y$ Identification Experiment

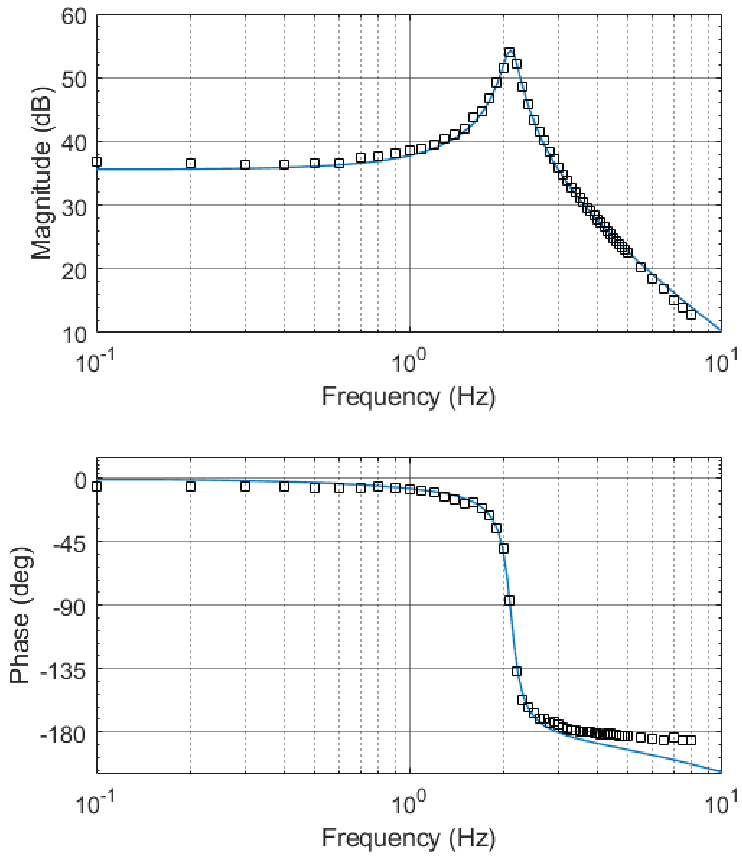

Figure 7.8: Bode diagram for roll moment disturbance to to half-car roll angle identification

Listing 7.4: Actuator displacement to half-car roll angle identification report

```
  From input "Roll moment disturbance" to output "Roll angle":
    -97.64 s + 1.063e04
  ---------------------
  s^2 + 1.547 s + 176.7

Name: tf1
Continuous-time identified transfer function.

Parameterization:
    Number of poles: 2   Number of zeros: 1
    Number of free coefficients: 4
    Use "tfdata", "getpvec", "getcov" for parameters and their
     uncertainties.

Status:
Estimated using TFEST on frequency response data "h".
Fit to estimation data: 92.26% (stability enforced)
FPE: 120.6, MSE: 112.3
```

7.9 Half Car Rig $\dot{u} \rightarrow y$ Identification Experiment

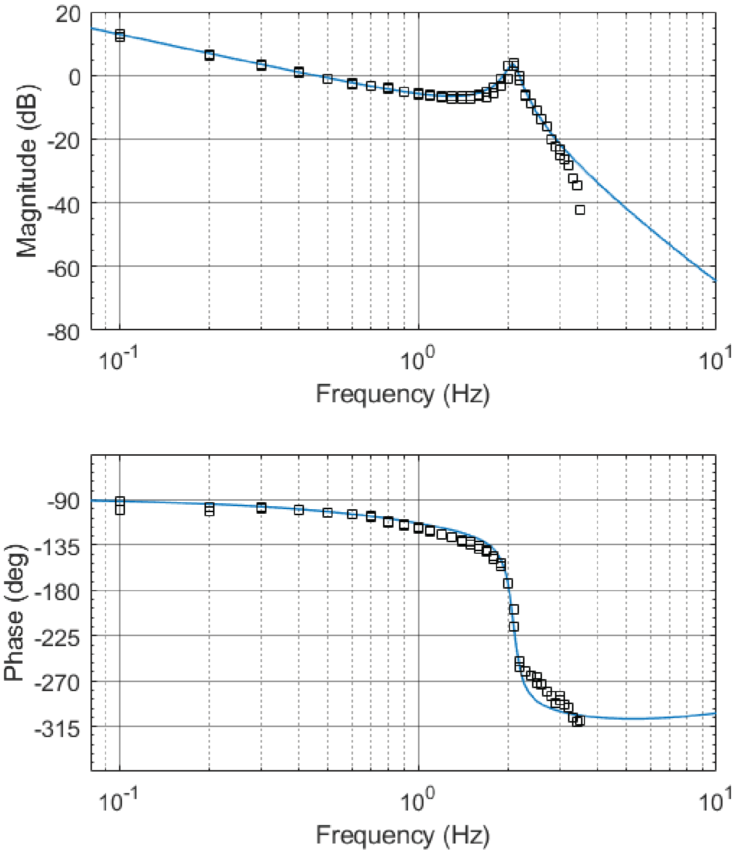

Figure 7.9: Bode diagram for motor speed command to half-car roll angle identification

Listing 7.5: Motor speed command to half-car roll angle identification report

```
  From input "Motor speed command" to output "Roll angle":
                    100.5 s + 6330
  ------------------------------------------------
  s^4 + 14.58 s^3 + 190.3 s^2 + 2280 s + 24.69

Name: tf1
Continuous-time identified transfer function.

Parameterization:
   Number of poles: 4   Number of zeros: 1
   Number of free coefficients: 6
   Use "tfdata", "getpvec", "getcov" for parameters and their
    uncertainties.

Status:
Estimated using TFEST on frequency response data "h".
Fit to estimation data: 93.06% (stability enforced)
FPE: 0.008497, MSE: 0.006739
```

Chapter 8

LQG Compensator Design

Now that we have the identified model from the motor speed command signal to the half-car roll angle, we can effectively design a controller for this very model. Unlike in [19], [1], [2] and [3], our approach to the problem of controller design is more effective as it eliminates all model uncertainties and hidden variables to the maximum extent possible. It also allows one to easily design a controller which will be valid out of the box without the necessity of blind tuning by trial and error. Moreover, this approach is guaranteed to be in tune with the physical system the controller is designed for and achieve maximum efficiency and best performance. We choose the controller to be combined of two individual parts. One is the linear quadratic regulator, and the other is the Kalman, state observer. When working together, these are equivalent to a linear quadratic Gaussian controller which is widely used in many industries from manufacturing to airspace and famous for its high reliability and robustness. Dividing the design of controller into two individual problems not only facilitates the understanding but also provides us with more flexibility in our designs.

8.1 Linear Quadratic Regulator Design

The identified transfer function of the physical model from input $\dot{u}$ to output y (see figure 7.4), is given in equation 8.1. In our codes we convert the transfer function into a state-space, see equation 8.2. For the state-space of the identified model, we design a linear quadratic regulator and obtain the LQR gain which is a vector. This vector is to be multiplied by the system's state vector yielding the required amount of control effort which stabilises the system in real time.

To design a linear quadratic regulator one needs to specify the penalty matrices that are associated with the system states, the control efforts and the cross-terms of the two. We choose the penalty for the control effort to be equal to one $R = 1$ and the cross-term penalty to be equal to zero $N = 0$. We implement two different controller settings: the moderate and the aggressive setting. Therefore we define the state-penalty matrix Q twice for each setting respectively. The moderate Q setting is given in equation 8.3 and the aggressive Q setting is given in 8.4. For simplicity, we keep all non-diagonal elements equal to zero. The diagonal values of Q matrix signify the penalties given to different system states ordered from lowest to highest. Thus, the diagonal element q_{44} specifies a penalty to the absolute deviation of the system from the desired value, which is the desired roll angle in our case. The diagonal element $q_3 3$ has a meaning of penalty assigned for the roll angle rate. The other two diagonal elements q_{22} and q_{11} of matrix Q are of minor importance and kept small. Their physical meanings are the acceleration and jerk correspondingly.

As a result, we obtain two LQR gain vectors for the moderate G_m and the aggressive G_a setting that is then used in the real-time evaluation of the control effort, see equation 8.5.

The resulting closed-loop model is characterised by the predicted step input response (figure 8.1) and pole-zero map (figure 8.2). Although, it will be seen later that the predicted responses do not exactly match the ones that are found experimentally.

$$H(s) = \frac{100.5\,s + 6330}{s^4 + 14.58\,s^3 + 2280\,s + 24.69} \tag{8.1}$$

$$A = \begin{bmatrix} -14.46 & -12.33 & -9.11 & -5.21 \cdot 10^{-11} \\ 16 & 0 & 0 & 0 \\ 0 & 16 & 0 & 0 \\ 0 & 0 & 1 & 0 \end{bmatrix}$$

$$B = [4, 0, 0, 0]^T \tag{8.2}$$

$$C = [0, 0, -0.07, -5.70]$$

$$D = 0$$

$$Q_m = \begin{bmatrix} 1 & 0 & 0 & 0 \\ 0 & 1 & 0 & 0 \\ 0 & 0 & 10^3 & 0 \\ 0 & 0 & 0 & 10^5 \end{bmatrix} \tag{8.3}$$

$$Q_a = \begin{bmatrix} 1 & 0 & 0 & 0 \\ 0 & 1 & 0 & 0 \\ 0 & 0 & 10^3 & 0 \\ 0 & 0 & 0 & 10^7 \end{bmatrix} \tag{8.4}$$

$$G_m = [11.29, 26.17, 31.95, 316.22]$$
$$G_a = [23.72, 91.81, 191.43, 3162.27] \tag{8.5}$$

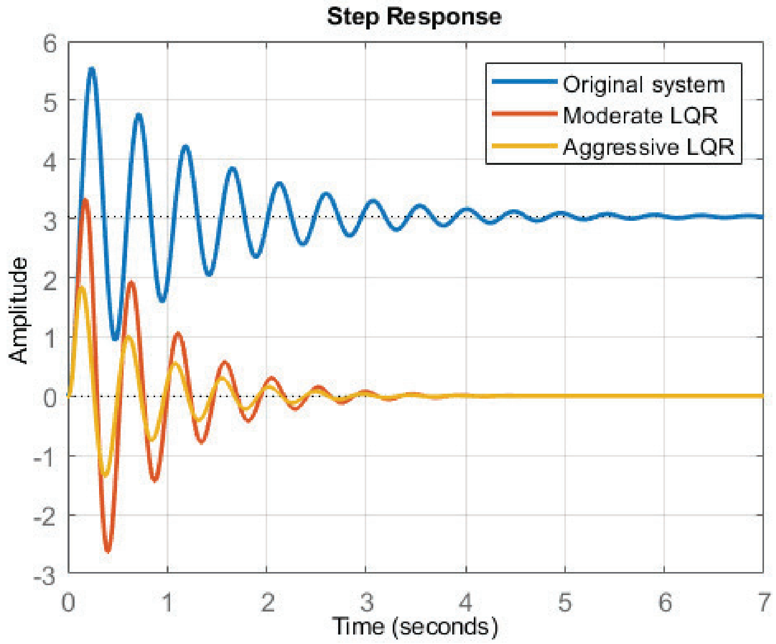

Figure 8.1: Expected step input response of the closed loop model

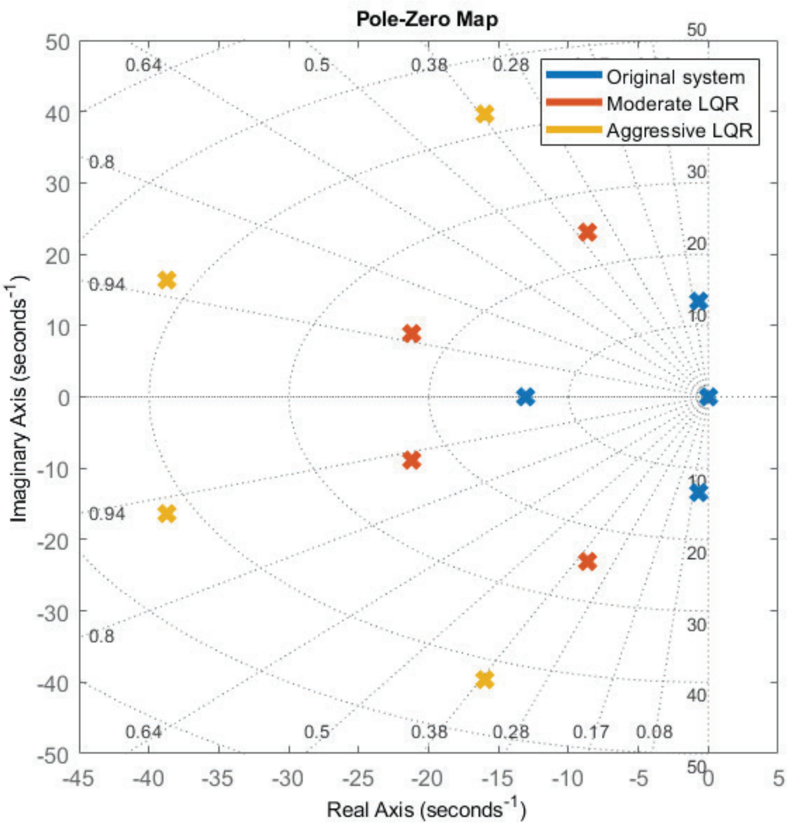

Figure 8.2: Expected pole-zero map of the closed loop model

8.2 Kalman State Observer Design

To design Kalman state observer we convert continuous time model 8.2 into a discrete time state-space as given in 8.6 with sampling rate of 1 ms. A Kalman state observer operates the information about uncertainties to operate. Therefore we specify three values of uncertainties: the uncertainty of state $Q_n = 1$, the uncertainty of measurement $R_n = 10^5$ and the state-measurement covariance uncertainty $N_n = 0$. Such choice of uncertainty values is due to the significant level of noise in the measurement signals which originates from the electromagnetic pickup of the motor parasite emissions. As discussed above the typical signal to noise ratio in the measurement signals is as small as $SNR = 30$ dB, which was also found experimentally.

$$
\begin{aligned}
A &= \begin{bmatrix} 0.9855 & -0.0123 & -0.0090 & -5.1788 \cdot 10^{-14} \\ 0.0158 & 0.9999 & -7.2607 \cdot 10^{-5} & -4.1531 \cdot 10^{-16} \\ 0.0001 & 0.0159 & 0.9999 & -2.2176 \cdot 10^{-18} \\ 4.2512 \cdot 10^{-8} & 7.9998 \cdot 10^{-6} & 0.0009 & 1 \end{bmatrix} \\
B &= [0.0039, 3.1845 \cdot 10^{-5}, 1.7004 \cdot 10^{-7}, 4.2543 \cdot 10^{-11}]^T \\
C &= [0, 0, -0.0717, -5.7055] \\
D &= 0
\end{aligned}
\tag{8.6}
$$

It should be noted that Kalman state observer itself represents another dynamic model and therefore distorts the expected simulated characteristics of the closed-loop system such as those shown in figures 8.1 and 8.2. One can find the corresponding codes for LQR design and Kalman state observer design in listing A.11. And the compensator diagram which deploys and executes physically on the micro-controller is given in figure 8.3.

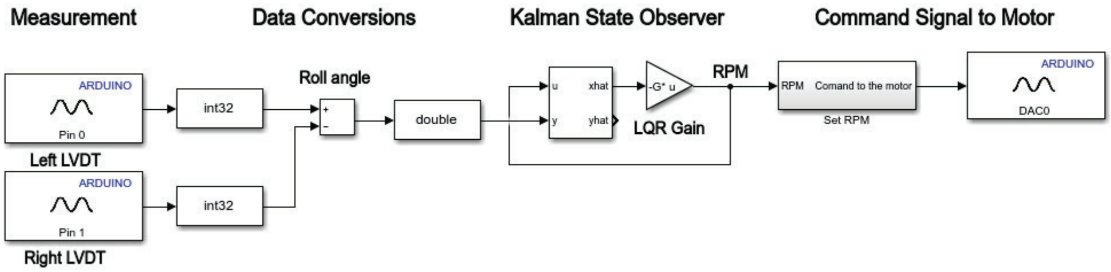

Figure 8.3: Compensator code which executes on the micro-controller

Chapter 9

Compensator Validation Experiments

We have already discussed the way of validating a compensator from the theoretical point of view in Chapter 5 - Simulation. In this chapter, we propose to perform validation of the real LQG compensator with the same idea as described in section 5.1. For reader's convenience here we paste the same figure again, see figure **??**. Figure 5.1 illustrates that in our validation experiments we are looking to measure system's response to external disturbance input in two situations: when the other input is left intact and when the LQG compensator controls the other input. The difference between these two scenarios will give us a foundation to make judgements about the compensator performance as well as the entire active hydraulically interconnected suspension ability for the roll angle reduction in real time. The most accurate way of performing this experiment is the measurement of the frequency response characteristic of the system across the range of frequencies from 0.1 Hz up to approximately 10 Hz depending on each individual system.

9.1 Prediction Power

Having made the identifications in Chapter 7, we could also efficiently predict the responses and models that would appear when the LQG compensator controls the system. The following identification graphs not only show the new models identified but also compare them with the predicted models and responses from Chapter 8. The reader will soon see and judge about the prediction power of the models identified earlier in Chapter 7. The author of the thesis does not make any conclusions at this point only for the sake of a little intrigue as the figures below are rather self-explanatory.

9.2 Agreement of the Results

In this section, the author of the thesis would like to present here his final results for readers judgement. As mentioned above, we tested the LQG compensator at two different settings: moderate and aggressive. At both settings, we collected a closed-loop response of the vehicle roll angle towards the disturbance roll moment which was induced externally. At both settings, we have collected system responses to a sine-wave excitation and processed the data in a way to obtain experimental data points for Bode diagram. The experimental data was then used to identify the new system models that we compared with the predicted ones.

One can find the Bode diagram for the moderate controller setting in figure 9.1 and the one for the aggressive controller setting in figure 9.2. In both figures, it is seen that the experimental results have excellent agreement with the predicted diagrams produced in Chapter 8.

Another experiment which was conducted is the drop-test when we lifted one side of the setup with a crane and then suddenly dropped it. In our drop tests, we recorded the readings of the roll angle and the hydraulic pressure. The experiment was repeatedly conducted tens of times, and here we present the typical results. As seen in figure 9.4 the agreement of predicted step input responses with the experimental ones is near excellent. The pressure readings are also given for reader's reference in 9.5.

High agreement of the results achieved gives us a foundation to conclude that:

- the identified models accurately characterise real physical systems,
- the identified models are valid to a high degree of confidence,

- the identified models have high prediction power,
- the identified models can be effectively used for control system design,
- the identified models can be effectively used for real-time system states estimation.

9.3 LQG Compensator Performance

The performance of the LQG compensator can be assessed by comparing the experimentally identified closed loop diagrams with the open loop system's response to the same disturbance. In figure 9.3 is shown the magnitude diagram of the models identified. As seen in the figure, the compensator effectively attenuates low-frequency excitation. However, the region of our interest lies in the resonant frequency which is approximately equal to $f_0 = 2.3$ Hz. As known from the theory, peak magnitude value achieved at resonance is also responsible for the peak response to a step input in the time domain. One can see in figure 9.3 that the attenuation of the resonant peak for moderate LQG setting is as big as approximately 4 dB or 1.6 times and the attenuation of peak response at the aggressive setting is as big as approximately 8 dB or 2.4 times. This result is also consistent with both the predicted and the measured step response of the system that is given in figure 9.4. A slight discrepancy between the frequency domain and the time domain experiments is explained by the non-linear effects such as, for example, dry friction.

As an evidence of our experimental work we also provide the tables with the experimental data B.6 and B.7 and the identification reports in listings 9.1 and 9.2.

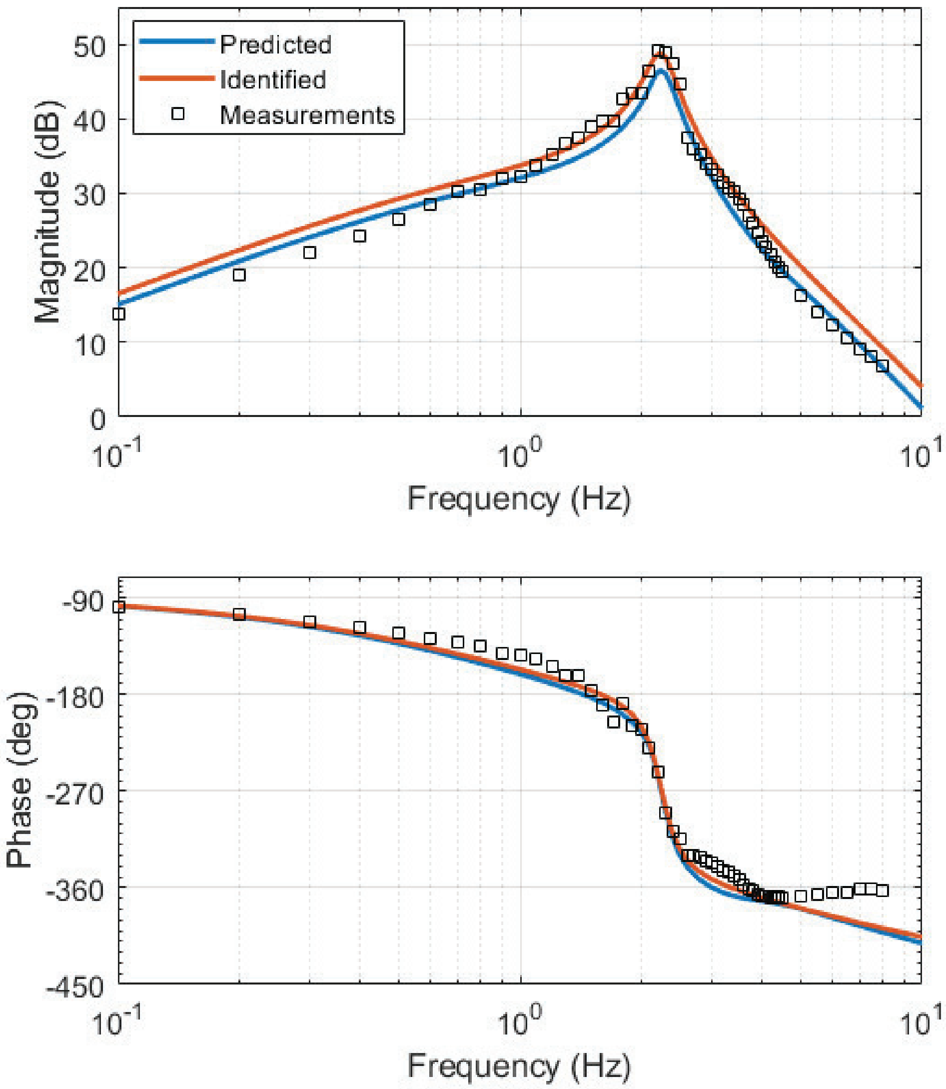

Figure 9.1: Experimental closed loop system identification from w to y when controlled with an LQG at moderate setting

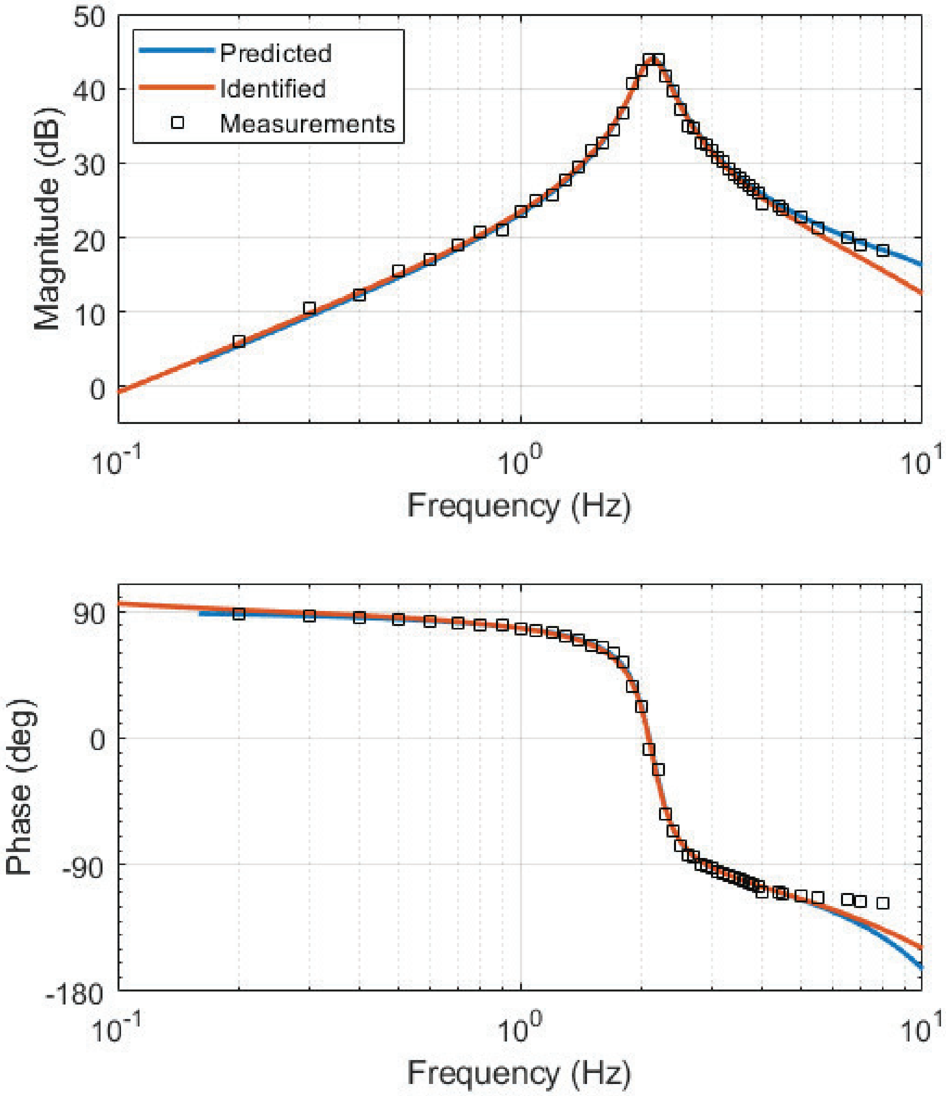

Figure 9.2: Experimental closed loop system identification from w to y when controlled with an LQG at aggressive setting

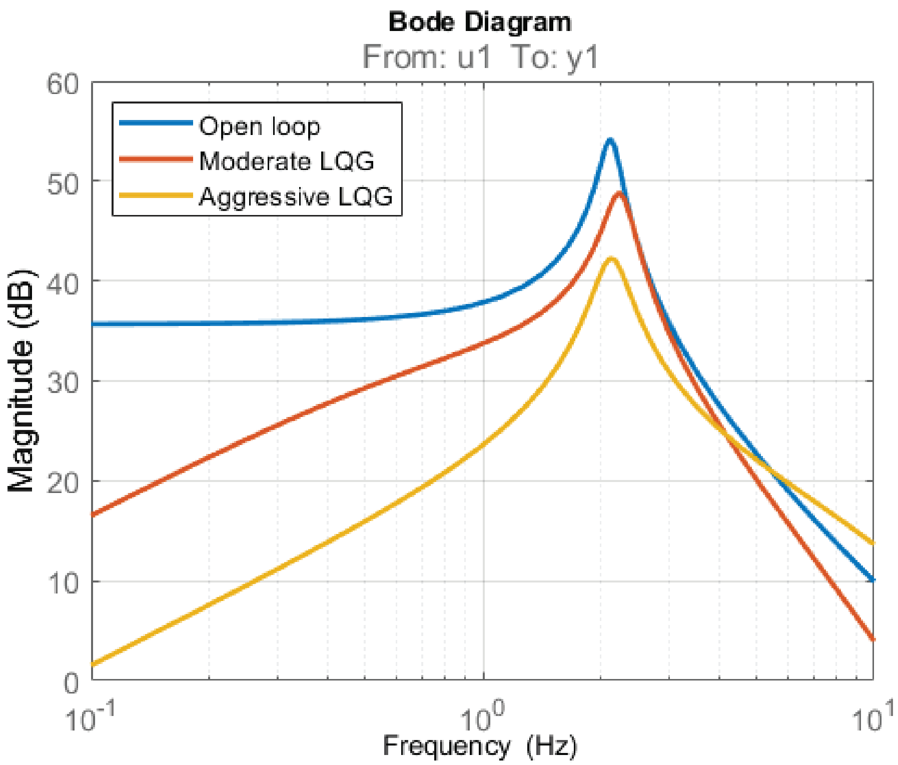

Figure 9.3: Experimental Bode diagrams compared

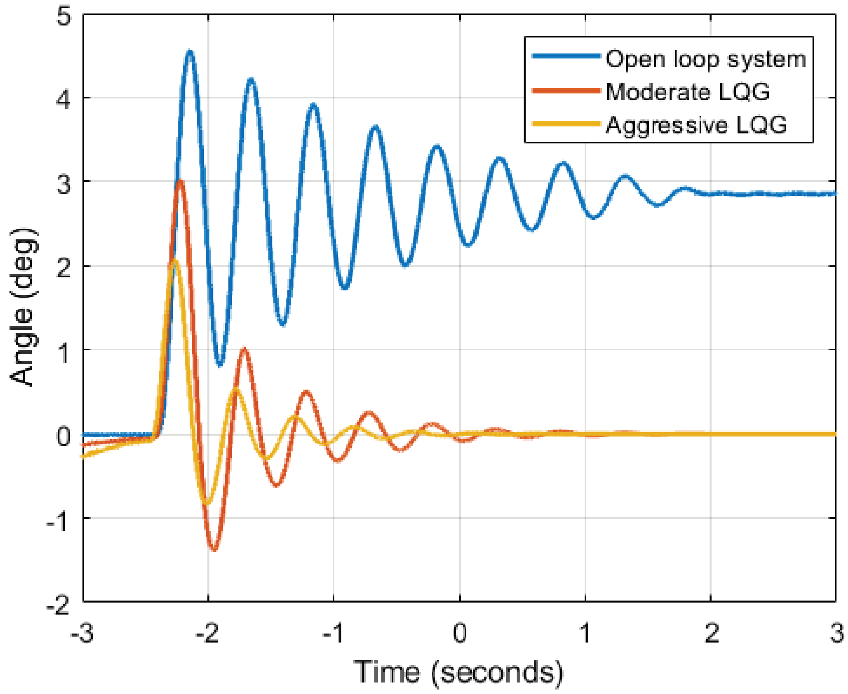

(a) Drop-test measurements

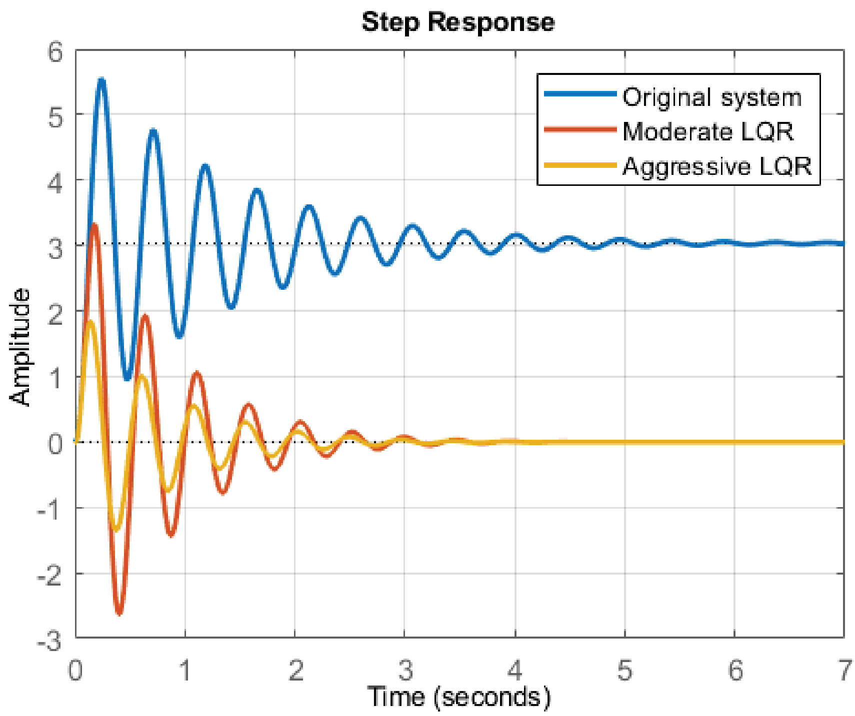

(b) Predicted step response

Figure 9.4: Drop test results compared with predicted step input response

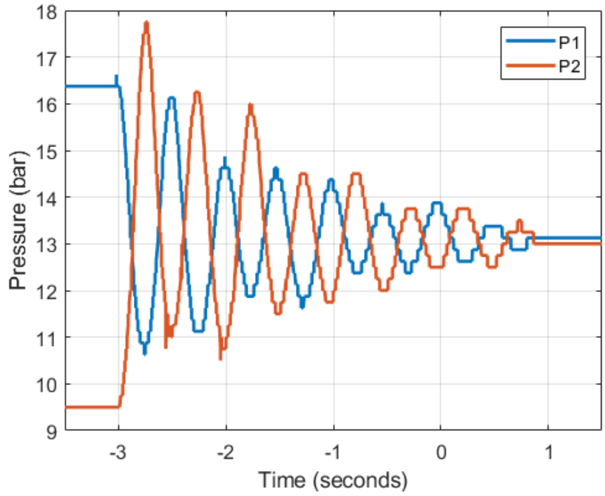

(a) Open loop system test

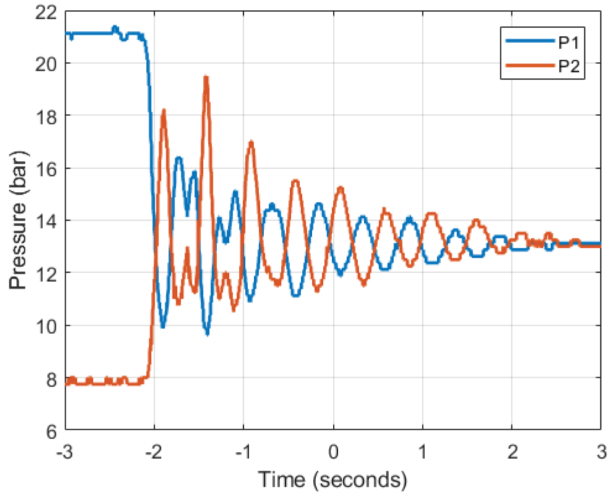

(b) Closed loop system test

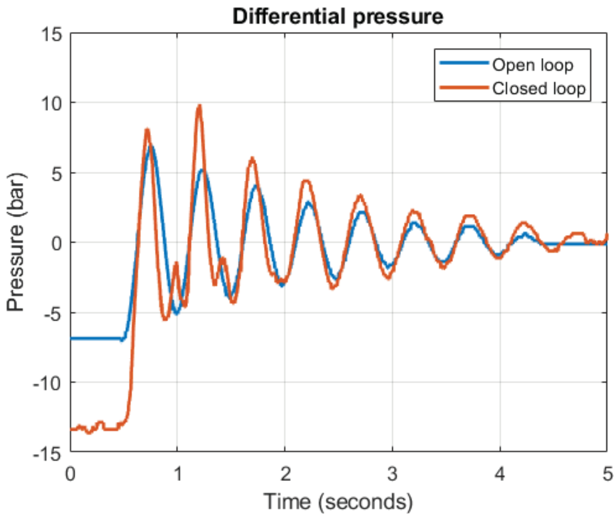

(c) Differential pressure compared between open and closed loop

Figure 9.5: Typical drop test pressure measurements

Listing 9.1: Identification report for the model from disturbance to roll angle when controlled with LQG at moderate setting

```
mod_exp =

  From input "u1" to output "y1":
                   -4.72e05 s + 8555
  ---------------------------------------------------------
  s^4 + 55.65 s^3 + 540.9 s^2 + 1.114e04 s + 4.388e04

Name: tf1
Continuous-time identified transfer function.

Parameterization:
   Number of poles: 4   Number of zeros: 1
   Number of free coefficients: 6
   Use "tfdata", "getpvec", "getcov" for parameters and their
    uncertainties.

Status:
Estimated using TFEST on frequency response data "h".
Fit to estimation data: 81.69% (stability enforced)
FPE: 305.7, MSE: 272.3
```

Listing 9.2: Identification report for the model from disturbance to roll angle when controlled with LQG at aggressive setting

```
agg_exp =

  From input "u1" to output "y1":
                2.53e06 s - 1.899e05
  --------------------------------------------------------
  s^4 + 148.6 s^3 + 9387 s^2 + 4.905e04 s + 1.586e06

Name: tf1
Continuous-time identified transfer function.

Parameterization:
   Number of poles: 4   Number of zeros: 1
   Number of free coefficients: 6
   Use "tfdata", "getpvec", "getcov" for parameters and their
    uncertainties.

Status:
Estimated using TFEST on frequency response data "h".
Fit to estimation data: 90.95% (stability enforced)
FPE: 11.42, MSE: 10.02
```

Chapter 10

Summary of Research Findings

In this project, we have done the work which was not only theoretical and simulation but in many ways practical as well. The significance of this research project is supported by the fact that in this project takes place the unification of theory, simulations, practical work and experimentation. As the reader could see throughout the thesis, these four components together form a strong combination supporting our statements and findings. The author of the thesis can tell that he feels quite satisfied with the work and the outcomes of present research. Of course, it is up to the reviewers to judge about the author's work. However, the author would like to say that he considers this project complete and successful.

To conclude this research, the author can make the following statements. In this research project

- we derived a valid augmented half-car model fitted with active hydraulically interconnected suspension;
- we took measured the parameters of the existing half-car testing rig for upgrading it later;
- we did initial estimations required for the upgrade;
- we performed numerical simulations with the models derived to predict future key parameters of the upgraded setup;
- our simulations also confirmed the feasibility of the methodology chosen;

- we designed the upgraded half-car testing rig in 3D CAD software;
- we created all necessary drafts and ordered custom parts in UTS Workshop;
- we ordered where possible existing parts from the market
- we managed the manufacturing process and upgraded the half-car testing rig;
- we did all necessary commissioning work to make the upgraded setup functional;
- we conducted identification experiments to obtain the sub-models important for the control system design;
- we designed a real LQG compensator for the system and tested it physically on the half-car rig;
- our tests have proved active hydraulically interconnected suspension system to have a high capacity for roll angle reduction;
- our tests also confirmed the validity of the LQG compensator designed;
- our experimental results have shown excellent agreement with the ones found through simulations;
- overall, we can state here that our work on this project has finished successfully.

10.1 Further Research

The author suggests to continue this research using same methodology as it was demonstrated in this thesis. Namely, precise model identification through forced vibration experiment is very important. The author suggests to also pay attention to further improvements of the half-car testing rig such as using better displacement sensors, not LVDT's, using a faster micro-controller. Note that LVDT sensors generate a lot of noise due to the electromagnetic interference which is picked up through the magnetic core of LVDT.

Further research can be done in the following directions:

- implementation of other control methods: H2, H-infinity, Sliding Mode,
- assessment of controller reaction to the uncertainties in the model,
- implementation of roll-over testing scenarios used in real car crash tests,
- developing fuzzy rules to smartly switch the control method in real time.

10.2 Author's Publications

[1] Tkachev, A. A., & Zhang, N. (2017). Active Hydraulically Interconnected Suspension. Modeling and Simulation (No. 2017-01-1561). SAE Technical Paper.

[2] Zhu, S., Xu, G., Tkachev, A., Wang, L., & Zhang, N. (2017). Comparison of the road-holding abilities of a roll-plane hydraulically interconnected suspension system and an anti-roll bar system. Proceedings of the Institution of Mechanical Engineers, Part D: Journal of Automobile Engineering, 231(11), 1540-1557.

Appendix A

Codes

Listing A.1: Half-car parameters initialisation

```
%% Copyright Anton Tkachev 2014 - 2018
% anton.a.tkachev@gmail.com
% If this code was of any help to you
% please kindly give author a credit in your paper

%% Filename 'HCM12.m'
% This script initialises the parameters of a half-car with values
% close to those of a real car.

%% Half-car parameters
is = 120;    % [kg.m2]    vehicle body moment of inertia (measured)
ms = 475;    % [kg]       vehicle body mass (measured)
mu = 35;     % [kg]       unsprung mass (from Wade Smith's thesis)
ks = 20E3;   % [N/m]      suspension spring stiffness (measured)
kt = 172E3;  % [N/m]      tire spring stiffness (measured)
cs = 240;    % [N/(m/s)]  suspension damping (measured)
ct = 1000;   % [N/(m/s)]  tire damping (estimation)
b  = 0.7;    % [m]        wheel track half width (measured)
h  = 0.5;    % [m]        center of gravity height (estimation)

%% Conventions
mp = ms/4 + is/4/b^2;
mn = ms/4 - is/4/b^2;

%% Inertia matrix
Mm = [mu,  0,  0,  0;
       0, mu,  0,  0;
       0,  0, mp, mn;
       0,  0, mn, mp];

%% Damping matrix
Cm = [cs + ct,       0, -cs,   0;
            0, cs + ct,   0, -cs;
          -cs,       0,  cs,   0;
            0,     -cs,   0,  cs];

%% Stiffness matrix
```

```
Km = [ks + kt,          0, -ks,     0;
              0, ks + kt,    0, -ks;
           -ks,          0,   ks,     0;
              0,       -ks,    0,    ks];

%% Forces matrix (multiplied by f = [f1, f2, f3]^T)
G = [-1,   0,   0;
       0,  -1,   0;
       1,   0,  -1;
       0,   1,   1];

%% Road input matrix (multiplied by w = [w1, w2]^T)
H = [kt,   0;
       0,  kt;
       0,   0;
       0,   0];

%% Road input deriv. mtx. (multiplied by w' = [w1', w2']^T)
J = [ct,   0;
       0,  ct;
       0,   0;
       0,   0];

%% Conventions
G1 = G(:,1:2); G2 = G(:,3);
```

Listing A.2: Conventional half-car model

```
%% Copyright Anton Tkachev 2014 - 2018
% anton.a.tkachev@gmail.com
% If this code was of any help to you
% please kindly give author a credit in your paper

%% Filename 'CNV12.m'
% This script initialises a MIMO state-space model of
% a conventional half-car without HIS system. The model is then
% stored in a variable named CNVSS. The system has 3 inputs
% and 4 outputs. The horizontal index of CNVSS matrix corresponds
% to the output and the vertical - to the input as follows below.

% +--------+--------+--------+--------+
% | CNVSS  |   w1   |   w2   |   f3   |
% +--------+--------+--------+--------+
% |     x1 | sys11  | sys12  | sys13  |
% +--------+--------+--------+--------+
% |     x2 | sys21  | sys22  | sys23  |
% +--------+--------+--------+--------+
% |     x3 | sys31  | sys32  | sys33  |
% +--------+--------+--------+--------+
% |     x4 | sys41  | sys42  | sys43  |
% +--------+--------+--------+--------+

%% Inputs
% u = [w1, w2, f3]^T
% w1 - left road input [m]
% w2 - right road input [m]
% f3 - equivalent roll force [N] f3 = ms*al*h/b

%% States
% x = [x1, x2, x3, x4]^T
% x1 - left  wheel vertical displacement [m]
% x2 - right wheel vertical displacement [m]
% x3 - vehicle body vertical displacement on the left [m]
% x4 - vehicle body vertical displacement on the right [m]

%% Outputs
% y = [y1, y2, y3, y4]^T
% y1 - left  wheel vertical displacement [m]
% y2 - right wheel vertical displacement [m]
% y3 - vehicle body vertical displacement [m]
% y4 - vehicle body roll angle [rad]

%% State-space conventional half-car model
% s^2*M*x + s*C*x + K*x = Gf + H*w
% J assumed to be zero for simplicity: J = 0

%% State space for conventional half-car model
A1 = [zeros(4),  eye(4);
      -Mm\Km, -Mm\Cm];

B1 = [zeros(4,3); Mm\[H,G2]];

C1 = [ 1,    0,      0,      0;  % left wheel bounce
       0,    1,      0,      0;  % right wheel bounce
```

```
        0,      0,      1/2,      1/2;  % vehicle body bounce
        0,      0,  -1/2/b,   1/2/b]; % vehicle body roll angle (rad)
C1 = [C1, zeros(4)];

D1 = zeros(4,3);

CNVSS = ss(A1,B1,C1,D1);

%% Transfer function fo conventional model
s = tf('s');
CNVTF = (s^2*Mm + s*Cm + Km)\([H,G2] + s*[J,zeros(4,1)]);
```

Listing A.3: Hydraulically interconnected suspension parameters

```
%% Copyright Anton Tkachev 2014 - 2018
% anton.a.tkachev@gmail.com
% If this code was of any help to you
% please kindly give author a credit in your paper

%% Filename 'HIS12.m'
% This script initialises the parameters of active HIS system with
% values close to those of a real system

%% Hydraulic system state equations
% p = s^2*Ih*dx + s*Rh*dx + Sh*dx

%% Inputs
% dx = [dx1, dx2, dx3]^T
% dx1 - left suspension deflection [m]
% dx2 - right suspension deflection [m]
% dx3 - hydraulic actuator displacement [m]

%% Outputs
% P = [p1, p2, p3, p4]^T
% p1 - left  cylinder upper chamber pressure [Pa]
% p2 - right cylinder upper chamber pressure [Pa]
% p3 - left  cylinder lower chamber pressure [Pa]
% p4 - right cylinder lower chamber pressure [Pa]

%% Hydraulic circuit parameters
P0 = 250E3;     % [Pa] - accumulator precharge pressure
P  = 14E5;      % [Pa] - accumulator working pressure
V0 = 0.32E-3;   % [m3] - accumulator volume
g  = 1.4;       % [-]  - specific heat ratio of N2 gas
a1 = 5.1E-4;    % [m2] - upper susp. piston area
a2 = 4.1E-4;    % [m2] - lower susp. piston area
a3 = 1.2E-3;    % [m2] - actuator piston annular area

%% Unknown parameters are estimated to the order of magnitude
r1 = 1.0E7;     % [Pa/(m3/s)] - 1st linear loss coefficient
r2 = 1.0E7;     % [Pa/(m3/s)] - 2nd linear loss coefficient
r3 = 1.0E7;     % [Pa/(m3/s)] - 3rd linear loss coefficient
ih = 1.0E4;     % [Pa/(m^3/s^2)] -  fluid inertia (omitted)

%% Pre-calculations
V = V0*P0/P;    % [m3] - gas volume in accumulator at rest
ch = V/P/g;     % [m3/Pa] - accumulator capacitance

%% Elastance matrix
Sh = 1/ch*[ a1, -a2,  a3;
           -a2,  a1, -a3;
           -a2,  a1, -a3;
            a1, -a2,  a3];

%% Resistance matrix
Rh = [      a1*(r1 + r2),             -a2*r2,         a3*r2;
                  -a2*r2,       a1*(r1 + r2),        -a3*r2;
       -a2*(r1 + r2 + r3),             a1*r2, -a3*(r2 + r3);
                   a1*r2, -a2*(r1 + r2 + r3),  a3*(r2 + r3)];

```

```
%% Inertance matrix
Ih = ih*[   0,    0,    0;
            0,    0,    0;
          -a2,    0,  -a3;
            0,  -a2,   a3];

%% Conventions
Sh1 = Sh(:,1:2); Sh2 = Sh(:,3);
Rh1 = Rh(:,1:2); Rh2 = Rh(:,3);
Ih1 = Ih(:,1:2); Ih2 = Ih(:,3);

%% HIS model in s-domain
s = tf('s');
HIS = Sh + s*Rh + s^2*Ih;
```

Listing A.4: Hydraulic-to-mechanical boundary condition

```
%% Copyright Anton Tkachev 2014 - 2018
% anton.a.tkachev@gmail.com
% If this code was of any help to you
% please kindly give author a credit in your paper

%% Filename 'H2M12.m'
% This script implements hydraulic-to-mechanical
% boundary condition and defines equivalent mechanical matrices
% to be augmented to the half-car model.

%% Hydraulic to mechanical boundary condition
P2F = [-a1,    0,   a2,    0;  % pressure to force conversion
          0, -a1,    0,   a2];

%% Equivalent mechanical matrices
Mh1 = G1*P2F*Ih1*G1';        % equivalent mechanical inertia
Ch1 = G1*P2F*Rh1*G1';        % equivalent mechanical damping
Kh1 = G1*P2F*Sh1*G1';        % equivalent mechanical stiffness

%% Equivalent reactions to actuator input
Mh2 = G1*P2F*Ih2;            % equivalent inertial reaction
Ch2 = G1*P2F*Rh2;            % equivalent damped reaction
Kh2 = G1*P2F*Sh2;            % equivalent stiff reaction
```

Listing A.5: Transfer function model initialisation

```
%% Copyright Anton Tkachev 2014 - 2018
% anton.a.tkachev@gmail.com
% If this code was of any help to you
% please kindly give author a credit in your paper

%% Filename 'MAKETF12.m'
% This script initialises a MIMO transfer function model of
% a half-car with active HIS. The model is then stored in a
% variable named SYSTF. The system has 4 inputs and 4 outputs.
% The horizontal index of SYSTF matrix corresponds to the output
% and the vertical - to the input as follows below.

% +-------+-------+-------+-------+-------+
% | SYSTF |  u1   |  u2   |  u3   |  u4   |
% +-------+-------+-------+-------+-------+
% |    y1 | tf11  | tf12  | tf13  | tf14  |
% +-------+-------+-------+-------+-------+
% |    y2 | tf21  | tf22  | tf23  | tf24  |
% +-------+-------+-------+-------+-------+
% |    y3 | tf31  | tf32  | tf33  | tf34  |
% +-------+-------+-------+-------+-------+
% |    y4 | tf41  | tf42  | tf43  | tf44  |
% +-------+-------+-------+-------+-------+

%% Inputs
% u = [u1, u2, u3, u4]^T
% u1 - left road input [m]
% u2 - right road input [m]
% u3 - equivalent roll force [N]
% u4 - hydraulic actuator displacement [m]

%% Outputs
% y = [y1, y2, y3, y4]^T
% y1 - left  wheel vertical displacement [m]
% y2 - right wheel vertical displacement [m]
% y3 - vehicle body vertical displacement on the left  [m]
% y4 - vehicle body vertical displacement on the right [m]

%% Numerator coefficient matrices
R0 = [H,G2,Kh2];
R1 = [J,zeros(4,1),Ch2];
R2 = [zeros(4,3),Mh2];

%% Initialise s-variable
s = tf('s');

%% Numerator of the TF
NUM = (R0 + R1*s + R2*s^2);

%% Denominator of the TF
DEN = (Mm - Mh1)*s^2 + (Cm - Ch1)*s + (Km - Kh1);

%% Transfer function matrix (4x4)
SYSTF = DEN\NUM;
```

Listing A.6: State-space model initialisation

```
%% Copyright Anton Tkachev 2014 - 2018
% anton.a.tkachev@gmail.com
% If this code was of any help to you
% please kindly give author a credit in your paper

%% Filename 'MAKESS12.m'
% This script initialises a MIMO state-space model of
% a half-car with active HIS. The model is then stored in a
% variable named SYSSS. The system has 4 inputs and 4 outputs.
% The horizontal index of SYSSS matrix corresponds to the output
% and the vertical - to the input as follows below.

% +---------+---------+---------+---------+---------+
% | SYSSS   |   u1    |   u2    |   u3    |   u4    |
% +---------+---------+---------+---------+---------+
% |      x1 | sys11   | sys12   | sys13   | sys14   |
% +---------+---------+---------+---------+---------+
% |      x2 | sys21   | sys22   | sys23   | sys24   |
% +---------+---------+---------+---------+---------+
% |      x3 | sys31   | sys32   | sys33   | sys34   |
% +---------+---------+---------+---------+---------+
% |      x4 | sys41   | sys42   | sys43   | sys44   |
% +---------+---------+---------+---------+---------+

%% State-space model limitations
% State space model does not include any derivatives of the input.
% Thus the right side of the equations of motion does not contain
% the terms (s*B1*u) and (s^2*B2*u).
% Instead, it only has (B0*u) term which allowes us to formalize
% the state space in a simple way preserving
% the physical meanings of system states

%% Equations of motion
% Mx" + Cx' + Kx = Bu

%% Resulting state-space
% x' = Ax + Bu
% y  = Cx + D

%% Inputs
% u = [u1, u2, u3, u4]^T
% u1 - left road input [m]
% u2 - right road input [m]
% u3 - lateral acceleration [m/s2]
% u4 - hydraulic actuator displacement [m]

%% States
% x = [x1, x2, x3, x4]^T
% x1 - left  wheel vertical displacement [m]
% x2 - right wheel vertical displacement [m]
% x3 - vehicle body vertical displacement on the left  [m]
% x4 - vehicle body vertical displacement on the right [m]

%% Outputs
% y = [y1, y2, y3, y4]^T
% y1 - left susp. deflection [m]
```

```
% y2 - right susp. deflection [m]
% y3 - vehicle body bounce [m]
% y4 - vehicle body roll angle [rad]

%% Combining half-car and HIS models into a state-space
A2 = [                 zeros(4),                    eye(4);
       -(Mm - Mh1)\(Km - Kh1), -(Mm - Mh1)\(Cm - Ch1)];

B2 = [zeros(4); (Mm - Mh1)\[H,G2,Kh2]];

C2 = [-1,     0,      1,      0;  % [m]   left susp. deflection
       0,    -1,      0,      1;  % [m]   right susp. deflection
       0,     0,    1/2,    1/2;  % [m]   vehicle body bounce
       0,     0, -1/2/b,  1/2/b]; % [rad] vehicle body roll angle

C2 = [C2,zeros(4)];

D2 = zeros(4);

SYSSS = ss(A2,B2,C2,D2);
```

Listing A.7: Linear quadratic regulator design

```
%% Copyright Anton Tkachev 2014 - 2018
% anton.a.tkachev@gmail.com
% If this code was of any help to you
% please kindly give author a credit in your paper

%% Filename 'SFDBCK12.m'
% This script designs an LQR control system for the submodel
% provided. It begins with model truncation which is done for
% simplicity. Then, state-feedback gains vector is found via LQR
% method. Alternatively, one can uncomment line number 30 to
% directly locate the poles of closed loop system. The gains are
% assigned to variable K. Luenberger state observer is designed
% and stored in variable OBS.

%% Reduce subsystem order to 2
SYSR = reduce(SYSSS(4,4),2,'Algorithm','balance');
% System order is reduced to 2 using balanced truncation method

%% Conventions
A = SYSR.a;
B = SYSR.b;
C = SYSR.c;

%% Linear Quadratic Regulator
q11 = 1;   % assign lower  penalty for error derivative
q22 = 10;  % assign higher penalty for absolute error

Q = blkdiag(q11,q22);          % state penalties
R = 0.01;                      % control effort penalty
N = [0;0];                     % cross penalties (no matter)
K = lqr(SYSR,Q,R,N);           % LQR gains vector

% K = place(A,B,[-30,-31]);    % alternative pole-placement

%% Closed loop system
CLSYS = ss(A - B*K, B, C, 0);

%% Luenberger state observer
L = place(A',C',[-200,-201])';       % observer feedback gains
OBS = ss(A-L*C-B*K,L,eye(2),0);      % Luenberger observer
```

Listing A.8: Entire model initialisation call sequence

```
%% Copyright Anton Tkachev 2014 - 2018
% anton.a.tkachev@gmail.com
% If this code was of any help to you
% please kindly give author a credit in your paper

%% Filename 'INIT12.m'
% This script defines the appropriate sequence of scripts
% one needs to call in order to fully initialize half-car model
% with active HIS system driven by an LQR controller

clear;      % clear workspace
HCM12;      % initialize half-car model parameters
CNV12;      % initialize conventional half-car model
HIS12;      % initialize HIS model parameters
H2M12;      % initialize hyd-to-mech boundary condition
MAKESS12;   % initialize state-space model
MAKETF12;   % initialize transfer function model
SFDBCK12;   % design an LQR controller and state observer
AHIS12;     % open Simulink diagram
```

Listing A.9: C++ implementation of PID controller in velocity form

```
#include <TimerOne.h>
#include "ArduinoTrueDAC.h"

// Elliptic Low Pass Filter
/*   n = 2;           % filter order
 *   Rp = 0.1;        % passband peak to peak ripple, dB
 *   Rs = 1000;       % stopband attenuation, dB
 *   fn = 1000;       % Nyquist frequency, Hz
 *   fc = 1;          % cutoff frequency, Hz
 *   Wp = fc/fn;      % normalized cutoff frequency */

// Sampling time
double t = 100E-6;     // 100 microseconds
double T = 100;         // 100 microseconds

// PID coefficients
double Kd = 0.1;
double Kp = 1;
double Ki = 10;

// Filter coefficients
double a[3] = {1, -1.99254216118629, 0.992574747774901};
double b[3] = {8.05339325492860e-06, 1.61067865098572e-05,
    8.05339325492859e-06};

// Filter variables
double u[3] = {0};  // input of the filter
double y[3] = {0};  // output of the filter

void setup() {
  DAC12INIT(); // initialise DAC
  Timer1.initialize(T);     // initialise timer interrupt
  Timer1.attachInterrupt(timerISR);
}

void loop(){} // empty loop

void timerISR(){ // timer interrupt service routine
   u[0] = (analogRead(A0) - analogRead(A1));    // measurement
   y[0] = -a[1]*y[1] - a[2]*y[2] + b[0]*u[0] + b[1]*u[1] + b[2]*u[2];
    // filtering

   // Derivative 1 and 2
   dy = (y[0] - y[1])/T;
   d2y = (y[0] - 2*y[1] + y[2])/T/T;

   u[2] = u[1]; u[1] = u[0];   // shift register for the input
   y[2] = y[1]; y[1] = y[0];   // shift register for the output

   w = Ki*y[0] + Kp*dy + Kd*d2y;    // PID output signal: motor speed
   DAC12(w);                          // set DAC value to w
}
```

Listing A.10: Fourier analysis using Matlab

```
%% Copyright Anton Tkachev 2014 - 2018
% anton.a.tkachev@gmail.com
% If this code was of any help to you
% please kindly give author a credit in your paper

% This code will process a waveform stored in a CSV file
% and find the magnitude and phase of the strongest
% spectral component

%% Before running this script
% one needs to run the line
% fileID = fopen('output.csv','w');
% to creat a file for the output.

%% Body of the script
filename = 'scope_xx.csv';   % provide waveform filename here

% Parse waveform data from a CSV file
waveform = importdata(filename,',',2);

t = waveform.data(:,1); % assign time
r = waveform.data(:,2); % assign reference
u = waveform.data(:,4); % assign input
y = waveform.data(:,5); % assign output

R = fft(r);     % find FFT of the reference
U = fft(u);     % find FFT of the input
Y = fft(y);     % find FFT of the output

N = length(R);      % find length of R
T = t(2) - t(1);    % find sampling time

Rm = abs(R);  % find magnitude of the reference
Um = abs(U);  % find magnitude of the input
Ym = abs(Y);  % find magnitude of the output

% Find the harmonic of excitation
[~, k] = max(Rm(2:N/2));

W = Y(k+1)/U(k+1);  % find Bode complex amplitude

% Bode plot parameters
frq = k/N/T;                % frequency (Hz)
mag = 20*log10(abs(W)); % magnitude (dB)
phs = 180/pi*angle(W);  % phase (deg)

% Append results to the output file
fprintf(fileID,'%4.4f,%4.4f,%4.4f\n',frq,mag,phs);

%% After every run
% one can change the waveform filename and run the script
% again for a different waveform. Repeat as many times as needed.
% The resutls will be appended to the output file.
% After all waveforms have been processed
% one needs to run the following line to close the output file.
% fclose(fileID);
```

Listing A.11: LQR and Kalman state observer design

```
%% Copyright Anton Tkachev 2014 - 2018
% anton.a.tkachev@gmail.com
% If this code was of any help to you
% please kindly give author a credit in your paper

% This code designs an LQR compensator and a Kalman
% state observer for the model stored in variable 'sys'.
% The closed loop system models are saved in variables
% clsys1 and clsys2

%% System state-space matrices
A = sys.a;
B = sys.b;
C = sys.c;
D = sys.d;

%% Kalman state observer design
Qn = 1;     % uncertainty of state
Rn = 1E5;   % uncertainty of measurement
Nn = 0;     % process-measurement cross-covariance

%% LQR moderate setting
Q = blkdiag(1,1,1E3,1E5);   % Penalty for states: position and velocity
R = 1;                      % Penalty for control effort
N = 0;                      % State-control-effort cross-term penalty
G1 = lqr(sys,Q,R,N);        % LQR gain

%% LQR aggressive setting
Q = blkdiag(1,1,1E3,1E7);   % Penalty for states: position and velocity
R = 1;                      % Penalty for control effort
N = 0;                      % State-control-effort cross-term penalty
G2 = lqr(sys,Q,R,N);        % LQR gain

%% Closed loop models
clsys1 = ss(A - B*G1, B, C, 0); % moderate setting
clsys2 = ss(A - B*G2, B, C, 0); % aggressive setting
```

Appendix B

Tables of Measurements

Table B.1: Experimental data for HIS actuator identification

Frequency	**Magnitude**	**Phase**
Hz	**dB**	**deg**
0.1	-1.2	85.8
0.2	-7.6	74.6
0.3	-11.0	72.3
0.4	-12.7	71.7
0.5	-16.5	68.9
0.6	-17.5	74.4
0.7	-19.5	70.0
0.8	-20.6	69.0
0.9	-20.8	71.5
1.0	-21.4	69.2
1.1	-22.7	68.1
1.2	-23.9	66.4
1.3	-23.9	63.2
1.4	-24.9	62.6
1.5	-26.2	61.1
1.6	-27.0	58.5
1.7	-27.4	56.6
1.8	-28.0	53.6
1.9	-28.2	50.4
2.0	-29.4	41.9
2.1	-31.1	31.2
2.2	-30.8	40.4
2.3	-31.6	40.1
2.4	-32.5	42.0
2.5	-32.5	37.4
2.6	-33.6	40.1
2.7	-34.2	37.9
2.8	-34.5	35.5
2.9	-35.1	34.2
3.0	-36.0	30.7
3.5	-38.8	15.9
4.0	-41.6	-8.9
4.5	-52.8	-37.6
5.0	-50.5	-60.3

Table B.2: Experimental data for active HIS identification

Frequency	**Magnitude**	**Phase**
Hz	**dB**	**deg**
0.1	-12.8	11.6
0.2	-11.5	16.8
0.3	-11.6	23.6
0.4	-13.1	21.6
0.5	-11.1	19.5
0.6	-12.2	15.8
0.7	-13.7	24.7
0.8	-13.7	36.8
0.9	-15.5	30.4
1.0	-16.3	37.3
1.1	-16.2	44.8
1.2	-16.0	52.8
1.3	-17.1	71.9
1.4	-16.1	88.2
1.5	-13.7	106.1
1.6	-10.8	122.5
1.7	-7.7	135.6
1.8	-2.4	141.8
1.9	2.6	138.6
2.0	8.8	125.9
2.1	11.3	82.1
2.2	5.9	48.6
2.3	2.8	40.6
2.4	2.1	32.9
2.5	1.3	30.2
2.6	-0.6	25.8
2.7	-1.6	24.3
2.8	-2.0	21.2
2.9	-1.3	13.9
3.0	-0.9	14.2

Table B.3: Experimental data for actuator displacement to half-car roll angle identification

Frequency	**Magnitude**	**Phase**
Hz	**dB**	**deg**
0.1	8.5	-1.8
0.2	11.0	-2.1
0.3	9.9	-4.4
0.4	12.0	-4.0
0.5	10.3	-3.3
0.6	10.0	-2.4
0.7	12.1	-3.0
0.8	13.9	-6.6
0.9	14.1	-7.1
1.0	14.8	-8.7
1.1	15.0	-9.4
1.2	14.1	-10.0
1.3	14.2	-10.8
1.4	14.7	-12.0
1.5	17.7	-13.8
1.6	19.6	-15.4
1.7	20.6	-16.2
1.8	23.0	-22.9
1.9	25.8	-29.3
2.0	30.8	-45.5
2.1	30.1	-99.5
2.2	23.8	-120.7
2.3	19.1	-124.0
2.4	19.6	-131.6
2.5	17.9	-131.2
2.6	16.1	-136.1
2.7	16.2	-137.6
2.8	14.7	-139.7
2.9	13.5	-140.3
3.0	9.2	-141.6
3.1	7.0	-142.9

Table B.4: Experimental data for roll moment disturbance to half-car roll angle identification

Frequency	Magnitude	Phase	Frequency	Magnitude	Phase
Hz	dB	deg	Hz	dB	deg
0.1	36.8	-5.8	2.9	37.3	-173.1
0.2	36.5	-5.9	3.0	35.9	-174.7
0.3	36.4	-6.0	3.1	34.7	-176.9
0.4	36.4	-6.3	3.2	33.8	-178.1
0.5	36.5	-6.5	3.3	32.8	-178.4
0.6	36.7	-7.3	3.4	32.0	-179.3
0.7	37.5	-7.4	3.5	31.2	-179.4
0.8	37.8	-6.3	3.6	30.4	-179.5
0.9	38.1	-7.0	3.7	29.7	-179.8
1.0	38.5	-8.0	3.8	29.0	-180.3
1.1	38.8	-8.9	3.9	28.4	-180.6
1.2	39.5	-10.1	4.0	27.8	-180.8
1.3	40.3	-13.3	4.1	27.2	-181.4
1.4	41.1	-14.8	4.2	26.6	-181.4
1.5	42.0	-17.8	4.3	25.9	-181.2
1.6	43.8	-17.4	4.4	25.5	-181.2
1.7	44.8	-21.1	4.5	24.9	-181.8
1.8	46.9	-26.1	4.6	24.3	-182.1
1.9	49.3	-35.5	4.7	23.8	-182.4
2.0	51.6	-49.9	4.8	23.4	-182.5
2.1	54.0	-86.8	4.9	22.9	-182.6
2.2	52.2	-137.2	5.0	22.4	-183.1
2.3	48.6	-157.4	5.5	20.3	-183.7
2.4	45.8	-162.6	6.0	18.5	-184.9
2.5	43.5	-166.9	6.5	16.9	-186.1
2.6	41.6	-170.6	7.0	15.2	-184.4
2.7	40.1	-171.0	7.5	13.9	-185.5
2.8	38.5	-173.5	8.0	12.8	-186.2

Table B.5: Experimental data for motor speed command to half-car roll angle identification

Frequency	**Magnitude**	**Phase**	**Frequency**	**Magnitude**	**Phase**
Hz	**dB**	**deg**	**Hz**	**dB**	**deg**
0.1	4.40	-91.1	1.6	0.46	-138.3
0.1	3.94	-99.7	1.7	0.56	-140.0
0.2	2.20	-96.6	1.7	0.45	-141.5
0.2	2.03	-100.9	1.8	0.66	-148.1
0.3	1.51	-97.3	1.8	0.54	-146.3
0.3	1.44	-98.6	1.9	0.90	-156.6
0.4	1.12	-99.8	1.9	0.69	-152.4
0.4	1.12	-99.8	2.0	1.43	-173.3
0.5	0.90	-102.9	2.0	0.88	-173.2
0.5	0.89	-103.0	2.1	1.57	-215.6
0.6	0.75	-104.6	2.1	1.41	-199.1
0.6	0.72	-104.7	2.2	0.85	-255.7
0.7	0.70	-106.6	2.2	0.98	-250.2
0.7	0.67	-108.0	2.3	0.49	-260.2
0.8	0.66	-112.0	2.3	0.48	-260.8
0.8	0.63	-112.8	2.4	0.37	-265.4
0.9	0.57	-114.9	2.4	0.37	-265.0
0.9	0.56	-116.3	2.5	0.28	-266.2
1.0	0.53	-116.9	2.5	0.28	-271.6
1.0	0.51	-119.0	2.6	0.20	-272.9
1.1	0.51	-120.3	2.7	0.16	-280.1
1.1	0.48	-121.9	2.8	0.10	-284.7
1.2	0.48	-124.1	2.9	0.08	-291.6
1.2	0.45	-125.0	3.0	0.07	-284.8
1.3	0.47	-126.9	3.0	0.06	-289.3
1.3	0.43	-127.6	3.1	0.05	-293.7
1.4	0.47	-129.9	3.2	0.04	-295.8
1.4	0.43	-131.2	3.3	0.02	-305.8
1.5	0.48	-132.2	3.4	0.02	-310.0
1.5	0.42	-133.8	3.5	0.01	-309.2
1.6	0.51	-136.2			

Table B.6: Experimental data for system identification from disturbance to roll angle when controlled with LQG at moderate setting

Frequency	**Magnitude**	**Phase**	**Frequency**	**Magnitude**	**Phase**
Hz	**dB**	**deg**	**Hz**	**dB**	**deg**
0.1	13.7	-98.5	2.7	35.9	-330.4
0.2	19.1	-105.6	2.8	35.1	-332.1
0.3	21.9	-112.0	2.9	33.9	-335.5
0.4	24.2	-118.3	3.0	33.2	-337.4
0.5	26.4	-122.6	3.1	32.5	-339.5
0.6	28.6	-128.3	3.2	31.5	-343.7
0.7	30.3	-132.0	3.3	30.7	-346.3
0.8	30.6	-135.4	3.4	30.2	-348.3
0.9	31.9	-141.5	3.5	29.2	-352.1
1.0	32.3	-142.5	3.6	28.5	-356.9
1.1	33.7	-146.9	3.7	27.1	-361.5
1.2	35.3	-153.5	3.8	25.9	-363.0
1.3	36.7	-163.0	3.9	24.8	-366.4
1.4	37.4	-161.9	4.0	23.6	-367.1
1.5	39.0	-175.7	4.1	22.7	-368.1
1.6	39.7	-189.3	4.2	21.8	-368.8
1.7	39.8	-206.2	4.3	20.8	-368.6
1.8	42.8	-189.0	4.4	20.1	-368.4
1.9	43.3	-208.9	4.5	19.4	-369.0
2.0	43.4	-213.2	5.0	16.3	-367.5
2.1	46.3	-230.4	5.5	14.1	-365.6
2.2	49.1	-251.5	6.0	12.3	-364.9
2.3	48.8	-290.6	6.5	10.6	-364.5
2.4	47.4	-306.9	7.0	9.0	-361.8
2.5	44.7	-314.4	7.5	8.1	-360.8
2.6	37.4	-330.5	8.0	6.9	-362.4

Table B.7: Experimental data for system identification from disturbance to roll angle when controlled with LQG at aggressive setting

Frequency	**Magnitude**	**Phase**	**Frequency**	**Magnitude**	**Phase**
Hz	**dB**	**deg**	**Hz**	**dB**	**deg**
0.2	6.1	87.8	2.5	37.3	-76.2
0.3	10.7	86.4	2.6	35.0	-83.6
0.4	12.2	85.8	2.7	34.7	-84.7
0.5	15.4	84.2	2.8	32.8	-89.6
0.6	17.2	83.2	2.9	32.3	-90.6
0.7	18.9	81.9	3.0	31.8	-92.3
0.8	20.9	80.3	3.1	30.6	-94.7
0.9	21.1	79.8	3.2	30.1	-95.7
1.0	23.4	77.8	3.3	29.2	-97.1
1.1	25.1	76.0	3.4	28.5	-99.5
1.2	25.7	75.1	3.5	28.1	-100.5
1.3	27.7	72.4	3.6	27.5	-101.5
1.4	29.4	69.9	3.7	26.8	-103.0
1.5	31.6	66.0	3.8	26.5	-104.0
1.6	32.7	63.9	3.9	26.0	-105.4
1.7	34.3	60.0	4.0	24.4	-109.4
1.8	36.6	53.5	4.4	24.3	-109.8
1.9	40.6	36.5	4.5	23.8	-111.4
2.0	42.4	22.9	5.0	22.7	-112.3
2.1	44.0	-8.1	5.5	21.1	-113.7
2.2	43.9	-22.1	6.5	20.0	-114.3
2.3	41.7	-53.9	7.0	19.0	-115.7
2.4	39.6	-66.5	8.0	18.3	-116.9

Appendix C

Mechanical Drawings

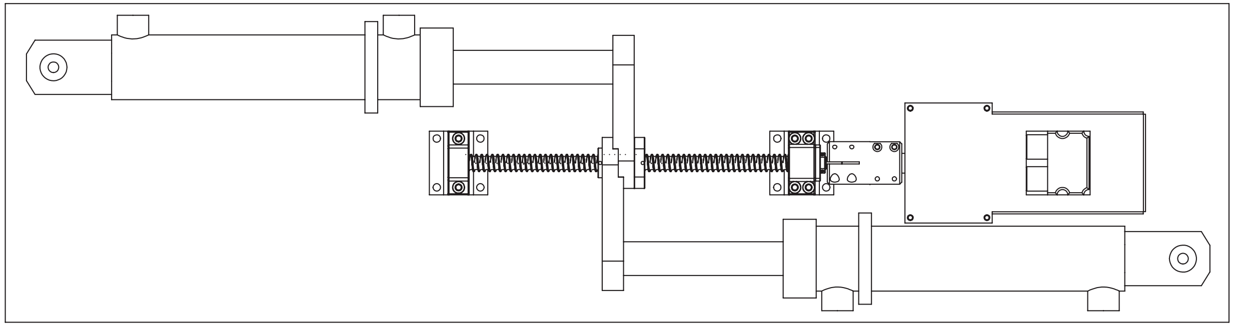

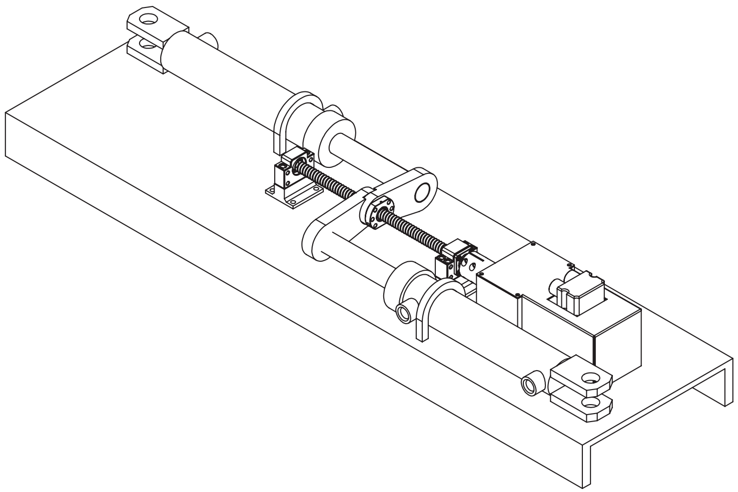

UNLESS OTHERWISE SPECIFIED: DIMENSIONS ARE IN MILLIMETERS SURFACE FINISH: TOLERANCES: LINEAR: ANGULAR:	FINISH:	DEBUR AND BREAK SHARP EDGES	DO NOT SCALE DRAWING	REVISION		
			Anton Tkachev			
	NAME	SIGNATURE	DATE		TITLE:	
DRAWN					Active HIS Actuator	
CHK'D						
APPV'D						
MFG						
Q.A				MATERIAL:	DWG NO. Assembly	A3
				WEIGHT:	SCALE:1:10	SHEET 1 OF 1

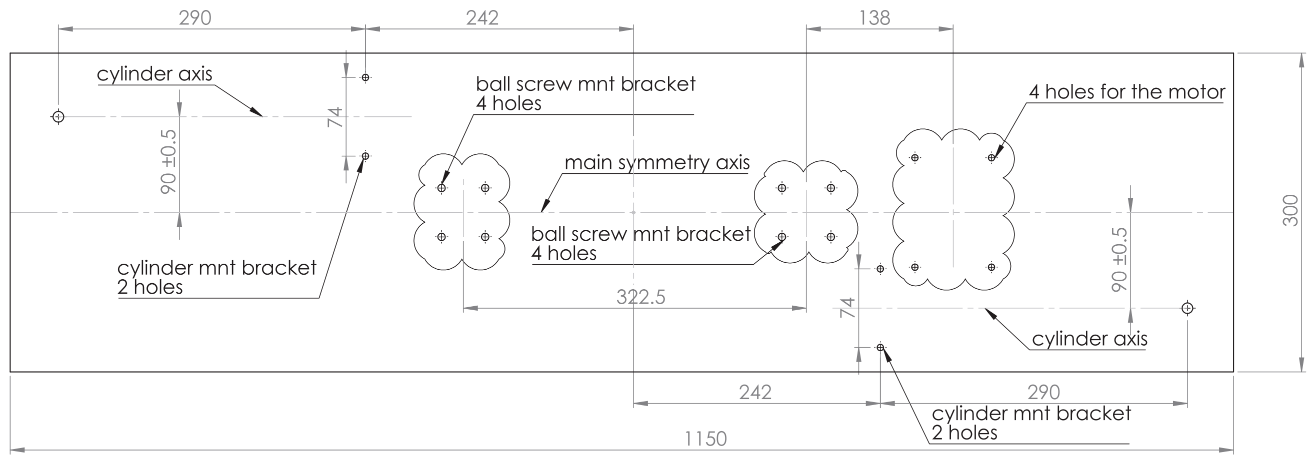

Dimensions to match parts provided

UNLESS OTHERWISE SPECIFIED: DIMENSIONS ARE IN MILLIMETERS SURFACE FINISH: TOLERANCES: LINEAR: ANGULAR:	FINISH:		DEBUR AND BREAK SHARP EDGES	DO NOT SCALE DRAWING	REVISION
				Anton Tkachev	
	NAME	SIGNATURE	DATE	TITLE:	
DRAWN				Actuator Base Channel	
CHK'D					
APPV'D					
MFG					
Q.A			MATERIAL: Steel	DWG NO. prt_channel	A3
			WEIGHT:	SCALE:1:10	SHEET 1 OF 1

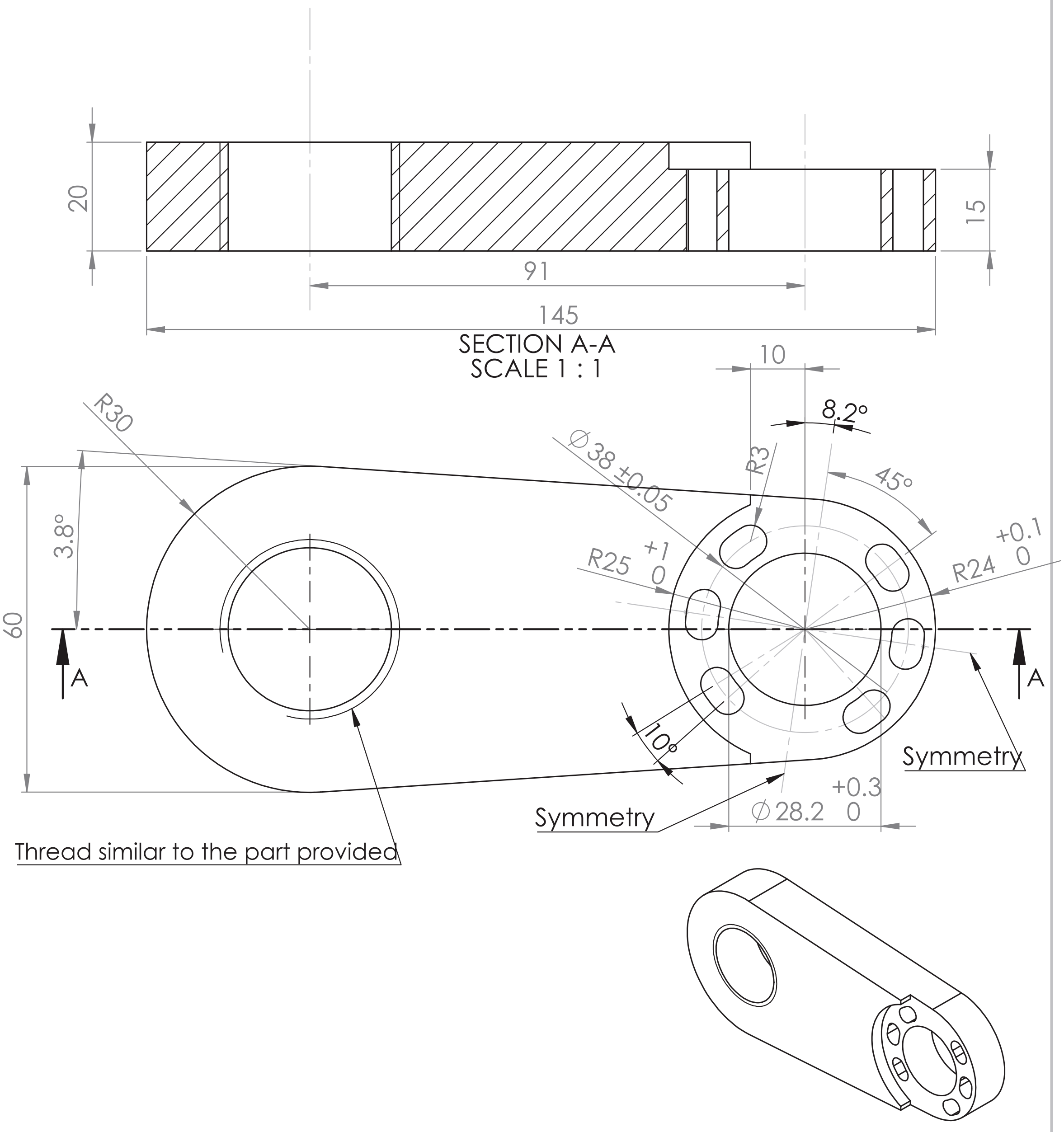

Qty: 2 Off

UNLESS OTHERWISE SPECIFIED: DIMENSIONS ARE IN MILLIMETERS SURFACE FINISH: **TOLERANCES: +/-1 mm** LINEAR: **ANGULAR: 0.5 deg.**	FINISH:		DEBUR AND BREAK SHARP EDGES	DO NOT SCALE DRAWING	REVISION	
				Anton Tkachev		
	NAME	SIGNATURE	DATE	TITLE:		
DRAWN				Linkage for the actuator		
CHK'D						
APPV'D						
MFG						
Q.A			MATERIAL: Steel	DWG NO.	linkage	A4
			WEIGHT:	SCALE:1:5	SHEET 1 OF 1	

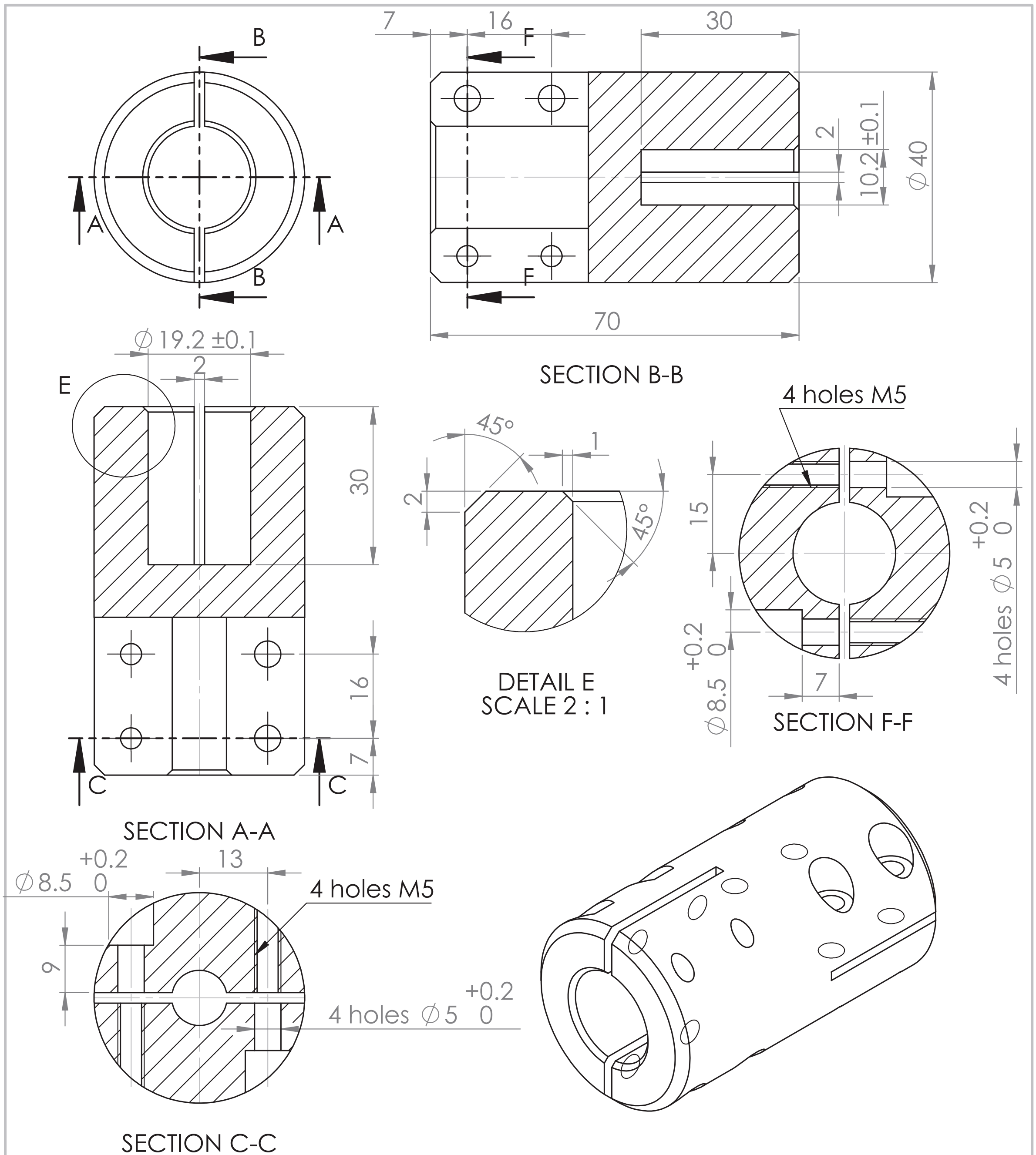

a) dimensions with tolerances to be provided
b) if tolerance not specified assume +/- 0.2 mm

Qty: 1 off

UNLESS OTHERWISE SPECIFIED: DIMENSIONS ARE IN MILLIMETERS SURFACE FINISH: TOLERANCES: LINEAR: ANGULAR:			FINISH:		DEBUR AND BREAK SHARP EDGES	DO NOT SCALE DRAWING	REVISION
						Anton Tkachev 0420362277	
	NAME	SIGNATURE	DATE			TITLE: Motor - ball-screw coupling	
DRAWN							
CHK'D							
APPV'D							
MFG							
Q.A				MATERIAL: Aluminium		DWG NO. motor-coupling	A4
				WEIGHT:		SCALE:1:1	SHEET 1 OF 1

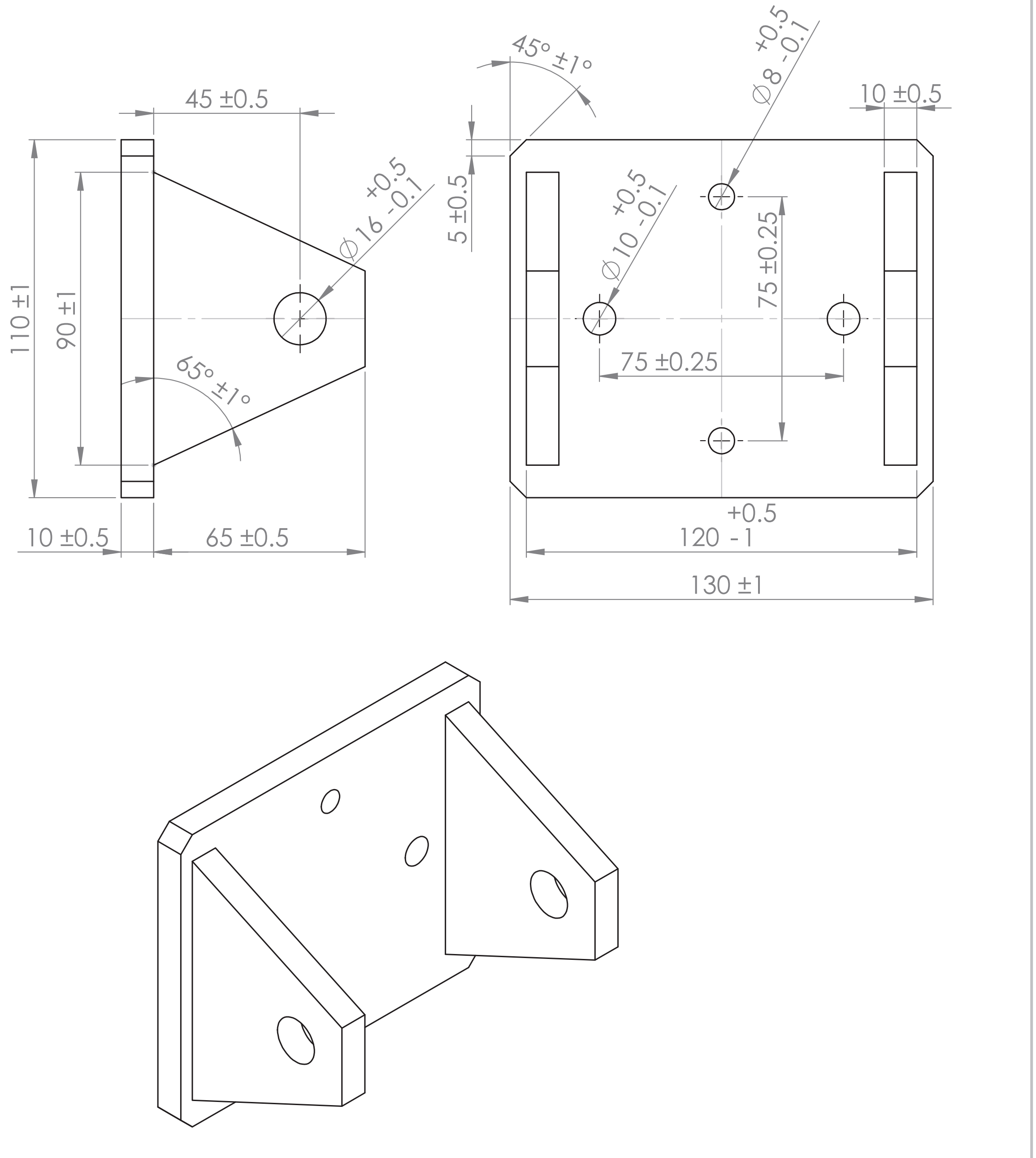

All parts welded

Qty: 1 off

UNLESS OTHERWISE SPECIFIED: DIMENSIONS ARE IN MILLIMETERS SURFACE FINISH: TOLERANCES: LINEAR: ANGULAR:	FINISH:	DEBUR AND BREAK SHARP EDGES	DO NOT SCALE DRAWING	REVISION
			Anton Tkachev 0420362277	

	NAME	SIGNATURE	DATE		
DRAWN					TITLE: Half car rig pivot at cylinder side
CHK'D					
APPV'D					
MFG					
Q.A				MATERIAL: M. Steel	DWG NO. rig-pivot-mnt-cylinder A4
				WEIGHT:	SCALE:1:2 SHEET 1 OF 1

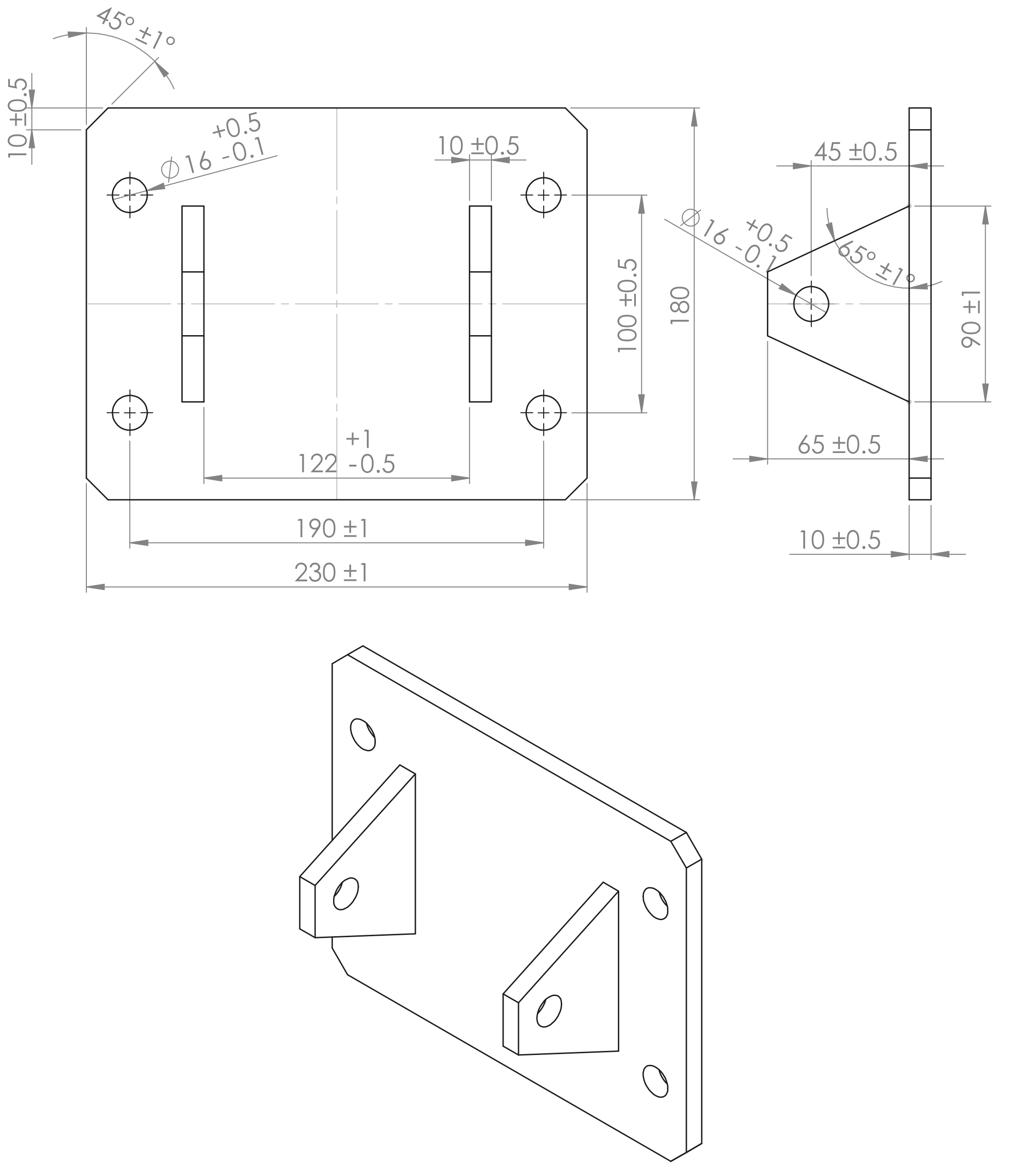

All parts welded

Qty: 1 off

UNLESS OTHERWISE SPECIFIED:
DIMENSIONS ARE IN MILLIMETERS
SURFACE FINISH:
TOLERANCES:
LINEAR:
ANGULAR:

FINISH:

DEBUR AND BREAK SHARP EDGES

DO NOT SCALE DRAWING

REVISION

Anton Tkachev 0420362277

	NAME	SIGNATURE	DATE
DRAWN			
CHK'D			
APPV'D			
MFG			
Q.A			

TITLE:

Half car rig pivot at frame side

MATERIAL:

M. Steel

DWG NO.

rig-pivot-mnt-side-frame

A4

WEIGHT:

SCALE:1:5

SHEET 1 OF 1

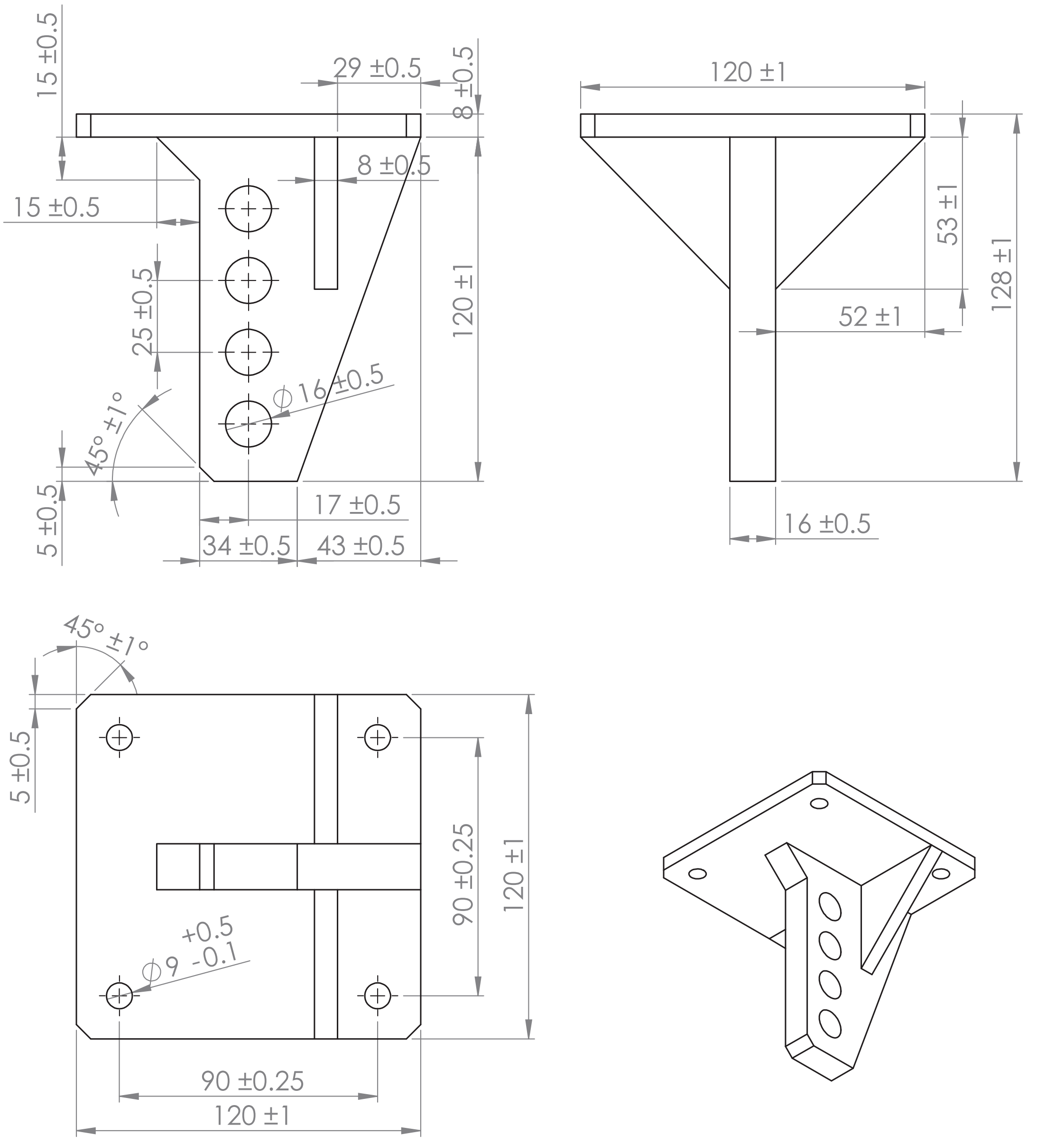

All parts welded

Qty: 1 off

UNLESS OTHERWISE SPECIFIED:
DIMENSIONS ARE IN MILLIMETERS
SURFACE FINISH:
TOLERANCES:
LINEAR:
ANGULAR:

FINISH:

DEBUR AND BREAK SHARP EDGES

DO NOT SCALE DRAWING

REVISION

Anton Tkachev 0420362277

	NAME	SIGNATURE	DATE
DRAWN			
CHK'D			
APPV'D			
MFG			
Q.A			

TITLE:

Half car rig roll pivot

MATERIAL:
M. Steel

DWG NO.
rig-roll-frame-pivot

A4

WEIGHT:

SCALE:1:5

SHEET 1 OF 1

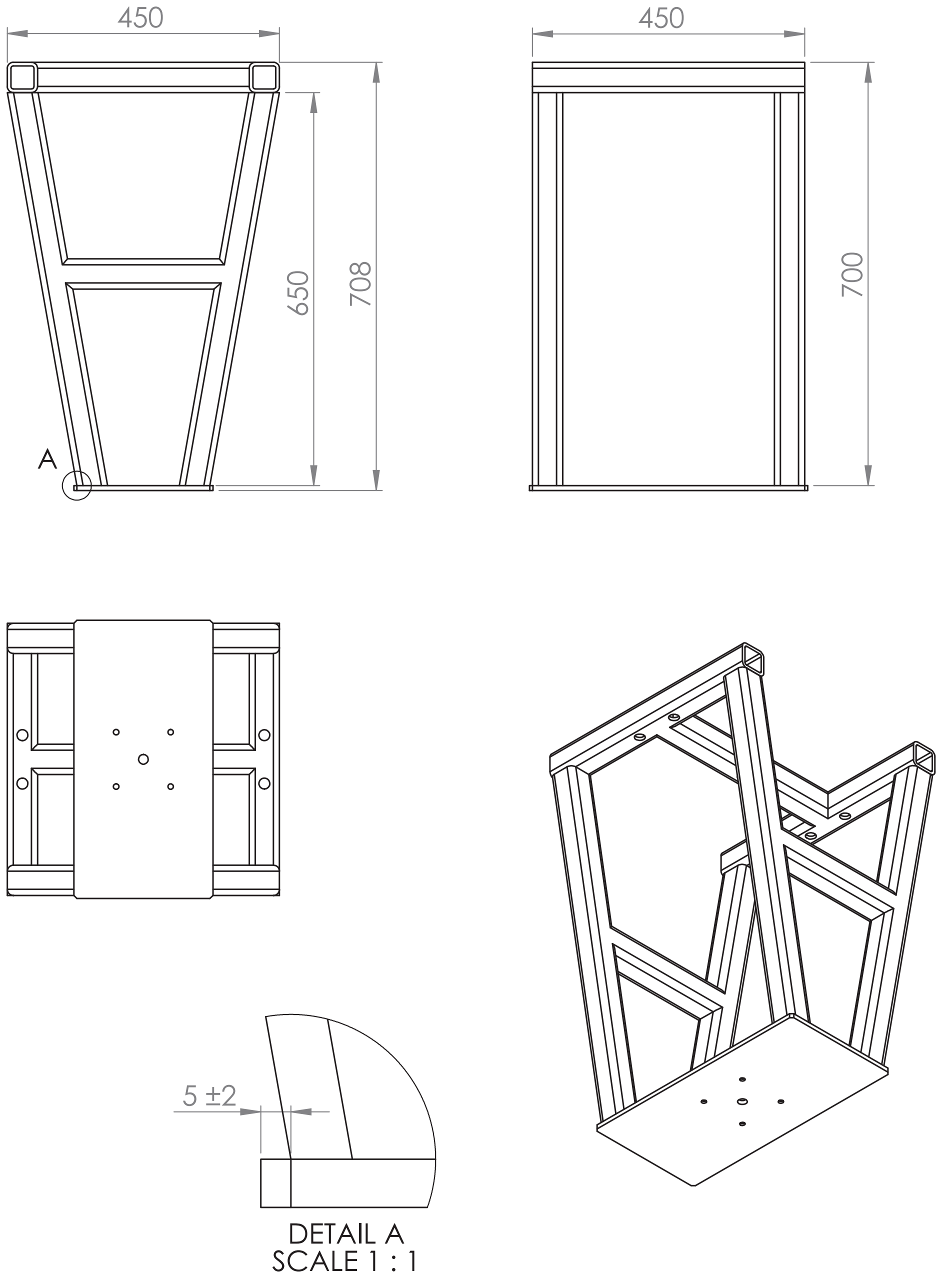

All parts welded

UNLESS OTHERWISE SPECIFIED: DIMENSIONS ARE IN MILLIMETERS SURFACE FINISH: TOLERANCES: LINEAR: ANGULAR:	FINISH:	DEBUR AND BREAK SHARP EDGES	DO NOT SCALE DRAWING	REVISION

Anton Tkachev 0420362277

	NAME	SIGNATURE	DATE
DRAWN			
CHK'D			
APPV'D			
MFG			
Q.A			

TITLE:

Half car rig roll frame assembly

MATERIAL:

M. Steel

DWG NO. rig-roll-frame

A4

WEIGHT:

SCALE:1:10

SHEET 1 OF 1

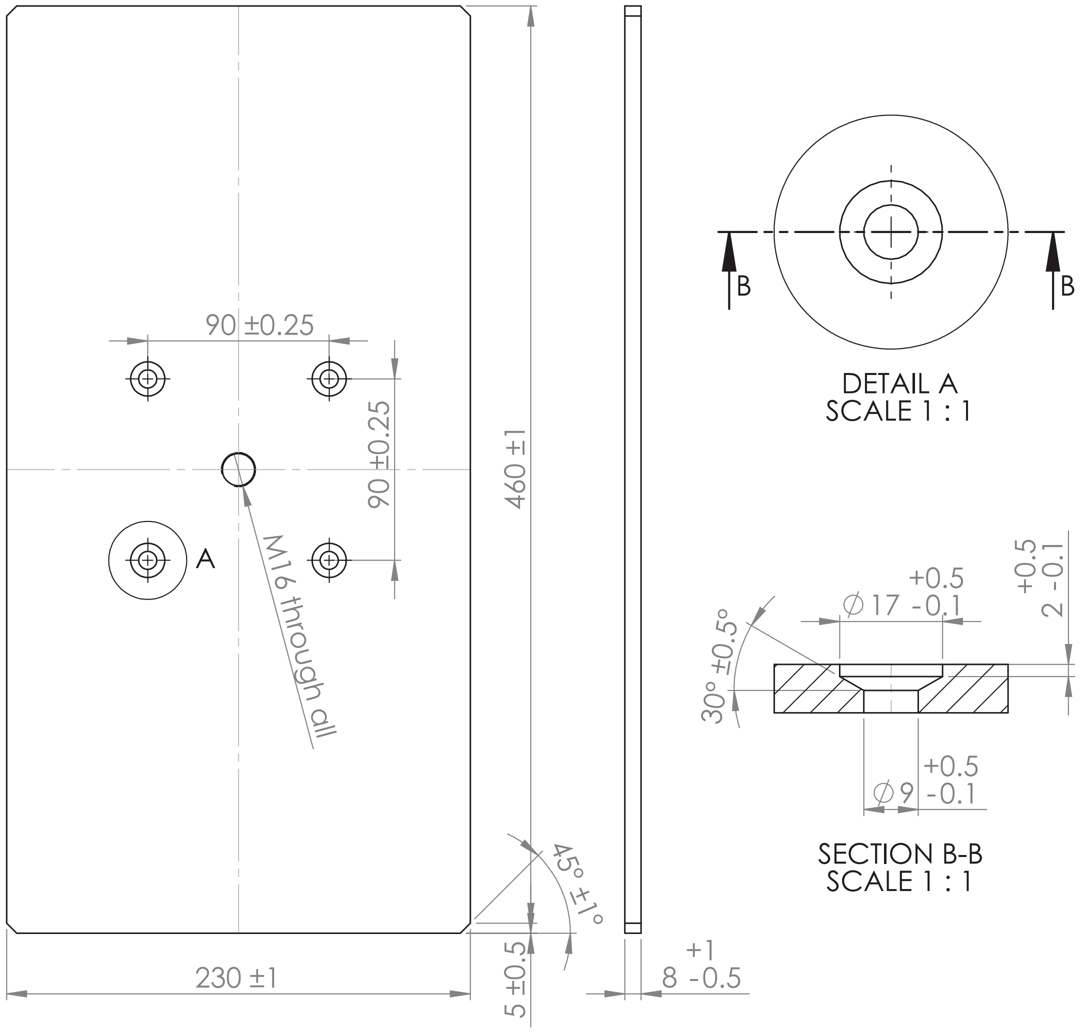

Qty: 1 off

UNLESS OTHERWISE SPECIFIED: DIMENSIONS ARE IN MILLIMETERS SURFACE FINISH: TOLERANCES: LINEAR: ANGULAR:	FINISH:	DEBUR AND BREAK SHARP EDGES	DO NOT SCALE DRAWING	REVISION
			Anton Tkachev 0420362277	

	NAME	SIGNATURE	DATE
DRAWN			
CHK'D			
APPV'D			
MFG			
Q.A			

TITLE:

Half car rig lower plate

MATERIAL:

M. Steel

DWG NO.

rig-roll-frame-bottom-plate

A4

WEIGHT:

SCALE:1:10

SHEET 1 OF 1

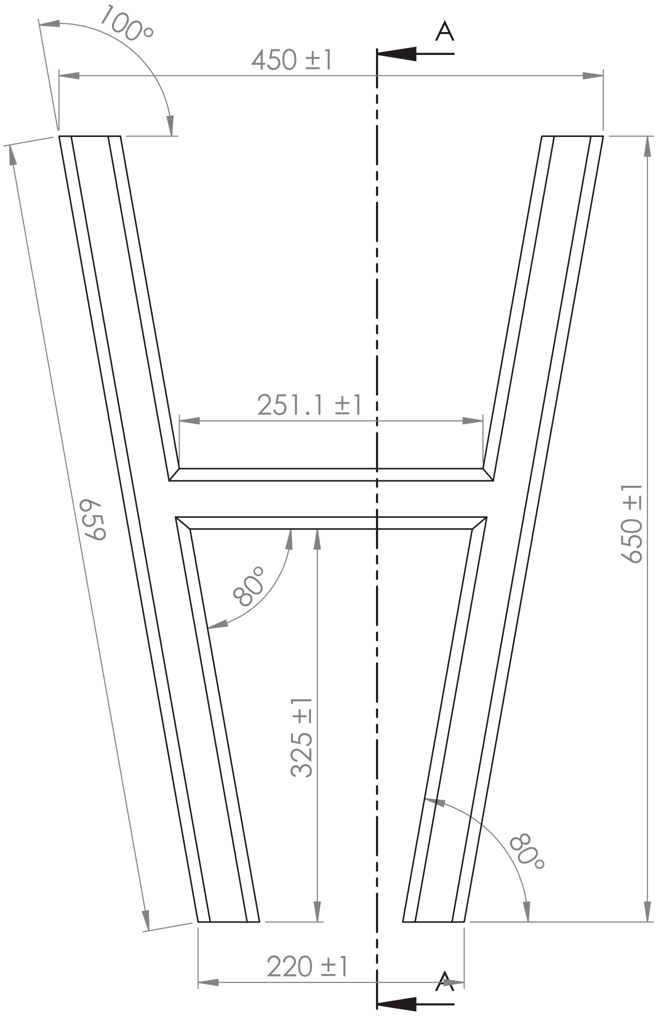

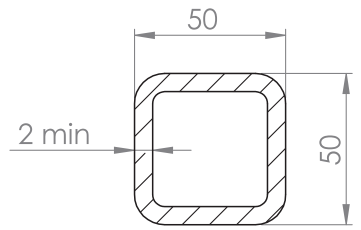

SECTION A-A
SCALE 1 : 2

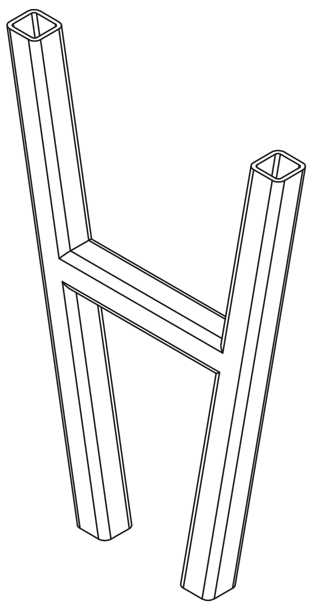

Dimensions with tolerances to be provided
Other dimensions are given for reference

All parts welded

Qty: 2 off

UNLESS OTHERWISE SPECIFIED:
DIMENSIONS ARE IN MILLIMETERS
SURFACE FINISH:
TOLERANCES:
LINEAR:
ANGULAR:

FINISH:

DEBUR AND BREAK SHARP EDGES

DO NOT SCALE DRAWING

REVISION

Anton Tkachev 0420362277

	NAME	SIGNATURE	DATE
DRAWN			
CHK'D			
APPV'D			
MFG			
Q.A			

TITLE:

Half car rig roll frame side part

MATERIAL:
M. Steel

WEIGHT:

DWG NO.
rig-roll-frame-side-part

A4

SCALE:1:5

SHEET 1 OF 1

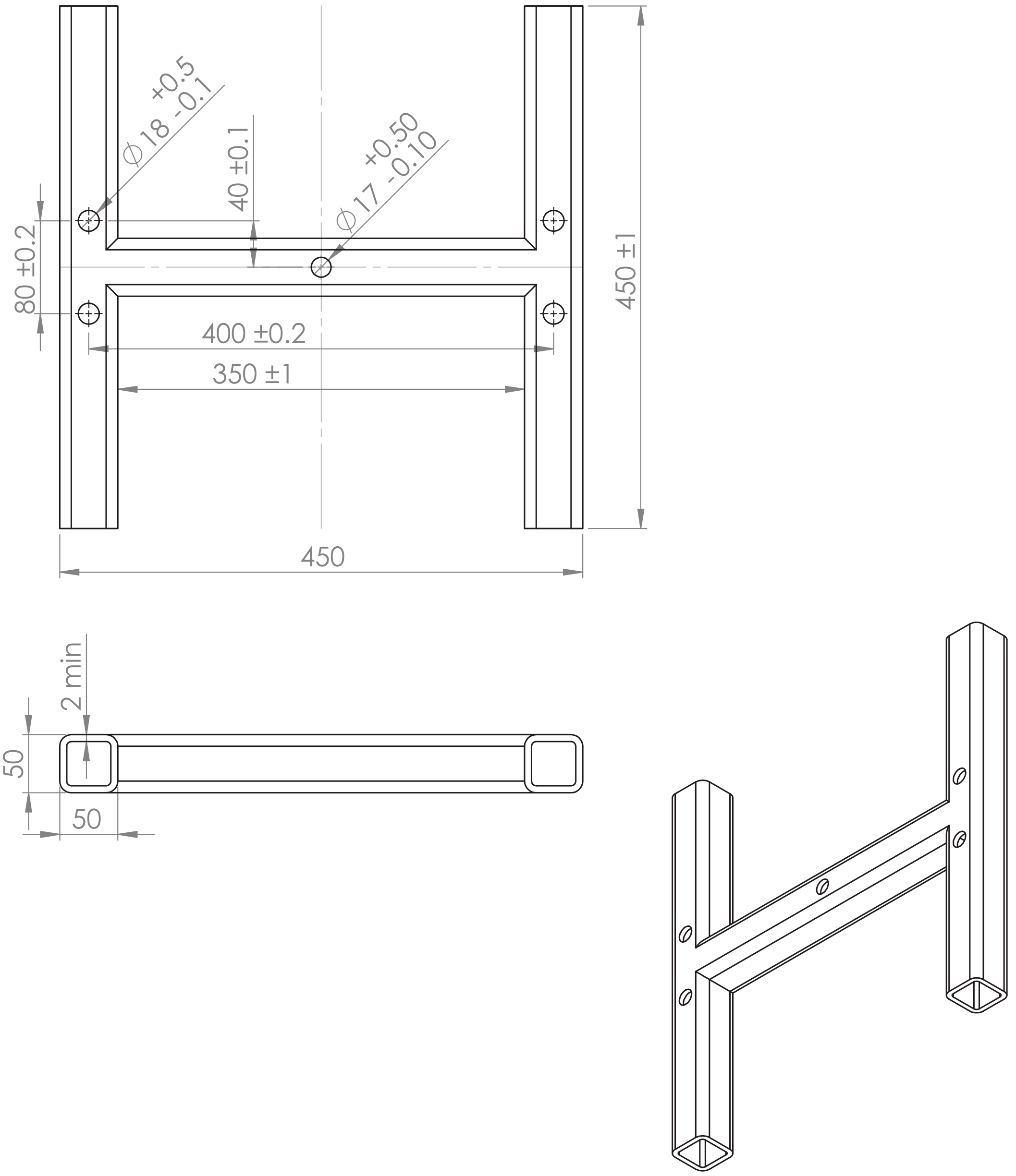

Qty: 1 off

UNLESS OTHERWISE SPECIFIED: DIMENSIONS ARE IN MILLIMETERS SURFACE FINISH: TOLERANCES: LINEAR: ANGULAR:	FINISH:	DEBUR AND BREAK SHARP EDGES	DO NOT SCALE DRAWING	REVISION
			Anton Tkachev 0420362277	

	NAME	SIGNATURE	DATE
DRAWN			
CHK'D			
APPV'D			
MFG			
Q.A			

TITLE:

Half car rig roll frame top part

MATERIAL: M. Steel

WEIGHT:

DWG NO. rig-roll-frame-top-part

A4

SCALE:1:10

SHEET 1 OF 1

Bibliography

[1] Sangzhi Zhu, Lifu Wang, Nong Zhang, and Haiping Du. H-infinity control of a novel low-cost roll-plane active hydraulically interconnected suspension: An experimental investigation of roll control under ground excitation. *SAE International Journal of Passenger Cars-Mechanical Systems*, 6(2013-01-1238):882–893, 2013.

[2] Sangzhi Zhu, Haiping Du, and Nong Zhang. Development and implementation of fuzzy, fuzzy pid and lqr controllers for an roll-plane active hydraulically interconnected suspension. In *Fuzzy Systems (FUZZ-IEEE), 2014 IEEE International Conference on*, pages 2017–2024. IEEE, 2014.

[3] Sangzhi Zhu, Haiping Du, Nong Zhang, and Lifu Wang. Development of a new model for roll-plane active hydraulically interconnected suspension. *SAE International Journal of Passenger Cars-Mechanical Systems*, 7(2014-01-0053):447–457, 2014.

[4] Nong Zhang, Wade A Smith, and Jeku Jeyakumaran. Hydraulically interconnected vehicle suspension: background and modelling. *Vehicle System Dynamics*, 48(1):17–40, 2010.

[5] Wade A Smith, Nong Zhang, and Jeku Jeyakumaran. Hydraulically interconnected vehicle suspension: theoretical and experimental ride analysis. *Vehicle system dynamics*, 48(1):41–64, 2010.

[6] Wade A Smith, Nong Zhang, and William Hu. Hydraulically interconnected vehicle suspension: handling performance. *Vehicle system dynamics*, 49(1-2):87–106, 2011.

[7] James R Wilde, Gary J Heydinger, Dennis A Guenther, Tom Mallin, and Andrew M Devenish. Experimental evaluation of fishhook maneuver performance of a kinetic suspension system. Technical report, SAE Technical Paper, 2005.

[8] James R Wilde, Gary J Heydinger, and Dennis A Guenther. Adams simulation of ride and handling performance of the kinetic tm suspension system. *SAE Transactions*, pages 1646–1659, 2006.

[9] Dongpu Cao, Subhash Rakheja, and Chun-Yi Su. Comparison of roll properties of hydraulically and pneumatically interconnected suspensions for heavy vehicles. Technical report, SAE Technical Paper, 2005.

[10] Wei Gao, N Zhang, and HP Du. A half-car model for dynamic analysis of vehicles with random parameters. In *5th Australasian Congress on Applied Mechanics (ACAM 2007)*, volume 1, pages 595–600. Engineers Australia, 2007.

[11] Nong Zhang, Wade Smith, Jeku Jeyakumaran, and William Hu. Determination of modal parameters of a half-car fitted with a hydraulically interconnected suspension from simulated free decay responses. In *5th Australasian Congress on Applied Mechanics (ACAM 2007)*, volume 1, pages 601–607. Engineers Australia, 2007.

[12] Wade Alister Smith. *An investigation into the dynamics of vehicles with hydraulically interconnected suspensions*. PhD thesis, University of Technology Sydney, Green Energy and Vehicle Innovations Centre, Electrical Mechanical and Mechatronics School, 2009, http://hdl.handle.net/10453/36058.

[13] Lifu Wang, Nong Zhang, and Haiping Du. Design and experimental investigation of demand dependent active suspension for vehicle rollover control. In *Decision and Control, 2009 held jointly with the 2009 28th Chinese Control Conference.*

CDC/CCC 2009. Proceedings of the 48th IEEE Conference on, pages 5158–5163. IEEE, 2009.

[14] Lifu Wang, Nong Zhang, Haiping Du, et al. Modelling, parameter estimation and testing of a vehicle with anti-roll systems. In *Proceedings of the 6th Australasian Congress on Applied Mechanics*, page 119. Engineers Australia, 2010.

[15] Lifu Wang, Nong Zhang, and Haiping Du. Experimental investigation of a hydraulically interconnected suspension in vehicle dynamics and stability control. *SAE International Journal of Passenger Cars-Mechanical Systems*, 5(2012-01-0240):759–768, 2012.

[16] Fei Ding, Nong Zhang, and Xu Han. Modeling and modal analysis of multi-body truck system fitted with hydraulically interconnected suspension. *Jixie Gongcheng Xuebao/Journal of Mechanical Engineering*, 2012.

[17] Fei Ding, Xu Han, Zhen Luo, and Nong Zhang. Modelling and characteristic analysis of tri-axle trucks with hydraulically interconnected suspensions. *Vehicle System Dynamics*, 50(12):1877–1904, 2012.

[18] Lifu Wang, Nong Zhang, Haiping Du, et al. Modelling and parameter estimation of an active hydraulic suspension using experimental method. In *Proceedings: the 7th Australasian Congress on Applied Mechanics (ACAM 7), 9-12 December 2012, the University of Adelaide, North Terrace Campus/National Committee on Applied Mechanics of Engineers Australia*, page 727. Engineers Australia, 2012.

[19] Lifu Wang, Guangzhong Xu, Nong Zhang, and Holger Roser. Experimental comparison of anti-roll bar with hydraulically interconnected suspension in articulation mode. Technical report, SAE Technical Paper, 2013.

[20] William S Levine. *The control handbook*. CRC press, 1996.

[21] David G Alciatore. *Introduction to mechatronics and measurement systems*. Tata McGraw-Hill Education, 2007.

[22] Chengyuan Ren and Kai Li. Analysis on hydraulic parameters of interconnected suspension based on fuzzy grey correlation. *International Journal of Vehicle Noise and Vibration*, 13(1):1–12, 2017.

[23] ARASH HOSSEINIAN AHANGARNEJAD. Integrated control of active vehicle chassis control systems. 2018.

[24] Lifu Wang, Song Jian, Hengmin Qi, and Nong Zhang. Lateral stability study of a vehicle fitted with hydraulically interconnected suspension in slalom maneuver. In *Chinese Automation Congress (CAC), 2017*, pages 1702–1707. IEEE, 2017.

[25] Shengzhao Chen, Bangji Zhang, Boyuan Li, and Nong Zhang. Dynamic characteristics analysis of vehicle incorporating hydraulically interconnected suspension system with dual accumulators. *Shock and Vibration*, 2018, 2018.

[26] Reza N Jazar. Vehicle dynamics. *Theory and Applications. Riverdale, NY: Springer Science+ Business Media*, 2008.

[27] LD Landau and EM Lifshitz. Mechanics, vol. 1. *Course of theoretical physics*, 3, 1976.

[28] Nook industries - ball screw torque calculations. `http://www.nookindustries.com/LinearLibraryItem/Ballscrew_Torque_Calculations`, 03 2015. (21/1/2018).

[29] Arthur Akers, Max Gassman, and Richard Smith. *Hydraulic power system analysis*. CRC press, 2006.

[30] A Esposito. A simplified method for analyzing hydraulic circuits by analogy. *Machine Design*, 41(24):173, 1969.

[31] Brian J Kirby. *Micro-and nanoscale fluid mechanics: transport in microfluidic devices*. Cambridge University Press, 2010.

[32] DV Sivukhin. A course of general physics. vol. ii, thermodynamics and molecular physics, 1996.

[33] Mark Waldo Zemansky and Richard H Dittman. *Heat and thermodynamics: an intermediate textbook*. McGraw-Hill New York, 1968.

[34] Kalil T Swain Oldham. *The doctrine of description: Gustav Kirchhoff, classical physics, and the "purpose of all science" in 19 th-century Germany*. University of California, Berkeley, 2008.

[35] Steve Smale. The fundamental theorem of algebra and complexity theory. *Bulletin of the American Mathematical Society*, 4(1):1–36, 1981.

[36] Wodek Gawronski and Jer-Nan Juang. Model reduction in limited time and frequency intervals. *International Journal of Systems Science*, 21(2):349–376, 1990.

[37] An-Pan Cherng. Formulation of hankel singular values and singular vectors in time domain. In *PROCEEDINGS-SPIE THE INTERNATIONAL SOCIETY FOR OPTICAL ENGINEERING*, volume 1, pages 436–442. SPIE INTERNATIONAL SOCIETY FOR OPTICAL, 1998.

[38] Control tutorials for matlab and simulink introduction statespace methods for controller design. `http://ctms.engin.umich.edu/CTMS/index.php?example=Introduction&section=ControlStateSpace`, 08 2014. (13/1/2018).

[39] Stanley M Shinners. *Modern control system theory and design*. John Wiley & Sons, 1998.

[40] The University of Texas at Arlington. Control system lectures, lecture 22. `http://www.uta.edu/utari/acs/ee4314/lectures/Lecture%2022.pdf`, 05 2017. (24/8/2018).

[41] Control systemsstate feedback wikibooks open books for an open world. `https://en.wikibooks.org/wiki/Control_Systems/State_Feedback#Ackerman.27s_formula`, 10 2007. (24/8/2018).

[42] Kalman filter - mathworks. `https://au.mathworks.com/help/control/ref/kalmanfilter.html`, 06 2016. (22/1/2018).

[43] Ronald Newbold Bracewell and Ronald N Bracewell. *The Fourier transform and its applications*, volume 31999. McGraw-Hill New York, 1986.

[44] Fredric J Harris. On the use of windows for harmonic analysis with the discrete fourier transform. *Proceedings of the IEEE*, 66(1):51–83, 1978.

[45] F.P. Miller, A.F. Vandome, and J. McBrewster. *Nyquist-Shannon Sampling Theorem: Aliasing, Sine Wave, Signal Processing, Nyquist Rate, Nyquist Frequency, Sampling Rate, Shannon-Hartley Theorem, Whittaker-Shannon Interpolation Formula, Reconstruction from Zero Crossings*. Alphascript Publishing, 2010.

[46] Lennart Ljung. System identification. In *Signal analysis and prediction*, pages 163–173. Springer, 1998.

[47] Digital filter wikipedia. `https://en.wikipedia.org/wiki/Digital_filter`, 01 2004. (1/1/2018).